Constraining the top quark Yukawa coupling using the «Higgs without Higgs» approach at the CMS detector

Master Thesis

Fabian Stäger

supervised by
Prof. Dr. Florencia Canelli
Dr. Adinda de Wit

Abstract

A precise measurement of the top quark Yukawa coupling is an important test of electroweak symmetry breaking in the Standard Model. A deviation of the top quark Yukawa coupling from its Standard Model prediction induces a quadratic energy growth in the amplitude $\mathcal{M}(bV_l \to tV_lV_l)$ involving a top quark, a bottom quark, and three longitudinally polarized vector bosons. At hadron colliders, this amplitude contributes to the production of the $pp \to tjVV'$ process with a final state consisting of a top quark, a forward jet, and two W or Z bosons. In this thesis, I test the possibility of constraining the top quark Yukawa coupling with data to be collected by the CMS detector at the High Luminosity Large Hadron Collider, using the $tjVV'$ process. The analysis is conducted using simulated proton-proton collisions at a center of mass energy $\sqrt{s} = 13$ TeV and takes into account only the $pp \to tjW^+W^-$ production mode in which the W bosons decay semileptonically. Assuming the statistical uncertainties on the Monte Carlo samples to be negligible, the $\pm 1\sigma$ uncertainty of this measurement on the ratio of the top quark Yukawa coupling to the Standard Model prediction, y_t/y_t^{SM}, is expected to be 32% with a 2σ upper limit of $y_t/y_t^{\mathrm{SM}} < 1.55$.

Contents

1 Introduction

One of the main goals of the Large Hadron Collider (LHC) physics programme is the precise measurement of the properties of the Higgs boson, the particle responsible for spontaneous symmetry breaking in the electroweak sector of the Standard Model (SM). In the SM, the strength of the interaction of a fermion ψ with the Higgs boson, the Yukawa coupling y_ψ, is proportional to the fermion mass m_ψ. The top quark is the heaviest fermion by a large margin, its Yukawa coupling is close to unity and two to six orders of magnitude bigger than those of the other fermions. Being the heaviest particle in the SM, the top quark is possibly the particle closest to new physics beyond the Standard Model (BSM). The precise measurement of the top quark Yukawa coupling is an important test of the SM electroweak symmetry breaking and offers a window into BSM physics.

Deviations from the SM predictions can be expressed in a model-independent way in terms of an effective field theory (EFT). The EFT operators that modify the couplings of the Higgs boson induce energy growing effects in amplitudes involving longitudinally polarized vector bosons. In the case of the top quark Yukawa coupling, this effect grows with energy squared. Recently, it has been proposed in reference [1] to measure modifications of the Higgs boson couplings off-shell and at high energies, via their contributions to the physics of longitudinal vector bosons. This approach, dubbed *Higgs without Higgs* (HwH) by the authors, is complementary to and potentially competitive with on-shell measurements and profits maximally from accumulated statistics of the High Luminosity LHC (HL-LHC) programme and from future high energy colliders.

In this thesis, I investigate a potential measurement of modifications to the top quark Yukawa coupling in the $pp \to tjVV$ process and make predictions on the sensitivity of such a measurement to be performed by the CMS experiment at the HL-LHC, using simulations of proton-proton collisions inside the CMS detector.

The outline of this thesis is as follows. Chapters 2 and 3 give an overview of the theoretical background; the Standard Model, the EFT approach to BSM physics, and the EFT operator that modifies the top quark Yukawa coupling. Chapter 4 describes the CMS detector. The signal channel and the relevant background processes are described in chapter 5. The event selection and the systematic uncertainties are described in chapters 6 and 7. Chapter 8 covers the statistical methods and makes a prediction on the sensitivity of the analysis. In chapter 9, the results are summarized and compared to those of other analyses, and several options for improvement are discussed.

2 The Standard Model

The SM is a quantum field theory that describes the elementary particles and their interactions. The three fundamental interactions (strong, weak, electromagnetic) of the spin-$\frac{1}{2}$ fermions

$$L^i = \begin{pmatrix} \nu^i \\ \ell^i \end{pmatrix} = \begin{pmatrix} \nu_e \\ e \end{pmatrix}, \begin{pmatrix} \nu_\mu \\ \mu \end{pmatrix}, \begin{pmatrix} \nu_\tau \\ \tau \end{pmatrix}; \qquad Q^i = \begin{pmatrix} u^i \\ d^i \end{pmatrix} = \begin{pmatrix} u \\ d \end{pmatrix}, \begin{pmatrix} c \\ s \end{pmatrix}, \begin{pmatrix} t \\ b \end{pmatrix}, \tag{2.1}$$

are mediated by the spin-1 bosons

$$A_\mu, \ W_\mu^\pm, \ Z_\mu, \ G_\mu^a \quad (a = 1, ..., 8). \tag{2.2}$$

These interactions are a consequence of the local symmetry $\mathrm{SU(3)_c \times SU(2)_L \times U(1)_Y}$ and are described in sections 2.1, 2.2, 2.3. The masses of fermions and vector bosons are generated by their interactions with the spin-0 complex scalar field

$$H = \begin{pmatrix} H^+ \\ H^0 \end{pmatrix}. \tag{2.3}$$

The spontaneous symmetry breaking $\mathrm{SU(2)_L \times U(1)_Y \longrightarrow U(1)_Q}$ by the vacuum expectation value of H, described in section 2.4, generates the masses of the $W_\mu^\pm$ and Z_μ gauge bosons of the weak interaction while leaving the photon A_μ of the electromagnetic interaction massless. The Yukawa interactions, described in section 2.5, generate fermion masses and explicitly break the global flavour symmetry. The discussion of the SM in this chapter is based on F. Halzen, A. Martin, *Quarks & Leptons* [2], chapters 12-15; M. Schwartz, *Quantum Field Theory and the Standard Model* [3], chapters 21-22, 25, 28-29; and G. Isidori, *Flavour physics and CP violation* [4], chapters 1-2.

Table 2.1: The particles of the Standard Model and their electric charge Q [5].

Quarks	**u**	**c**	**t**	Leptons	$\boldsymbol{\nu_e}$	$\boldsymbol{\nu_\mu}$	$\boldsymbol{\nu_\tau}$
	up	charm	top		electron neutrino	muon neutrino	tau neutrino
	$Q = 2/3$	$Q = 2/3$	$Q = 2/3$		$Q = 0$	$Q = 0$	$Q = 0$
	d	**s**	**b**		**e**	$\boldsymbol{\mu}$	$\boldsymbol{\tau}$
	down	strange	bottom		electron	muon	tau
	$Q = -1/3$	$Q = -1/3$	$Q = -1/3$		$Q = -1$	$Q = -1$	$Q = -1$

spin-0 bosons	**H**	spin-1 bosons	**A**	**W$^\pm$**	**Z**	**G^a**
	Higgs boson $Q = 0$		photon $Q = 0$	W boson $Q = \pm 1$	Z boson $Q = 0$	gluon $Q = 0$

2.1 Quantum Electrodynamics: U(1) gauge theory

A fermion $\psi(x)$ with mass m is described by the free Dirac Lagrangian [2]

$$\mathcal{L}_0 = \overline{\psi}\left(i\gamma^\mu\partial_\mu - m\right)\psi\,, \tag{2.4}$$

which is invariant with respect to a global U(1) phase transformation

$$\psi(x) \longrightarrow e^{i\theta}\psi(x)\,. \tag{2.5}$$

The global U(1) symmetry has a Noether current [2]

$$j^\mu(x) = \frac{\delta\mathcal{L}}{\delta\partial_\mu\psi}\frac{\delta\psi}{\delta\theta} = \overline{\psi}\gamma^\mu\psi\,, \quad \partial^\mu j_\mu = 0\,. \tag{2.6}$$
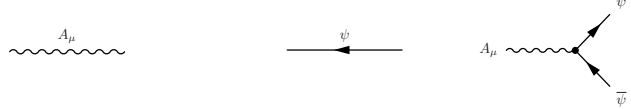
The corresponding conserved Noether charge is the electric charge. The gauge principle requires the Lagrangian to be invariant under a *local* U(1) transformation (space-time dependent phase $\theta = \theta(x)$) [2]. This is achieved by constructing a covariant derivative $D_\mu = \partial_\mu - ieA_\mu$. If the vector field $A_\mu(x)$ transforms as

$$A_\mu(x) \longrightarrow A_\mu(x) + \frac{1}{e}\partial_\mu\theta(x) \quad\Longrightarrow\quad D_\mu\psi(x) \longrightarrow e^{i\theta(x)}D_\mu\psi(x)\,, \tag{2.7}$$

then the Lagrangian

$$\mathcal{L} = \overline{\psi}\left(i\gamma^\mu D_\mu - m\right)\psi = \overline{\psi}\left(i\gamma^\mu\partial_\mu - m\right)\psi + e\,\overline{\psi}\gamma^\mu\psi A_\mu \tag{2.8}$$

is gauge invariant. The vector field A_μ, called the photon, couples to the electromagnetic current j^μ of equation (2.6). A gauge invariant kinetic term for the photon A_μ is built using the field strength tensor $F_{\mu\nu} = \partial_\mu A_\nu - \partial_\nu A_\mu$. The full Lagrangian of Quantum Electrodynamics (QED) is [2]

$$\begin{aligned}
\mathcal{L}_{\text{QED}} &= -\frac{1}{4}F_{\mu\nu}F^{\mu\nu} + \overline{\psi}\left(i\gamma^\mu D_\mu - m\right)\psi \\
&= -\underbrace{\frac{1}{2}\partial_\mu A_\nu\left(\partial^\mu A^\nu - \partial^\nu A^\mu\right)}_{A_\mu} + \underbrace{\overline{\psi}\left(i\gamma^\mu\partial_\mu - m\right)\psi}_{\psi} + \underbrace{e\,\overline{\psi}\gamma^\mu\psi A_\mu}_{A_\mu}\;.
\end{aligned} \tag{2.9}$$

2.2 Quantum Chromodynamics: SU(3) gauge theory

Quantum Chromodynamics (QCD) is the theory of the strong interactions of quarks and gluons. Quarks come in three copies or colours (r, g, b). They are SU(3) triplets [2]

$$\psi(x) = \begin{pmatrix}\psi_1(x)\\\psi_2(x)\\\psi_3(x)\end{pmatrix} \tag{2.10}$$

in the fundamental representation. The U(1) gauge symmetry of section 2.1 is generalized to the case of the non-Abelian gauge group SU(3), starting from the free Lagrangian for a fermion triplet $\psi_i(x)$

$$\mathcal{L}_0 = \overline{\psi}_i \left(i\gamma^\mu \partial_\mu \delta_{ij} - m\delta_{ij} \right) \psi_j = \overline{\psi} \left(i\gamma^\mu \partial_\mu - m \right) \psi \,, \tag{2.11}$$

invariant with respect to the eight global SU(3) transformations with eight conserved Noether currents [3]

$$\psi_i(x) \longrightarrow e^{i\theta^a T_{ij}^a} \psi_j(x) \,, \quad j_a^\mu = \overline{\psi}_i \gamma^\mu T_{ij}^a \psi_j \,. \tag{2.12}$$

The complex 3×3 matrices T_{ij}^a are the generators of the fundamental representation of SU(3). Invariance with respect to local SU(3) transformations is achieved by introducing the covariant derivative

$$(D_\mu)_{ij} = \partial_\mu \delta_{ij} - ig_s G_\mu^a T_{ij}^a \tag{2.13}$$

with the strong coupling constant g_s and eight gauge boson fields G_μ^a, called gluons, that transform as

$$G_\mu^a(x) \longrightarrow G_\mu^a(x) + \frac{1}{g_s} \partial_\mu \theta^a(x) - f^{abc}\theta^b(x)G_\mu^c(x) \,, \tag{2.14}$$

with structure constants $f^{abc} \in \mathbb{R}$ and indices a, b, c going from 1 to 8 [3]. The last term, $f^{abc}\theta^b G_\mu^c$, contributes to global transformations with $\partial_\mu \theta^a = 0$. The gluons G_μ^a therefore carry SU(3) charge. This is a consequence of the non-Abelian character of the gauge group SU(3), the fact that the generators T^a do not commute ($\left[T^a, T^b \right] = i f^{abc}T^c \neq 0$). Therefore, the field strength tensor

$$G_{\mu\nu}^a = \partial_\mu G_\nu^a - \partial_\nu G_\mu^a + g_s f^{abc} G_\mu^b G_\nu^c \tag{2.15}$$

has a new term quadratic in G_μ^a, leading to gluon self-interactions. The full Lagrangian of QCD is [3]

$$\begin{aligned}
\mathcal{L}_{\mathrm{QCD}} = &- \frac{1}{4} G_{\mu\nu}^a G^{a\,\mu\nu} + \overline{\psi} \left(i\gamma^\mu D_\mu - m \right) \psi \\
= &- \underbrace{\frac{1}{2} \partial_\mu G_\nu^a \left(\partial^\mu G^{a\,\nu} - \partial^\nu G^{a\,\mu} \right)}_{} - \underbrace{g_s f^{abc} \left(\partial^\mu G^{a\,\nu} \right) G_\mu^b G_\nu^c}_{} \\
&- \underbrace{\frac{1}{4} g_s^2 f^{abc} f^{ade} G_\mu^b G_\nu^c G^{d\,\mu} G^{e\,\nu}}_{} + \underbrace{\overline{\psi} \left(i\gamma^\mu \partial_\mu - m \right) \psi}_{} + \underbrace{g_s \overline{\psi}_i \gamma^\mu T_{ij}^a \psi_j G_\mu^a}_{} \,.
\end{aligned} \tag{2.16}$$

In the general case of a multiplet of n fermions in the fundamental representation of SU(n), there are $n^2 - 1$ generators and $n^2 - 1$ gauge bosons carrying SU(n) charge. The Lagrangian of an SU(n) gauge theory is called the Yang-Mills Lagrangian [3].

2.3 Electroweak theory

2.3.1 Fermi theory

The Fermi theory describes neutron β-decay in terms of a local 4-fermion interaction (figure 2.1), built on the analogy of a photon coupling to a fermion current j^μ in QED, leading to a $\psi\psi \to \psi\psi$ amplitude

$$\mathcal{M} = \;\rangle\!\!\sim\!\!\langle\; \sim \frac{e^2}{q^2}\, j^\mu j_\mu \,. \tag{2.17}$$

In Fermi theory, the fermion currents couple without exchange of a gauge boson [2]:

$$\mathcal{L}_{\text{Fermi}} = \frac{G_{\text{F}}}{\sqrt{2}}\left(l^{\mu+}h_\mu^- + h^{\mu+}l_\mu^-\right) \quad\longrightarrow\quad \mathcal{M} = \;\rangle\!\!\!\langle\; \sim \frac{G_{\text{F}}}{\sqrt{2}}\, l^{\mu+}h_\mu^- \,. \tag{2.18}$$

Here, the fermion currents $l_\mu^\pm$ and $h_\mu^\pm$ are charged currents coupling left-chiral fermions of different charge:

$$
\begin{aligned}
l_\mu^+ &= \overline{e}\,\gamma_\mu(1-\gamma^5)\,\nu = 2\,\overline{e}_L\gamma_\mu\nu_{\text{L}}\,, & l_\mu^- &= 2\,\overline{\nu}_L\gamma_\mu e_L\,,\\
h_\mu^+ &= \overline{d}\,\gamma_\mu(1-\gamma^5)\,u = 2\,\overline{d}_L\gamma^\mu u_L\,, & h_\mu^- &= 2\,\overline{u}_L\gamma^\mu d_L\,.
\end{aligned}
\tag{2.19}
$$

The Fermi constant is measured to be $G_{\text{F}} \approx 1.17 \times 10^{-5}\,\text{GeV}^{-2} \approx (300\,\text{GeV})^{-2}$ [5]. In the high energy limit ($s \to \infty$), unitarity requires that the differential cross section behaves as

$$\frac{d\sigma}{d\Omega} \sim \frac{1}{s}\overline{\sum}|\mathcal{M}|^2 \overset{!}{\sim} \frac{1}{s}\,. \tag{2.20}$$

Dimensional analysis indicates that the amplitude (2.18) grows with energy squared ($\mathcal{M} \sim G_{\text{F}}s$). Therefore, unitarity is violated if the center of mass energy $\sqrt{s}$ is greater than $1/\sqrt{G_{\text{F}}} \sim 300\,\text{GeV}$. In addition, the mass dimension 6 operators of the local 4-fermion interactions generate quadratic divergences at every order of the perturbative expansion in G_{F}, which can not be reabsorbed into the parameters of the original Lagrangian [3]. This is the case for any operator of mass dimension $d > 4$. Theories containing such operators are called non-renormalizable. However, at low energy ($s \ll G_{\text{F}}^{-1}$), the expansion in G_{F}

$$\rangle\!\!\!\langle \;+\; \rangle\!\!\bigcirc\!\!\langle \;+\;\ldots = \mathcal{M}_0\left(1 + \lambda_1\mathcal{O}(G_{\text{F}}s) + \ldots\right) \tag{2.21}$$

converges quickly and yields precise predictions [3]. In general, non-renormalizable theories can be regarded as low energy approximations of renormalizable high energy theories. Such low energy approximations are called Effective Field Theories (EFT) [4]. They are discussed in more detail in chapter 3.
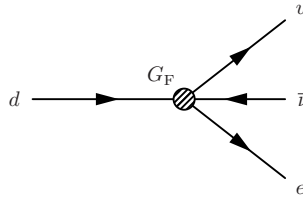

Figure 2.1: The Fermi theory describes neutron β-decay in terms of a local 4-fermion interaction with effective coupling G_{F}.

2.3.2 Intermediate vector bosons

The problems of 4-fermion charged interactions at high energy are solved by introducing two massive charged gauge boson mediators $W_\mu^\pm$ (figure 2.2). The $W_\mu^\pm$ bosons couple to the charged currents $j_\mu^\mp = l_\mu^\mp + h_\mu^\mp$ of equation (2.19) [2]

$$\mathcal{L}_W^{\text{int.}} = \frac{g_2}{2\sqrt{2}} \left(W_\mu^+ j^{\mu-} + W_\mu^- j^{\mu+} \right) ,\tag{2.22}$$

leading to an amplitude

$$\mathcal{M} = \text{\reflectbox{\ding{}}}\!\!\sim\!\!\prec \ \sim \frac{g_2^2}{8} \, j_\mu^+ \left(\frac{-g^{\mu\nu} + q^\mu q^\nu/m_W^2}{q^2 - m_W^2} \right) j_\nu^- .\tag{2.23}$$

Expanding the $W_\mu^\pm$ propagator in inverse powers of the mass m_W [4]

$$D_W^{\mu\nu}(q) = \frac{-g^{\mu\nu} + q^\mu q^\nu/m_W^2}{q^2 - m_W^2} = \frac{g^{\mu\nu}}{m_W^2} + \mathcal{O}\left(\frac{1}{m_W^4} \right),\tag{2.24}$$

it becomes clear that at low energy ($q^2 \ll m_W^2$) the effective 4-fermion interaction of Fermi Theory is recovered:

$$\mathcal{M} \sim \frac{g_2^2}{8} \, j_\mu^+ \left(\frac{-g^{\mu\nu} + q^\mu q^\nu/m_W^2}{q^2 - m_W^2} \right) j_\nu^- \xrightarrow{q^2 \ll m_W^2} \frac{g_2^2}{8m_W^2} \, j^{\mu+} j_\mu^- =: \frac{G_{\text{F}}}{\sqrt{2}} j^{\mu+} j_\mu^- .\tag{2.25}$$

2.3.3 SU(2) × U(1) Electroweak theory

The charged currents

$$\begin{aligned} j_\mu^+ &= 2 \, \overline{e}_L \gamma_\mu \nu_L + 2 \, \overline{d}_L \gamma_\mu u_L , \\ j_\mu^- &= 2 \, \overline{\nu}_L \gamma_\mu e_L + 2 \, \overline{u}_L \gamma_\mu d_L \end{aligned}\tag{2.26}$$

can be constructed in an SU(2) gauge theory. With left-chiral fermion fields $\psi_L = L_L, Q_L$

$$L_L = \begin{pmatrix} \nu_L \\ e_L \end{pmatrix}, \ Q_L = \begin{pmatrix} u_L \\ d_L \end{pmatrix}\tag{2.27}$$

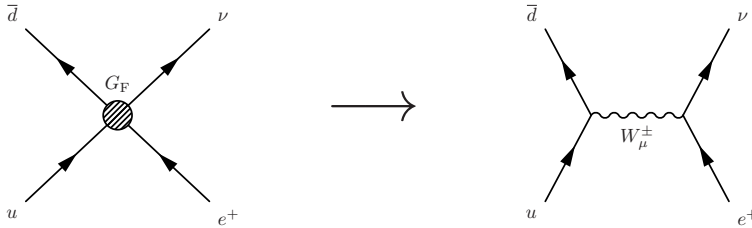Figure 2.2: The weak charged currents are mediated by massive gauge bosons $W_\mu^\pm$. The effective coupling G_{F} is weak not because g_2 is small, but because m_W^2 is large [2].

as doublets in the fundamental representation of SU(2), and generators

$$T^+ = T^1 + iT^2 = \begin{pmatrix} 0 & 1 \\ 0 & 0 \end{pmatrix}, \quad T^- = T^1 - iT^2 = \begin{pmatrix} 0 & 0 \\ 1 & 0 \end{pmatrix}, \quad \left(T^a = \frac{1}{2}\sigma^a \right), \quad (2.28)$$

where σ^a $(a = 1, 2, 3)$ are the Pauli matrices, the charged currents can be written as [2]

$$j_\mu^\pm = \sum_{\psi_L} 2\overline{\psi}_L \gamma_\mu T^\mp \psi_L \,. \qquad (2.29)$$

The right-chiral fields that do not participate in the weak charged currents are singlets $\psi_R = e_R, u_R, d_R$ in the trivial representation $(T^a \psi_R = 0)$ [3]. The charged currents of equation (2.22) can be written as [2]

$$\mathcal{L}_{cc} = \frac{g_2}{2} \sum_{a=1}^{2} W_\mu^a j^{\mu a} = \frac{g_2}{2\sqrt{2}} \left(W_\mu^+ j^{\mu -} + W_\mu^- j^{\mu +} \right), \quad W_\mu^\pm = \frac{1}{\sqrt{2}} \left(W_\mu^1 \mp iW_\mu^2 \right) \,. \quad (2.30)$$

The third gauge boson W_μ^3 with diagonal generator T^3 leads to a neutral current [2]

$$\mathcal{L}_{nc} = \frac{g_2}{2} W_\mu^3 j^{\mu 3}, \qquad T^3 = \frac{1}{2} \begin{pmatrix} 1 & 0 \\ 0 & -1 \end{pmatrix},$$

$$j_\mu^3 = \sum_{\psi_L} 2\overline{\psi}_L \gamma_\mu T^3 \psi_L = \overline{\nu}_L \gamma_\mu \nu_L - \overline{e}_L \gamma_\mu e_L + \overline{u}_L \gamma_\mu u_L - \overline{d}_L \gamma_\mu d_L \,. \qquad (2.31)$$

To unify weak interactions and QED, the gauge group is extended to $SU(2)_L \times U(1)_Y$. The new $U(1)_Y$ gauge group has a coupling g_1, a generator Y, called weak hypercharge, and a gauge boson B_μ. The physical gauge bosons Z_μ of the weak neutral current and A_μ of QED are superpositions of W_μ^3 and B_μ, obtained through the mixing [2]

$$\begin{pmatrix} Z_\mu \\ A_\mu \end{pmatrix} = \begin{pmatrix} \cos\theta_W & \sin\theta_W \\ -\sin\theta_W & \cos\theta_W \end{pmatrix} \begin{pmatrix} W_\mu^3 \\ B_\mu \end{pmatrix},$$

$$\begin{pmatrix} eI^z \\ -eQ \end{pmatrix} = \begin{pmatrix} \cos\theta_W & \sin\theta_W \\ -\sin\theta_W & \cos\theta_W \end{pmatrix} \begin{pmatrix} g_2 T^3 \\ -g_1 \frac{Y}{2} \end{pmatrix}. \qquad (2.32)$$

The weak mixing angle θ_W is determined by setting the electric charge [2]

$$Q = T^3 + \frac{Y}{2} \implies e = \sin\theta_W g_2 = \cos\theta_W g_1 \,. \qquad (2.33)$$

The interaction terms $\overline{\psi} i\gamma^\mu D_\mu \psi$ are built using the covariant derivative

$$D_\mu = \partial_\mu - ig_2 T^a W_\mu^a + ig_1 \frac{Y}{2} B_\mu$$

$$= \partial_\mu - i\frac{g_2}{\sqrt{2}} \left(T^+ W_\mu^+ + T^- W_\mu^- \right) - ie \left(I^z Z_\mu - QA_\mu \right), \qquad (2.34)$$

and are split into a charged current (figure 2.3a) involving only left-chiral fermions

$$\mathcal{L}_{cc} = \sum_{\psi_L} \overline{\psi}_L i\gamma^\mu \left(\partial_\mu - ig_2 T^1 W_\mu^1 - ig_2 T^2 W_\mu^2 \right) \psi_L$$

$$= \sum_{\psi_L} \overline{\psi}_L i\gamma^\mu \partial_\mu \psi_L + \frac{g_2}{2\sqrt{2}} \left(W_\mu^+ j^{\mu -} + W_\mu^- j^{\mu +} \right), \qquad (2.35)$$

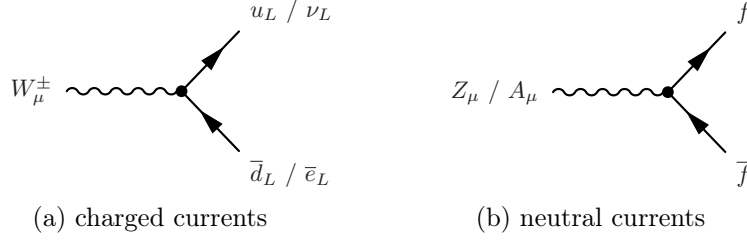(a) charged currents   (b) neutral currents

Figure 2.3: The charged and neutral currents of electroweak theory.

and a neutral current (figure 2.3b) that also involves right-chiral fermions [2]

$$
\begin{aligned}
\mathcal{L}_{nc} &= \sum_{\psi=\psi_L,\psi_R} \overline{\psi} i\gamma^\mu \left(\partial_\mu - ig_2 T^3 W_\mu^3 + i\frac{g_1}{2} Y B_\mu \right) \psi \\
&= \sum_{\psi=\psi_L,\psi_R} \overline{\psi} i\gamma^\mu \left(\partial_\mu - ie I^z Z_\mu + ie Q A_\mu \right) \psi \, .
\end{aligned}
\tag{2.36}
$$

Table 2.2: The fermions of the SM and their $\mathrm{SU(3)_c \times SU(2)_L \times U(1)_Y}$ quantum numbers.

	Q_L	u_R	d_R	L_L	ν_R $^{(*)}$	e_R
$\mathrm{SU(3)_c}$	3	3	3	1	1	1
$\mathrm{SU(2)_L}$	2	1	1	2	1	1
$\mathrm{U(1)_Y}$	$+1/3$	$+4/3$	$-2/3$	-1	0	-2

$^{(*)}$ right-chiral neutrinos ν_R are sterile (all charges $= 0$). Therefore, they are not included in the SM.

2.4 Higgs mechanism

The gauge bosons $W_\mu^\pm$, Z_μ of the weak interactions obtain masses through spontaneous symmetry breaking [3]. This is described by the gauge invariant Lagrangian

$$
\mathcal{L}_{\text{Higgs}} = (D_\mu H)^\dagger (D^\mu H) + \mu^2 |H|^2 - \frac{\lambda}{4}|H|^4 .
\tag{2.37}
$$

$H(x)$ is a complex scalar field with a potential

$$
V(H) = -\mu^2 |H|^2 + \frac{\lambda}{4}|H|^4 = \frac{\lambda}{4}\left(H^\dagger H - \frac{v^2}{2} \right)^2 + \text{const.} , \qquad v = \frac{2\mu}{\sqrt{\lambda}} ,
\tag{2.38}
$$

where v is called the vacuum expectation value. The covariant derivative is

$$
D_\mu = \partial_\mu - i\frac{g_2}{\sqrt{2}}\left(T^+ W_\mu^+ + T^- W_\mu^- \right) - ie\left(I^z Z_\mu - Q A_\mu \right) .
\tag{2.39}
$$

The field H is an $SU(2)_L$ doublet with weak hypercharge $Y = 1$ and ground state H_0 [3]

$$H(x) = \begin{pmatrix} H^+(x) \\ H^0(x) \end{pmatrix}, \quad H_0 = \frac{1}{\sqrt{2}} \begin{pmatrix} 0 \\ v \end{pmatrix}. \tag{2.40}$$

In the case $\mu^2 < 0$, $\lambda > 0$, the potential has non-trivial global minima at $|H|^2 = v^2/2$. By the choice of the ground state H_0, the $SU(2)_L \times U(1)_Y$ gauge symmetry is spontaneously broken. Due to

$$QH = \begin{pmatrix} H^+ \\ 0 \end{pmatrix} \implies QH_0 = 0, \qquad I^{\hat{a}} H_0 \neq 0 \text{ for } I^{\hat{a}} = T^\pm, I^z, \tag{2.41}$$

the symmetry group $U(1)_Q$ of Quantum Electrodynamics remains unbroken, leading to the desired symmetry breaking pattern

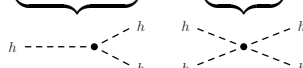$$SU(2)_L \times U(1)_Y \longrightarrow U(1)_Q \tag{2.42}$$

which generates masses for the $W_\mu^\pm$ and Z_μ bosons, while leaving the photon A_μ massless [3]. The field $H(x)$ is expanded around the ground state H_0

$$H(x) = \frac{1}{\sqrt{2}} \begin{pmatrix} 0 \\ v + h(x) \end{pmatrix} e^{iI^{\hat{a}} \phi^{\hat{a}}(x)/v}. \tag{2.43}$$

The four real scalar fields, the Higgs boson $h(x)$ and the three Goldstone bosons $\phi^{\hat{a}}(x)$, represent the radial and azimuthal field oscillations around the ground state. The Goldstone bosons can be removed from the Lagrangian by a gauge transformation with phase $\theta^{\hat{a}}(x) = -\phi^{\hat{a}}(x)/v$, called the unitary gauge [3], which turns

$$H(x) \longrightarrow \frac{1}{\sqrt{2}} \begin{pmatrix} 0 \\ v + h(x) \end{pmatrix}. \tag{2.44}$$

The potential becomes [3]

$$V(H) = \frac{1}{2} m_h^2 h^2 + \underbrace{\sqrt{\frac{\lambda}{8}} m_h h^3}_{} - \underbrace{\frac{\lambda}{16} h^4}_{}, \qquad \text{with } m_h = \sqrt{\frac{\lambda}{2}} v. \tag{2.45}$$

The Higgs boson $h(x)$ has obtained a mass m_h, proportional to the vacuum expectation value, and a new triple self-interaction with coupling proportional to m_h. From the kinetic term

$$(D_\mu H)^\dagger (D^\mu H) = \frac{1}{2} \left| \begin{pmatrix} -\frac{ig_2}{\sqrt{2}}(v+h)W_\mu^+ \\ \partial_\mu h + \frac{ig_2}{2\cos\theta_W}(v+h)Z_\mu \end{pmatrix} \right|^2$$

$$= \frac{1}{2}(\partial_\mu h)^2 + \frac{g_2^2}{4}(v+h)^2 W_\mu^+ W^{\mu -} + \frac{g_2^2}{8\cos^2\theta_W}(v+h)^2 Z_\mu Z^\mu, \tag{2.46}$$

the masses of the two charged gauge bosons $W_\mu^\pm$ and the neutral Z_μ emerge [3]. They are proportional to the vacuum expectation value v and the gauge coupling g_2, and related via the weak mixing angle θ_W:

$$m_W = \frac{g_2 v}{2}, \quad m_Z = \frac{m_W}{\cos\theta_W} = \frac{g_2 v}{2\cos\theta_W}. \tag{2.47}$$

The couplings of the new triple interactions are proportional to the gauge boson masses:

$$\frac{g_2^2}{4}(v+h)^2\,W_\mu^+ W^{\mu-} = m_W^2\,W_\mu^+ W^{\mu-} + \underbrace{g_2 m_W\,hW_\mu^+ W^{\mu-}}_{} + \underbrace{\frac{g_2^2}{4}\,h^2 W_\mu^+ W^{\mu-}}_{}$$

$$\frac{g_2^2}{8\cos^2\theta_W}(v+h)^2\,Z_\mu Z^\mu = \frac{1}{2}m_Z^2\,Z_\mu Z^\mu + \underbrace{\frac{g_2 m_Z}{2\cos\theta_W}\,hZ_\mu Z^\mu}_{} + \underbrace{\frac{g_2^2}{8\cos^2\theta_W}\,h^2 Z_\mu Z^\mu}_{}.$$

(2.48)

By construction, the photon A_μ remains massless and does not interact with the Higgs boson. The disappearance of the Goldstone bosons $\phi^{\hat{a}} = \phi^\pm, \phi^0$ is compensated by the appearance of a longitudinal polarization of the massive gauge bosons $W_\mu^\pm, Z_\mu$ [3].

2.5 Yukawa interaction

In the SM, fermion mass terms

$$\mathcal{L}_{\text{mass}} = -m_\psi\,\overline{\psi}\psi = -m_\psi\left(\overline{\psi}_L\psi_R + \overline{\psi}_R\psi_L\right) \tag{2.49}$$

are generated via spontaneous symmetry breaking in the fermion-scalar Yukawa interaction [3]

$$\mathcal{L}_{\text{Yukawa}} = -\overline{L}_L^i Y_\ell^{ij} H\ell_R^j - \overline{Q}_L^i Y_d^{ij} Hd_R^j - \overline{Q}_L^i Y_u^{ij} \widetilde{H}u_R^j + \text{h.c.} \tag{2.50}$$

with $\widetilde{H} = i\sigma^2 H^*$ the conjugate Higgs doublet, and Y_ψ ($\psi = \ell, d, u$) the Yukawa couplings. The Yukawa couplings are non-Hermitian, complex 3×3 matrices that can be decomposed in terms of a diagonal matrix λ_ψ,

$$\lambda_\ell = \text{diag}(y_e, y_\mu, y_\tau),\ \ \lambda_d = \text{diag}(y_d, y_s, y_b),\ \ \lambda_u = \text{diag}(y_u, y_c, y_t), \tag{2.51}$$

and two independent unitary matrices $U_{L,R}^\psi$

$$Y_\psi = U_L^\psi \lambda_\psi (U_R^\psi)^\dagger. \tag{2.52}$$

In the lepton sector, the fields L_L^i and ℓ_R^i can be rotated

$$L_L^i \longrightarrow (U_L^\ell)^{ij} L_L^j,\quad \ell_R^i \longrightarrow (U_R^\ell)^{ij} \ell_R^j \tag{2.53}$$

to get into the mass eigenstate basis where $\mathcal{L}_{\text{Yukawa}}^\ell$ is flavour-diagonal

$$\mathcal{L}_{\text{Yukawa}}^\ell \longrightarrow -\overline{L}_L\,(U_L^\ell)^\dagger U_L^\ell\,\lambda_\ell\,(U_R^\ell)^\dagger U_R^\ell\,\ell_R\,H + \text{h.c.}$$
$$= -\overline{L}_L^i\,\lambda_\ell^{ii}\,\ell_R^i\,H + \text{h.c.}. \tag{2.54}$$

In unitary gauge

$$H \longrightarrow \frac{1}{\sqrt{2}}\begin{pmatrix} 0 \\ v+h \end{pmatrix},\quad \widetilde{H} \longrightarrow \frac{1}{\sqrt{2}}\begin{pmatrix} v+h \\ 0 \end{pmatrix} \tag{2.55}$$
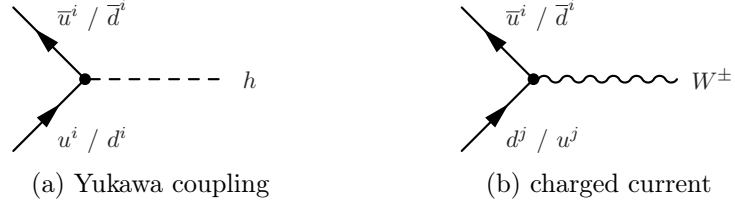
(a) Yukawa coupling   (b) charged current

Figure 2.4: In the mass eigenstate basis of both u- and d-type quarks, the CKM matrix $V = (U_L^u)^\dagger U_L^d$ is shifted from the Yukawa to the gauge sector, leading to flavour changing charged currents and diagonal Yukawa couplings [3].

this becomes

$$\mathcal{L}_{\text{Yukawa}}^\ell = -\frac{1}{\sqrt{2}}(v+h)\left(\overline{\ell}_L^i \lambda_\ell^{ii} \ell_R^i + \text{h.c.}\right)$$

$$= -m_{\ell,i}\,\overline{\ell}_L^i \ell_R^i - \underbrace{\frac{m_{\ell,i}}{v}\,h\,\overline{\ell}_L^i \ell_R^i}_{}+\text{h.c.}\,, \quad \text{with } m_{\ell,i} = \frac{\lambda_\ell^{ii}}{\sqrt{2}}\,v\,. \tag{2.56}$$

The leptons $\ell^i = e$, μ, τ have obtained masses, proportional to the Yukawa couplings $\lambda_\ell^{ii} = y_e, y_\mu, y_\tau$ and the vacuum expectation value v [3]. In the quark sector, the up and down components of the quark doublet Q_L^i have to be rotated separately

$$u_L^i \longrightarrow (U_L^u)^{ij} u_L^j, \quad d_L^i \longrightarrow (U_L^d)^{ij} d_L^j, \quad u_R^i \longrightarrow (U_R^u)^{ij} u_R^j, \quad d_R^i \longrightarrow (U_R^d)^{ij} d_R^j \tag{2.57}$$

in order to make the mass terms of both u- and d-type quarks flavour-diagonal:

$$\begin{aligned}\mathcal{L}_{\text{Yukawa}}^q \longrightarrow &-\overline{Q}_L^i \lambda_d^{ii} d_R^i H - \overline{Q}_L^i \lambda_u^{ii} u_R^i \widetilde{H} + \text{h.c.}\\ = &-\frac{1}{\sqrt{2}}(v+h)\left(\overline{d}_L^i\,\lambda_d^{ii}\,d_R^i + \overline{u}_L^i\,\lambda_u^{ii}\,u_R^i + \text{h.c.}\right).\end{aligned} \tag{2.58}$$

The separate rotation of u_L^i and d_L^i shifts the flavour changing interactions from the Yukawa to the gauge sector of the SM (figure 2.4). A non-diagonal matrix, the CKM matrix $V \equiv (U_L^u)^\dagger U_L^d$, appears in the weak charged current [3]

$$\mathcal{L}_{cc}^q = \frac{g_2}{\sqrt{2}}\left(\overline{u}_L^i \gamma^\mu d_L^i W_\mu^+ + \text{h.c.}\right) \longrightarrow \frac{g_2}{\sqrt{2}}\left(\overline{u}_L^i \gamma^\mu \left((U_L^u)^\dagger U_L^d\right)_{ij} d_L^j W_\mu^+ + \text{h.c.}\right). \tag{2.59}$$

2.6 Experimental status of the Standard Model

The predictions of the Standard Model have been confirmed by experiment and tested to high precision. The massive gauge bosons $W_\mu^\pm$ and Z_μ of the weak interaction were discovered in proton-antiproton collisions at a center of mass energy $\sqrt{s} = 540$ GeV by the UA1 and UA2 experiments at the Super Proton Synchrotron (SPS) at CERN. The first observation of $W \to e\nu$ decays in February 1983 [6], and $Z \to e^+e^-$, $Z \to \mu^+\mu^-$ decays

in May 1983 [7], was awarded the 1984 Nobel Prize in Physics. Today, combinations of measurements from Tevatron and CERN's Large Electron-Positron Collider (LEP) and Large Hadron Collider (LHC) give the W and Z boson masses $m_W = 80.379 \pm 0.012$ GeV and $m_Z = 91.1876 \pm 0.0021$ GeV [5].

In 2012, the CMS and ATLAS experiments at the LHC announced the discovery of a neutral boson with mass near 125 GeV in proton-proton collisions at $\sqrt{s} = 7$ and 8 TeV, consistent with the Higgs boson predicted in the Standard Model [8][9]. In 2013, Peter Higgs and François Englert were awarded the Nobel Prize in Physics for their theoretical work on the Higgs boson. The decays $h \to \gamma\gamma$, $h \to ZZ$, $h \to W^+W^-$, as well as the main Higgs production modes were observed in Run 1 of the LHC [10]. In Run 2, observations of the decays $h \to \tau^+\tau^-$ [11][12] and $h \to b\bar{b}$ [13][14], and the production modes Vh [13] and $t\bar{t}h$ [15][16] were made, and there is evidence for the decay $h \to \mu^+\mu^-$ [17][18]. Constraints on the $h \to c\bar{c}$ decay are also set [19]. The most precise measurement of the Higgs boson mass to date is $m_h = 125.38 \pm 0.14$ GeV [20]. All SM particle masses are listed in table 2.3.

Table 2.3: Masses of the SM particles [5].

$$
\begin{aligned}
m_u &= 2.16^{+0.49}_{-0.26} \text{ MeV} & m_e &= 510.9989461 \pm 0.0000031 \text{ keV} \\
m_d &= 4.67^{+0.48}_{-0.17} \text{ MeV} & m_\mu &= 105.6583745 \pm 0.0000024 \text{ MeV} \\
m_s &= 93^{+11}_{-5} \text{ MeV} & m_\tau &= 1.77686 \pm 0.00012 \text{ GeV} \\
m_c &= 1.27 \pm 0.02 \text{ GeV} & m_Z &= 91.1876 \pm 0.0021 \text{ GeV} \\
m_b &= 4.18^{+0.03}_{-0.02} \text{ GeV} & m_W &= 80.379 \pm 0.012 \text{ GeV} \\
m_t &= 172.76 \pm 0.30 \text{ GeV} & m_h &= 125.38 \pm 0.14 \text{ GeV} \\
& & m_{\nu_i} &\lesssim 1.1 \text{ eV }^{(*)}
\end{aligned}
$$

$^{(*)}$ The neutrinos are massless particles in the SM, but known from experiment to have non-zero masses.

3 Standard Model Effective Field Theory

The Standard Model of particle physics is a highly successful theory that accurately describes physics at the energy scale probed by the LHC. However, there is experimental evidence for phenomena not explained by the SM, such as the existence of neutrino masses [21], dark matter [22], or the recent hints of lepton flavour universality violations in $b \to s\ell\ell$ and $b \to c\ell\nu$ transitions [23]. This is motivation to consider the SM as part of a more complete theory of unknown form.

Precision measurements of the properties of SM particles and their interactions are in good agreement with the SM predictions, and there have been no direct observations of BSM physics. Therefore, it is reasonable to assume that BSM physics involves heavy particles with masses beyond the energy reach of the LHC. Such particles, while too heavy to be produced in final states at the LHC, could still appear off-shell as mediators of interactions of the light SM fields [4].

Fermi theory, discussed in section 2.3.1, describes the perturbative effect of the heavy $W^{\pm}$ bosons on the physics of light fermions, at an energy scale $\sqrt{s} \ll m_W$, in terms of an effective 4-fermion interaction

$$\mathcal{L}_{\mathrm{Fermi}} = \frac{4G_{\mathrm{F}}}{\sqrt{2}} \left(\overline{e}_L \gamma^\mu \nu_L\right)\left(\overline{u}_L \gamma_\mu d_L\right) + \mathrm{h.c.}\,, \tag{3.1}$$

with non-renormalizable mass dimension $d = 6$ operators, suppressed by two inverse powers of the mass m_W ($G_{\mathrm{F}} \sim g_2^2/m_W^2$). In analogy to this, the effect of heavy new particles (with masses above some cutoff scale Λ) on the physics of SM particles, at an energy scale $\sqrt{s} \ll \Lambda$, can be described in terms of the Standard Model Effective Field Theory (SMEFT) [24]

$$\mathcal{L}_{\mathrm{SMEFT}} = \mathcal{L}_{\mathrm{SM}}^{(d \leq 4)} + \frac{1}{\Lambda}\sum_i c_i \mathcal{Q}_i^{(5)} + \frac{1}{\Lambda^2}\sum_j c_j \mathcal{Q}_j^{(6)} + \mathcal{O}\left(1/\Lambda^3\right)\,, \tag{3.2}$$

with non-renormalizable operators $\mathcal{Q}_i^{(d)}$, built out of SM fields and invariant under $\mathrm{SU(3)_c} \times \mathrm{SU(2)_L} \times \mathrm{U(1)_Y}$ gauge transformations, and effective couplings c_i, called Wilson coefficients, suppressed by $d - 4$ inverse powers of the cutoff scale Λ.

At mass dimension $d = 5$, only one operator exists that is invariant under the SM gauge group [24]: The Weinberg operator $\mathcal{Q}_\nu^{(5)}$, which generates an effective Majorana mass term for the neutrino

$$\frac{c_\nu}{\Lambda}\,\mathcal{Q}_\nu^{(5)} = \frac{c_\nu}{\Lambda}\,L_L^T \widetilde{H}^* \widetilde{H}^\dagger L_L \xrightarrow{H \to H_0} \frac{c_\nu v^2}{2\Lambda}\,\nu_L^T \nu_L\,. \tag{3.3}$$

At $d = 6$, there are 63 operators [24]. One of them,

$$\mathcal{Q}_{\mathrm{uH}}^{(6)} = Y_u^{ij}|H|^2 \overline{Q}_L^i \widetilde{H} u_R^j + \mathrm{h.c.}\,, \tag{3.4}$$

is the subject of the analysis presented in this thesis and is discussed in the following section.

3.1 Modified Yukawa interactions

In the presence of the mass dimension 6 operator $\mathcal{Q}_{\mathrm{uH}}$ (3.4), the Yukawa interactions (2.50) of u-type quarks are modified [25]

$$\mathcal{L}^u_{\mathrm{Yukawa}} \longrightarrow \mathcal{L}^u_{\mathrm{Yukawa}} + \frac{c_{\mathrm{uH}}}{\Lambda^2} \mathcal{Q}_{\mathrm{uH}} = -\left(1 - \frac{c_{\mathrm{uH}}}{\Lambda^2}\,|H|^2\right)\left(Y_u^{ij}\,\overline{Q}^i_L\,\widetilde{H}u^j_R + \mathrm{h.c.}\right). \qquad (3.5)$$

In unitary gauge

$$\widetilde{H} \longrightarrow \frac{1}{\sqrt{2}}\begin{pmatrix} v + h \\ 0 \end{pmatrix}, \quad |H|^2 \longrightarrow \frac{1}{2}\left(v^2 + 2vh + h^2\right) \qquad (3.6)$$

and mass eigenstate basis

$$\overline{Q}^i_L Y_u^{ij} u^j_R \longrightarrow \left(\overline{u}^i_L, \overline{d}^k_L V^\dagger_{ki}\right)\lambda^{ii}_u u^i_R\,, \qquad (3.7)$$

with V the CKM matrix and $\lambda_u = \mathrm{diag}(y_u, y_c, y_t)$, this becomes

$$\begin{aligned}
\mathcal{L}^u_{\mathrm{Yukawa}} = &-\left[(v + h) - \frac{c_{\mathrm{uH}}}{\Lambda^2}\frac{1}{2}\left(v^3 + 3v^2 h + 3vh^2 + h^3\right)\right]\frac{y_{u,i}}{\sqrt{2}}\left(\overline{u}^i_L u^i_R + \mathrm{h.c.}\right) \\
= &-\left[\left(1 - \frac{c_{\mathrm{uH}}}{\Lambda^2}\frac{v^2}{2}\right)v + \left(1 - \frac{c_{\mathrm{uH}}}{\Lambda^2}\frac{3v^2}{2}\right)h\right]\frac{y_{u,i}}{\sqrt{2}}\left(\overline{u}^i_L u^i_R + \mathrm{h.c.}\right) \\
&+ \left(\text{terms proportional to } h^2\,\overline{u}^i u^i \text{ and } h^3\,\overline{u}^i u^i\right).
\end{aligned} \qquad (3.8)$$

The quark masses m_u, m_c, m_t and the Yukawa couplings y_u, y_c, y_t receive corrections of order $c_{\mathrm{uH}} v^2 / \Lambda^2$ [25].

4 The CMS Detector and Event Reconstruction

The LHC at CERN is the largest and most powerful particle collider to date, located beneath the Swiss-French border near Geneva in a tunnel 27 km in circumference. Several detectors are placed around the four interaction points, where every 25 ns two proton beams collide head-on at a center of mass energy $\sqrt{s} = 13$ TeV. The four main experiments are *ALICE* [26], *ATLAS* [27], *CMS* [28], and *LHCb* [29].

The CMS (Compact Muon Solenoid) detector is a multi-purpose detector and is located close to Cessy, France. CMS and the LHC have been in operation since 2010. The CMS experiment collected 5.6 fb^{-1} of data at a center of mass energy $\sqrt{s} = 7$ TeV and 21.8 fb^{-1} at $\sqrt{s} = 8$ TeV during Run 1 of the LHC (2010-2013), and 137 fb^{-1} at $\sqrt{s} = 13$ TeV during Run 2 (2015-2018). The LHC is currently restarting operation for Run 3, enabling CMS to collect another 150 fb^{-1} of data at $\sqrt{s} = 13.6$ TeV until 2025. From 2026 to 2028, the LHC is scheduled for an upgrade to operate at a much higher instantaneous luminosity (High-Luminosity LHC, HL-LHC) for another twelve years. The integrated luminosity collected by the end of the HL-LHC programme is expected to be 3000 fb^{-1} and data taking is scheduled to start in 2029 [30].

4.1 Coordinate system and relevant variables

The coordinate system used by CMS has its origin at the collision point in the middle of the detector, the x-axis pointing towards the center of the LHC, the y-axis pointing vertically upwards, and the z-axis pointing along the beam direction. In the x-y plane, the azimuthal angle φ is measured from the x-axis and the distance from the origin is denoted by r. The polar angle ϑ is measured from the z-axis. The pseudorapidity η is defined as [28]

$$\eta \equiv -\ln\left(\tan\frac{\vartheta}{2}\right). \tag{4.1}$$

The pseudorapity η and azimuthal angle φ are used to define a measure of angular separation between particles, ΔR, which is invariant under Lorentz boosts along the beam axis in the massless limit, and defined as [5]

$$\Delta R \equiv \sqrt{(\Delta\varphi)^2 + (\Delta\eta)^2}. \tag{4.2}$$

Hard scattering events are head-on collisions of individual partons (quarks and gluons), each carrying a fraction of the energy of the respective proton according to their parton distribution function. This means that the momenta along the beam axis of the interacting partons are unknown and net momentum can only be constrained in the plane

transverse to the beam axis (x-y plane). It is therefore customary to express momenta in terms of the transverse momentum p_T, the azimuthal angle φ, and the pseudorapidity η. The presence of invisible particles, for example neutrinos, that escape the detector unnoticed, can be inferred from a momentum inbalance in the x-y plane. Their net momentum is equal to the missing transverse energy $E_\mathrm{T}^\mathrm{miss}$, defined as

$$\mathbf{E}_\mathrm{T}^\mathrm{miss} \equiv -\sum_i \mathbf{p}_\mathrm{T}^i \,, \tag{4.3}$$

where the sum runs over all visible final state particles [5].

4.2 CMS detector

The innermost component of the CMS detector (pictured schematically in figure 4.1), surrounding the interaction point, is the tracking detector. It is designed to provide a precise measurement of the trajectories of charged particles, in order to reconstruct interaction vertices and determine particle momenta. The tracker consists of four barrel layers of silicon pixel detectors placed close to the proton beam, at radii between 2.9 cm and 16.0 cm, and ten barrel layers of silicon strip trackers extending out to a radius of 1.1 m. Both pixel and strip trackers are completed by endcap sections on each side of the barrel, extending the pseudorapidity range of the tracker up to $|\eta| < 2.5$ [28].
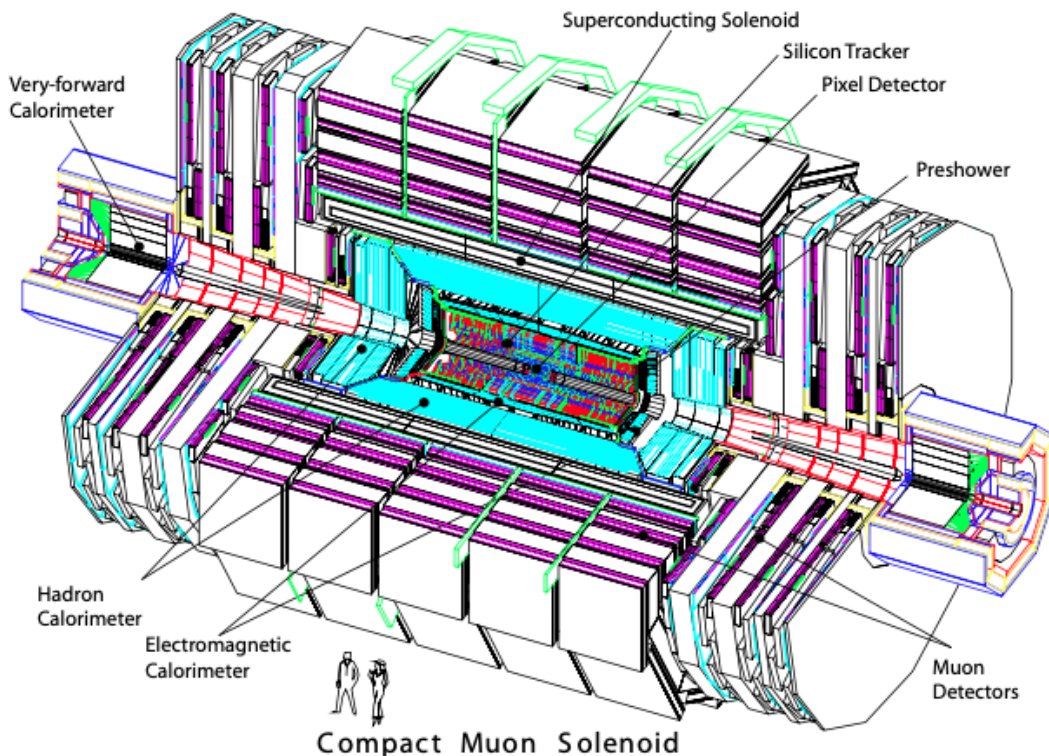

Figure 4.1: The CMS detector. Source: [28].

The LHC collides proton beams consisting of bunches of $\sim 10^{11}$ protons at a rate of one bunch crossing per 25 ns. Per bunch crossing, there are around 40 inelastic collisions. In order to deal with the huge number of particles emerging from the interaction region every 25 ns, the inner tracker needs high granularity and a fast response. At the same time, it needs to sustain high levels of radiation caused by the intense particle flux close to the interaction point. These requirements on granularity, time resolution, and radiation hardness lead to a tracker design based on silicon detector technology [28].

The four barrel layers and three endcap disks of the pixel detector consist of a total of 1856 sensor modules, each made up of 160×416 pixels. The standard pixel size is $100 \times 150 \, \mu m^2$ [31]. The high granularity of the pixel detector with its 124 million readout channels makes it possible to reconstruct interaction vertices with a position resolution of $10 - 12 \, \mu m$ in each spatial dimension [32].

The strip detector consists of a total of 9.3 million silicon strips in ten barrel layers and twelve endcap disks. The hit resolution in the barrel strip detector varies between $10 - 50$ μm, increasing with pseudorapidity and distance from the interaction point [32].

The relative resolution of the momentum measurement in a tracking detector improves linearly with the strength of the magnetic field and quadratically with the length of the measured track, and deteriorates linearly with the transverse momentum of the particle. The quadratic dependence of the momentum resolution on the length of the measured tracks is one of the reasons for the large size of detectors in high-energy physics. With an outer radius of 1.1 m, the CMS tracker is rather small. To compensate for this, a strong magnetic field is needed. This is achieved using a superconducting solenoid with a diameter of 6 m and 12.5 m length, providing a magnetic field of 3.8 T [28].

An electromagnetic calorimeter (ECAL) and a hadronic calorimeter (HCAL) are placed between the inner tracker and the superconducting solenoid. The ECAL is used to measure the energy and direction of electrons and photons, which induce electromagnetic showers that are absorbed in the ECAL material. It is a homogeneous calorimeter made of 61200 lead tungstate crystals in the barrel region, closed by 7324 crystals in both endcaps that extend the pseudorapidity coverage up to $|\eta| < 3.0$. The high density of the lead tungstate crystals allows for fast readout, fine granularity, and high radiation hardness. A preshower detector, a two layer sampling calorimeter with high granularity, is placed in front of the endcap crystals. Its aim is to distinguish photons from neutral pions that decay into a pair of photons [28].

The HCAL measures the energy and direction of hadrons. As its size is restricted between the outer radius of the ECAL (1.77 m) and the inner radius of the solenoid (2.95 m), a tail catcher is placed outside the solenoid to ensure full absorption of the hadronic shower. The HCAL is a sampling calorimeter made of alternating layers of steel and brass absorbers and plastic scintillators. Barrel and endcap sections cover the pseudorapidity range up to $|\eta| < 3.0$, and a forward calorimeter placed 11.2 m from the interaction point extends the coverage up to $|\eta| < 5.2$ [28].

The muon detection system is the outermost part of the detector. As the name Compact Muon Solenoid implies, muon detection is of central importance to CMS. Muons are easy to identify and are less affected than electrons by radiative losses in the detector material, making it possible to measure their momenta with high precision. The muon system uses

three different types of gaseous tracking detectors. The pseudorapidity region $|\eta| < 1.2$ is covered by drift tube (DT) chambers organized in four stations, each containing eight chambers that measure the muon coordinates in the transverse plane, and, in case of the first three stations, an additional four chambers which provide a measurement in the direction of the beam axis. In the two endcap regions, four stations of cathode strip chambers (CSC) cover the $0.9 < |\eta| < 2.4$ region. With their fast response and fine segmentation, the CSCs are well suited for the high muon rates and non-uniform magnetic field in the endcap regions [28].

The drift tube and cathode strip chambers in the barrel and endcap regions are complemented by a dedicated muon trigger system, consisting of resistive plate chambers (RPC) that provide a fast measurement with good time resolution, but coarser position resolution than the DTs and CSCs. There are six layers of RPCs embedded in the barrel muon system, and three layers in each of the endcaps [28].

4.3 Trigger system

The CMS detector observes an event rate of approximately 10^9 collisions per second. Only a small fraction of these collisions contain events that are of interest to the CMS physics programme. The trigger system has to select the interesting events and reduce the event rate to a few hundred events per second for storage and subsequent analysis [28].

This is done in two steps. The Level-1 Trigger (L1) is implemented in hardware and uses information from the calorimeters and the muon detectors. It must decide whether to reject an event or pass it on to the High-Level Trigger (HLT) within 4 μs of the collision [33]. The HLT is implemented in software and has access to the full data output of the detector. Event selection criteria are applied to reconstructed physical objects. The CPU power available to the HLT allows an average processing time of 175 ms per event at an L1 input rate of 100 kHz [33].

4.4 The High-Luminosity LHC

Starting in 2029, the LHC is expected to produce more than 250 fb^{-1} of data per year, more than the integrated luminosity of Runs 1-2 combined. To achieve this, the proton beams have to be more intense and more focused than they currently are. More powerful superconducting magnets on both sides of the CMS detector will focus the particle beams and crab cavities will be used to tilt the beams before the interaction point, increasing the rate of collisions by enlarging the overlap area of the two beams [30].

The upgrade to the HL-LHC brings significant challenges for the detector design. With increased luminosity, an average of 140 additional proton-proton collisions (pile-up) will be produced per bunch crossing, compared to around 40 at present. This increase in pile-up makes it necessary to improve the granularity and time response of all detector parts. The pseudorapidity coverage of the inner tracker will be increased and the L1 Trigger system will be upgraded to include tracker information. Additionally, the radiation

hardness of the detector components will have to be increased in order to sustain much higher radiation doses without degrading [34].

4.5 Event reconstruction

Final state particles originate from the beam interaction point and travel outward through the different elements of the detector (figure 4.2). In the tracker, charged particles leave hits in the sensitive layers. A track finding algorithm reconstructs their trajectory starting from a seed of two or three hits, then extrapolating to the next tracker layers, looking for additional hits that can be assigned to the track candidate. This is done in multiple iterations, first for the tracks easiest to find, then removing the hits associated with succesfully reconstructed tracks, reducing the complexity of subsequent iterations. Tracks that appear to originate from the same interaction vertex are then clustered together and the position of each vertex is fitted. The curvature of the trajectories of charged particles in the magnetic field is used to determine the particle momenta [32].

In the ECAL, electrons and photons are absorbed and their energy and direction are determined from the corresponding electromagnetic showers. Hadrons leave a signal in the ECAL as well and are then fully absorbed in the HCAL, where their energy and direction are measured [35].
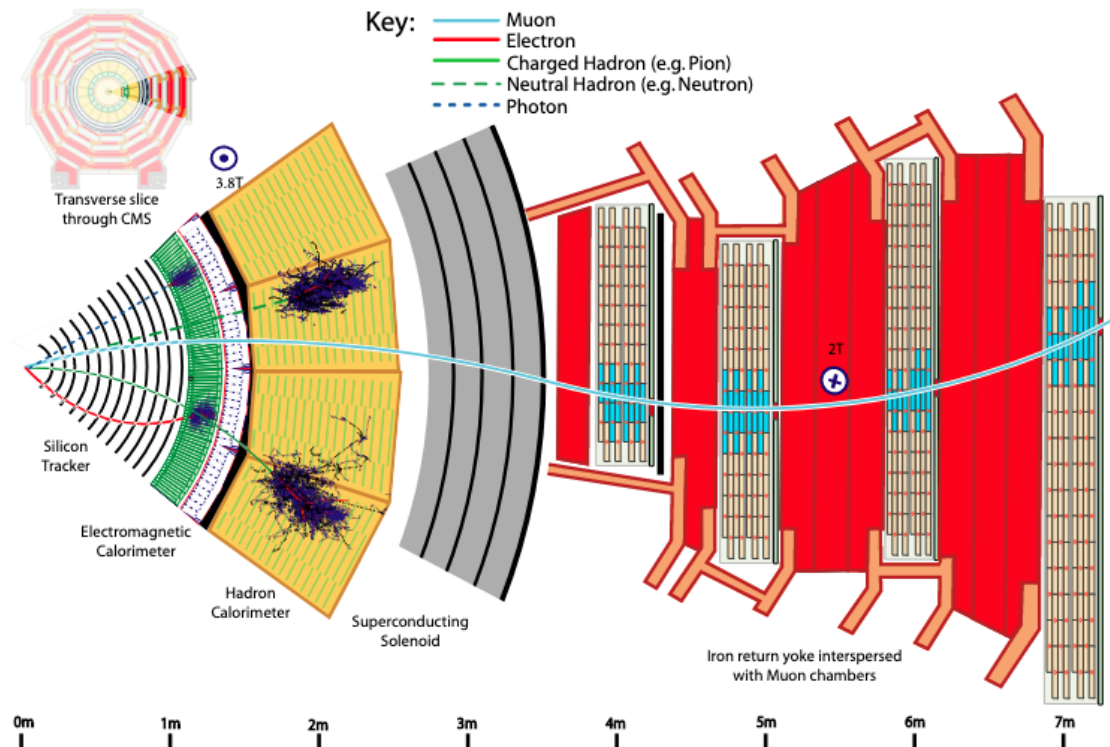

Figure 4.2: A transverse slice of the CMS detector showing the interactions of different types of particles. Interaction point on the left. Source: [35].

Muons cross the calorimeters with little interaction and are the only particles to leave tracks in the outermost detection layers, the muon detectors. Neutrinos escape undetected [35].

The particle-flow (PF) algorithm reconstructs physical objects such as jets, photons, electrons, and muons from raw detector data. It identifies each final state particle using information from all subdetectors and reconstructs the particle properties on the basis of this identification [35].

4.5.1 Muons

Tracks in the muon detectors and in the inner tracker are combined either outside-in or inside-out. *Global muon* reconstruction (outside-in) is designed for high transverse momentum muons, $p_T > 200$ GeV. A track in the muon detector is matched to a track in the inner tracker and a combined fit is performed on the two tracks. The inside-out approach is more efficient for low-p_T muons. Tracks from the inner tracker are propagated to the muon detectors. If at least one muon detector segment matches the extrapolated track, the track qualifies as a *tracker muon*. Global muons and tracker muons sharing the same track are merged into a single muon candidate [35].

A set of selection criteria are applied to muon candidates, based on quality parameters from the muon reconstruction and information from other subdetectors. There are several muon identification (ID) types, each optimized for different sources of muons, such as the *medium muon ID* optimized for muons originating from the primary vertex (prompt muons) or from heavy flavour decays, the *tight muon ID* that aims to suppress muons from decay in flight and muons faked by hadrons that pass through the HCAL, or the *soft muon ID* optimized for low-p_T muons for B-physics analyses. These ID types are based on variables such as the number of hits in the inner tracker and the muon stations, the track fit quality, the degree of matching between inner tracker and muon detector tracks, and the compatibility of the track with the reconstructed primary vertex. For muons with $p_T > 20$ GeV, the identification efficiency exceeds 96% over the entire pseudorapidity range of the detector [36].

Muon isolation requirements help distinguish between prompt muons and muons from weak decays within jets. The isolation is evaluated by summing up the transverse momenta of charged particles and energy of neutral hadrons and photons within a cone of $\Delta R < 0.3$ or 0.4 around the muon trajectory. The pileup-corrected relative isolation for muons is defined as

$$I^\mu_{\text{rel}} = \frac{1}{p_T^\mu} \left[\sum_{\text{charged}} p_T + \max\left(0, \sum_{\text{neutral}} p_T - 0.5 \sum_{\text{charged}} p_T^{\text{PU}}\right) \right], \qquad (4.4)$$

where $\sum_{\text{charged}} p_T$ and $\sum_{\text{charged}} p_T^{\text{PU}}$ refer to the sums over charged particles associated with the primary vertex or with pileup (PU) vertices respectively. The factor 0.5 corresponds to the approximate ratio of neutral particle to charged hadron production in inelastic proton-proton collisions [35]. Tight and loose working points are defined to achieve efficiencies of 95% and 98% respectively. For $\Delta R < 0.3$ ($\Delta R < 0.4$), the tight and loose working points are $I^\mu_{\text{rel}} < 0.05$ and 0.10 ($I^\mu_{\text{rel}} < 0.15$ and 0.25) [36].

4.5.2 Electrons

In the *ECAL-based* approach to electron reconstruction, the energy and position of energy clusters in the ECAL are used to find compatible hits in the inner tracker. Hadrons are rejected by requiring the sum of energies measured in HCAL cells within a distance $\Delta R < 0.15$ of the electron candidate to be less than 10% of the energy in the ECAL cluster. In the *tracker-based* approach, tracks are propagated to the ECAL and matched to the closest energy cluster. If the ratio of track p_{T} and cluster E_{T} is close to 1, the track is identified as an electron [35].

The large probability of electrons to lose energy through bremsstrahlung in the tracker material makes it difficult to reconstruct clean electron tracks across the whole tracker, leading to a lower reconstruction efficiency and larger uncertainties than in the muon case. Multivariate electron ID classifiers that combine information about the track quality, momentum loss between the innermost and outermost layer of the tracker, hadron activity near the electron trajectory, ECAL cluster shape, relative isolation and kinematic properties significantly reduce misidentification rates. Three working points are defined to identify electrons with efficiences of 70%, 80%, and 90% [37].

4.5.3 Photons

In the inner tracker, electrons often emit bremsstrahlung photons and photons often convert to electron-positron pairs. Therefore, the properties of photon candidates are similar to those of electrons, and the reconstruction of photons is done in combination with electron reconstruction. An ECAL energy cluster with no matching track in the inner tracker is identified as a photon if the sum of energy deposits in nearby HCAL clusters does not exceed 10% of its energy [35]. Multivariate photon ID classifiers are based on similar principles as in the electron case and achieve comparable efficiencies and misidentification rates [37].

4.5.4 Jets

A free quark or gluon fragments in a cascade of soft, collinear branchings. Due to colour confinement, these fragments hadronize, resulting in *jets*, collimated bundles of hadrons flying in the direction of the original quark or gluon. The PF algorithm identifies HCAL clusters without a matching track as neutral hadrons and HCAL clusters with one or several matching tracks and a matching ECAL cluster as charged hadrons [35]. The anti-k_{T} algorithm [38] then clusters the individual hadrons to jets. Usually, jets are produced using the anti-k_{T} algorithm with a distance parameter $R = 0.4$. Another class of jets, referred to as *AK8 jets* or *FatJets*, are produced with a distance parameter $R = 0.8$. These AK8 jets are suited for the reconstruction of hadronically decaying, highly boosted heavy particles like $W^{\pm}$, Z, Higgs bosons, or top quarks [39].
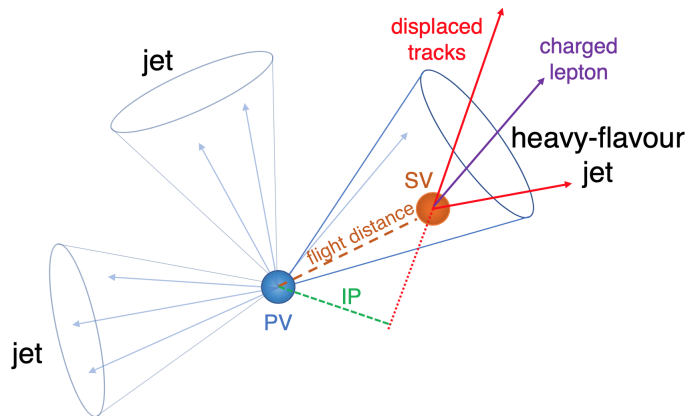
Figure 4.3: The decay of a B or D hadron in a heavy-flavour jet resulting in displaced particle tracks with a secondary vertex. Source: [40].

Heavy-flavour jet tagging

In general, it is unknown which type of quark or gluon a jet originated from. However, jets originating from heavy quarks, b- and c-jets, can be identified with high efficiency, using variables connected to the properties of the B or D hadrons present in these jets. B and D hadrons have lifetimes of $\sim$1.5 ps and $\sim$1 ps respectively. Depending on their momentum, they travel distances of a few mm to $\sim$1 cm before decaying, giving rise to tracks that are discplaced with respect to the primary interaction vertex (figure 4.3). Additionally, B and D hadron decays are more likely to produce muons or electrons, and, due to the large mass of these hadrons, their decay products are less collinear to the jet axis [40].

The DeepCSV (deep combined secondary vertex) b-tagging algorithm uses a deep neural network and combines information of displaced tracks with information on secondary vertices associated with the jet to identify jets originating from b-quarks. For the identification of c-jets a similar algorithm is used, but due to the shorter lifetime and lower mass of D hadrons, c-tagging is more challenging. Three working points (loose, medium, tight) are defined corresponding to thresholds on the discriminator that lead to misidentification probabilities of 11%, 1.1%, and 0.1% for light-flavour jets (u-, d-, s quarks, gluons). The identification efficiency for b-jets at these working points is 84%, 68%, and 50% respectively. For c-jets, the efficiency is considerably lower at 41%, 12%, and 2.4% [40].

Tagging of hadronically decaying heavy particles

AK8 jets originating from hadronic decays of highly boosted top quarks, $W^{\pm}$, Z, or Higgs bosons can be identified using properties such as the jet mass and the number of subjets, which is expected to be two for $W^{\pm}$, Z, h bosons (which decay to two quarks), and three for t quarks (which decay to a b quark and a W boson, which then decays to two quarks) [39].

The DeepAK8 algorithm is a multiclass classifier that uses a total of 42 variables for each jet constituent particle, as well as the properties of secondary vertices as input. Particle properties, such as the p_T, charge, energy deposit, and angular separation between the particle and the jet axis, help the algorithm extract information on the jet substructure. Measurements from the inner tracker are used to extract information on the presence of b- or c-quarks [39].

Different working points are defined on the DeepAK8 classifiers that lead to misidentification rates of 2.5%, 1%, 0.5%, and 0.1% for quarks (excluding top quarks) and gluons from QCD multijet production. Figure 4.4, taken from reference [39], shows the signal efficiency versus misidentification rate (background efficiency) of several identification algorithms for hadronically decaying top quarks and W bosons.
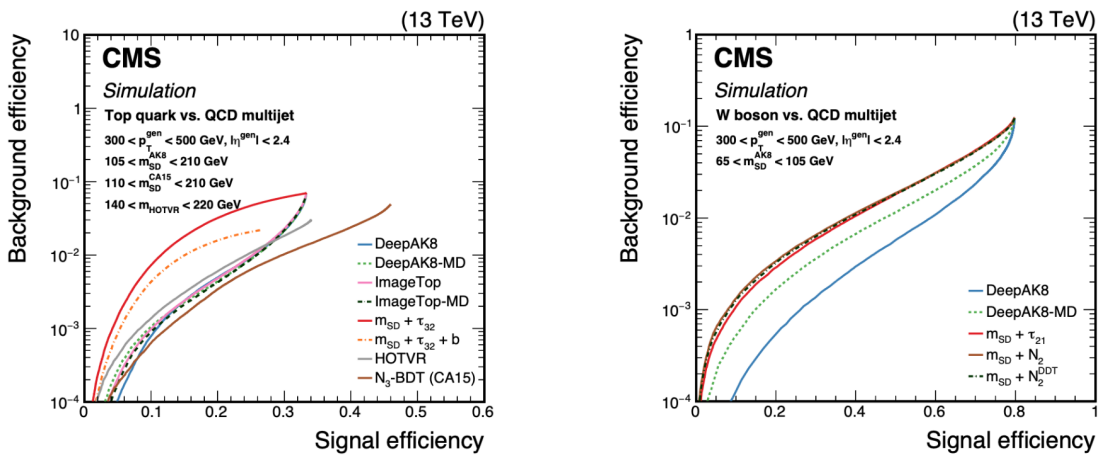
Figure 4.4: Signal efficiency versus misidentification rate (background efficiency) of identification algorithms for hadronically decaying top quarks (left) and W bosons (right) generated with 300 GeV $< p_T <$ 500 GeV. The DeepAK8 algorithm, discussed in the text, is shown in blue. Source: [39].

4.5.5 Taus

Unlike electrons and muons, τ leptons are very short-lived and can only be reconstructed from their decay products. The branching fraction of the leptonic decay mode to a muon/electron and two neutrinos is around 35%. The other 65% are hadronic decays to one neutrino and a few hadrons. Hadronic τ decays can be distinguished from quark and gluon jets by the number of decay products and their isolation and collimation. The algorithms used by CMS for reconstruction and identification of hadronic τ decays achieve efficiencies of 50% to 60% and misidentification rates between the permille and percent level [41].

5 The Signal Process pp → tjVV and Backgrounds

A modification of the Yukawa interaction by the SMEFT operator $\mathcal{Q}_{\text{uH}}$, discussed in section 3.1, induces a quadratic energy growth in the five point amplitude $\mathcal{M}(bV_l \to tV_lV_l)$ involving three longitudinal vector bosons, a top quark, and a b quark. In non-unitary gauge, the longitudinal polarizations $W_l^\pm$, Z_l of the gauge bosons reappear explicitly as the Goldstone bosons $\phi^\pm$, ϕ^0 in the scalar fields [1]

$$H = \begin{pmatrix} H^+ \\ H^0 \end{pmatrix} = \frac{1}{\sqrt{2}} \begin{pmatrix} \phi^+ \\ v + h + i\phi^0 \end{pmatrix}, \quad \widetilde{H} = \begin{pmatrix} H^{0\,*} \\ -H^- \end{pmatrix} = \frac{1}{\sqrt{2}} \begin{pmatrix} v + h - i\phi^0 \\ -\phi^- \end{pmatrix}, \tag{5.1}$$

and the operator becomes

$$
\begin{aligned}
\mathcal{Q}_{\text{uH}}\big|_t &= y_t |H|^2 \left(\bar{t}_L, \overline{d}_L^i V_{i3}^\dagger\right) \widetilde{H} \, t_R + \text{h.c.} \approx y_t |H|^2 \left(\bar{t}_L, \bar{b}_L\right) \widetilde{H} \, t_R + \text{h.c.} \\
&= \frac{y_t}{2\sqrt{2}} \left[(v+h)^2 + \phi^+\phi^- + (\phi^0)^2\right] \left[\left(v + h - i\phi^0\right) \bar{t}_L t_R - \phi^- \bar{b}_L t_R + \text{h.c.}\right].
\end{aligned}
\tag{5.2}
$$

The term

$$\frac{y_t}{2\sqrt{2}} \left(\phi^+\phi^- + (\phi^0)^2\right) \left(\phi^- \bar{b}_L t_R + \text{h.c.}\right) \tag{5.3}$$

contributes to the amplitude $\mathcal{M}(bV_l \to tV_lV_l)$, $V = W^\pm, Z$, at tree level with effective coupling $\sim c_{\text{uH}}/\Lambda^2$. Dimensional analysis indicates that at high energy, $E \gg m_W, m_Z$, m_h, m_t, the BSM and SM contribution to this amplitude scale as [1]

$$\frac{\mathcal{M}^{\text{BSM}}}{\mathcal{M}^{\text{SM}}} \sim \frac{E^2}{\Lambda^2}. \tag{5.4}$$

In proton-proton collisions, the amplitude $\mathcal{M}(bV_l \to tV_lV_l)$ contributes to processes with a final state of two longitudinal vector bosons, a top quark and a forward jet (figure 5.1):

$$pp \to tjV_lV_l', \quad \text{where} \ \ V_lV_l' = W_l^\pm W_l^\pm, \ W_l^\pm W_l^\mp, \ W_l^\pm Z_l, \ Z_lZ_l. \tag{5.5}$$
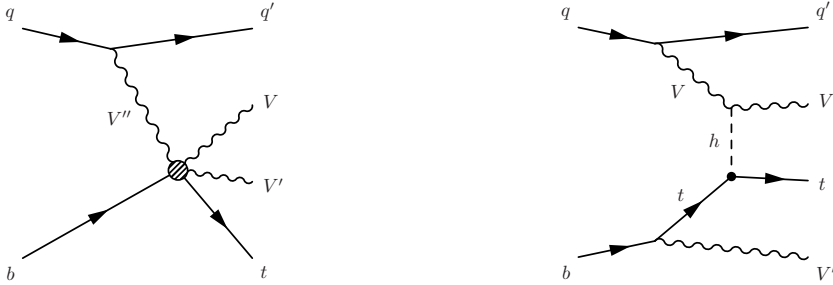

Figure 5.1: The process $pp \to tjV_lV_l'$ is sensitive to the operator $\mathcal{Q}_{\text{uH}}$ that modifies the top quark Yukawa coupling. The Feynman diagram in non-unitary gauge is shown on the left and one of the possible diagrams in unitary gauge on the right.

In the EFT framework, the cross section of this process can be expressed as the sum

$$\sigma = \sigma_{\text{SM}} + \frac{c_{\text{uH}}}{\Lambda^2}\sigma_{\text{int.}} + \frac{c_{\text{uH}}^2}{\Lambda^4}\sigma_{\text{BSM}} \qquad (5.6)$$

of the Standard Model cross section σ_{SM}, a term σ_{int} due to interference of the SM and BSM amplitudes, and the SM-independent σ_{BSM}.

5.1 Signal channel

The channel studied is $pp \to tjW^+W^-$, where one W boson decays hadronically ($W \to qq'$), the other leptonically ($W \to \ell\nu$). The top quark decays either hadronically ($t \to bW \to bqq'$) or leptonically ($t \to bW \to b\ell\nu$). The reconstructed final state consists of a forward jet, a W-tagged AK8 jet, and, depending on the top quark decay mode, either a top-tagged AK8 jet, one isolated lepton, and missing energy from one neutrino; or a b-tagged jet, two isolated leptons, and missing energy from two neutrinos. In the following, the former is referred to as the 1ℓ event category, and the latter as the 2ℓ category.

Monte Carlo (MC) samples of the signal process are generated using MadGraph 5 [42] at leading order (LO). For the BSM contributions at non-zero c_{uH}, SMEFTsim v2.1 [43] is used. In SMEFTsim, the top quark Yukawa coupling scales with c_{uH} as [44]

$$y_t \longrightarrow y_t(1 + \delta y_t), \quad \text{with } \delta y_t = \frac{v^2}{\Lambda^2}c_{\text{uH}} \approx 0.0605\,c_{\text{uH}}, \;\; \Lambda = 1\,\text{TeV}. \qquad (5.7)$$

In order to study the dependence of the cross section on c_{uH}, three $pp \to tjW^+W^-$ samples are generated at $c_{\text{uH}} = 0, 40, 80$. An additional pure BSM sample is obtained by setting the Wilson coefficient to a very high value, $c_{\text{uH}} = 10000$. The decay of the top quark is simulated with Pythia [45], those of the W bosons with MadSpin [46].
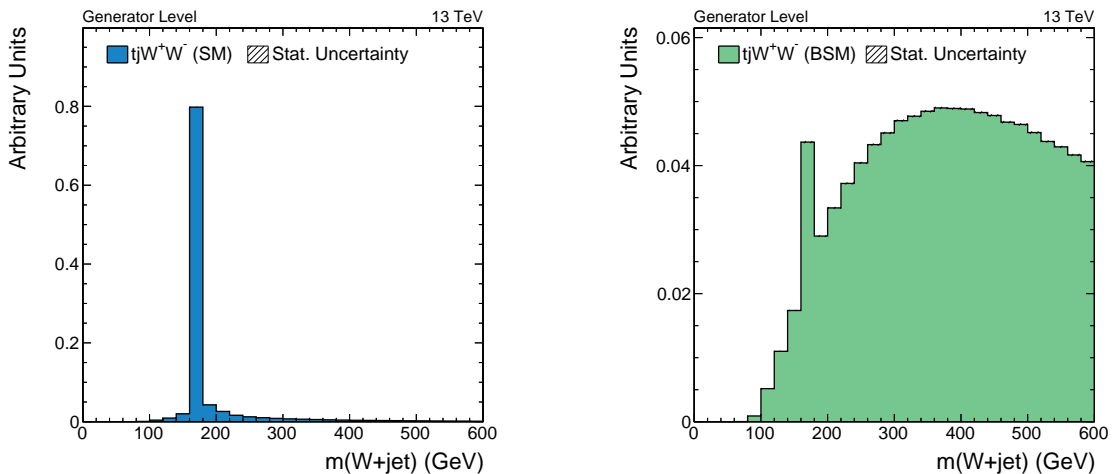

Figure 5.2: Invariant mass of the W boson + jet system (W^+ if the jet has negative electric charge and vice versa) in the SM (left) and BSM (right) contributions to $pp \to tjW^+W^-$. In $pp \to t\bar{t}W^\pm \to tbW^+W^-$ events, this reconstructs the top quark mass.

A large part of the SM contribution to the tjW^+W^- final state comes from $pp \rightarrow t\bar{t}W^\pm \rightarrow tbW^+W^-$. For a top quark transverse momentum $p_T^t > 100$ GeV, these $t\bar{t}W$ events make up around 93% of the tjW^+W^- final state. On the other hand, less than 4% of the BSM contribution to the tjW^+W^- final state comes from $t\bar{t}W$ events. This is illustrated in figure 5.2, which shows the invariant mass of the W boson + jet system in the SM and BSM contributions to the signal process at generator level.

As the b-jet in $pp \rightarrow t\bar{t}W^\pm \rightarrow tbW^+W^-$ is usually at low pseudorapidity, the forward jet requirement plays a key role in distinguishing $t\bar{t}W$ events from genuine $pp \rightarrow tjW^+W^-$ events and therefore in increasing the sensitivity of the signal to c_{uH}. In addition, the quadratic energy growth of the BSM contribution to $\mathcal{M}(bV_l \rightarrow tV_lV_l)$ can be exploited by setting high p_T requirements on the reconstructed top-tagged jet, W-tagged jet, and leptons. Figures 5.3 and 5.4 show the kinematic distributions of the top quark and W boson transverse momentum and jet pseudorapidity in the SM and BSM contributions to the signal at generator level.
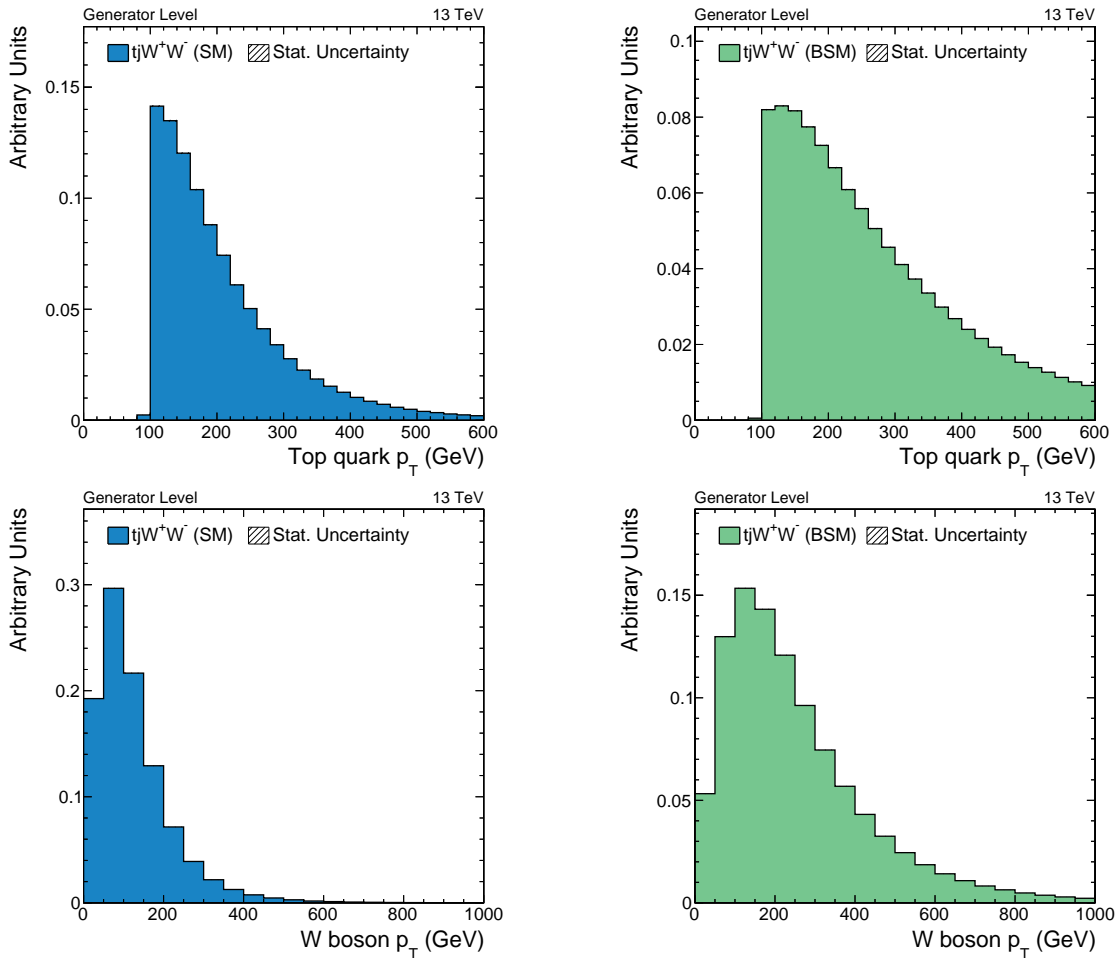

Figure 5.3: Top quark (top) and W boson transverse momentum (bottom) in the SM (left) and BSM (right) contributions to $pp \rightarrow tjW^+W^-$.
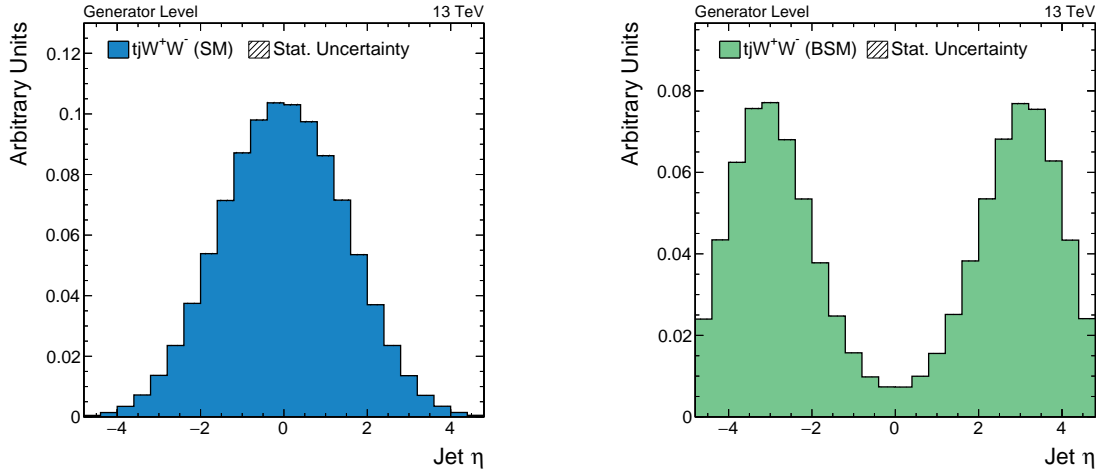
Figure 5.4: Jet pseudorapidity in the SM (left) and BSM (right) contributions to $pp \to tjW^+W^-$.

The signal cross section is shown as a function of c_{uH} in figure 5.5 and table 5.1, for three different sets of cuts:

$$
\begin{aligned}
&\text{cut 1:} \quad p_{\mathrm{T}}^t > 100 \,\text{GeV}, \\
&\text{cut 2:} \quad p_{\mathrm{T}}^t > 350 \,\text{GeV}, \\
&\text{cut 3:} \quad p_{\mathrm{T}}^t > 350 \,\text{GeV}, \, |\eta_j| > 2.4 \,.
\end{aligned}
\tag{5.8}
$$

As expected, the c_{uH} dependence of the cross section grows with tighter cuts, which means the sensitivity to c_{uH} increases in events with high transverse momenta and forward jets.

Table 5.1: Signal cross section for the three sets of cuts listed in equation (5.8).

	σ (pb)
cut 1	$2.48 \times 10^{-1} \, (1 - 0.000101 \, c_{\mathrm{uH}} + 0.0000184 \, c_{\mathrm{uH}}^2)$
cut 2	$2.79 \times 10^{-2} \, (1 + 0.000306 \, c_{\mathrm{uH}} + 0.0000407 \, c_{\mathrm{uH}}^2)$
cut 3	$8.00 \times 10^{-4} \, (1 + \ 0.00438 \, c_{\mathrm{uH}} \ + 0.00123 \, c_{\mathrm{uH}}^2)$

5.2 Background processes

Any physics process with a final state similar to the signal has to be considered as a background. The contribution of the various background processes is estimated using the MC samples listed in table 5.2. In this section, kinematic distributions of the relevant backgrounds at generator level are compared to those of the signal. Only events with the `HLT_IsoMu24` or `HLT_Ele35_WPTight_Gsf` trigger are considered. This is one of the selections applied later on in the analysis, and will be discussed in more detail in chapter 6.
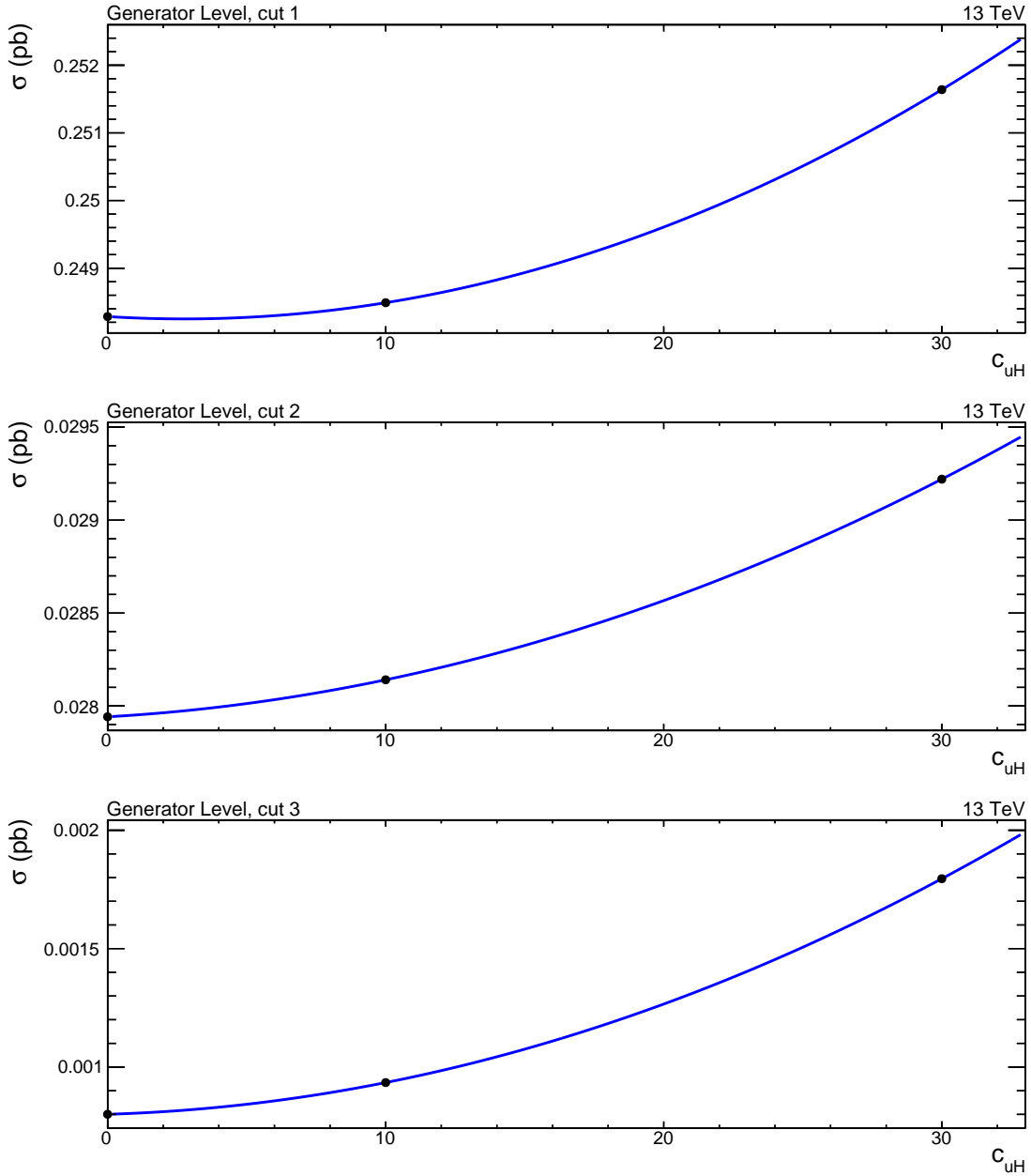
Figure 5.5: Signal cross section (in pb) as a function of the Wilson coefficient c_{uH} for the three sets of cuts listed in equation (5.8).

5.2.1 Top quarks

The biggest background contribution comes from $t\bar{t}$+jets events with at least one leptonic top quark decay. If two jets in the event are misreconstructed as a W boson, semileptonic $t\bar{t}$ decays ($t\bar{t} \to bjj + b\ell\nu$) contribute to the 1ℓ event category, and fully leptonic decays ($t\bar{t} \to b\bar{b} + \ell^+\ell^- + \nu\bar{\nu}$) contribute to the 2ℓ category. There, the $t\bar{t}$ background can be greatly reduced by rejecting all events with two opposite charge leptons. A W-tagger with a low misidentification rate can further reduce the $t\bar{t}$ contribution.

The production of a $t\bar{t}$-pair in association with one or two vector bosons ($t\bar{t}W^{\pm}$, $t\bar{t}Z$, $t\bar{t}W^{+}W^{-}$, $t\bar{t}W^{\pm}Z$, $t\bar{t}ZZ$) is much rarer than $t\bar{t}$+jets, but the signatures of these processes are quite similar to the signal. Rejecting events with extra leptons can help to reduce this background.

$pp \to tW$ events can pass the event selection in the 1ℓ category if a jet fakes a lepton or is misidentified as an additional W boson. The $pp \to tZ$ cross section is around two orders of magnitude smaller than $pp \to tW$ and mostly contributes to the 2ℓ event category, where both tZ and tW can be rejected effectively by vetoing events with oppositely charged leptons.

As shown in figure 5.6, the top quark and W/Z boson p_{T} spectra of these backgrounds fall more quickly than those of the signal, the majority of jets is at small $|\eta|$, and in events with two leptons, the leptons usually have opposite electric charges.
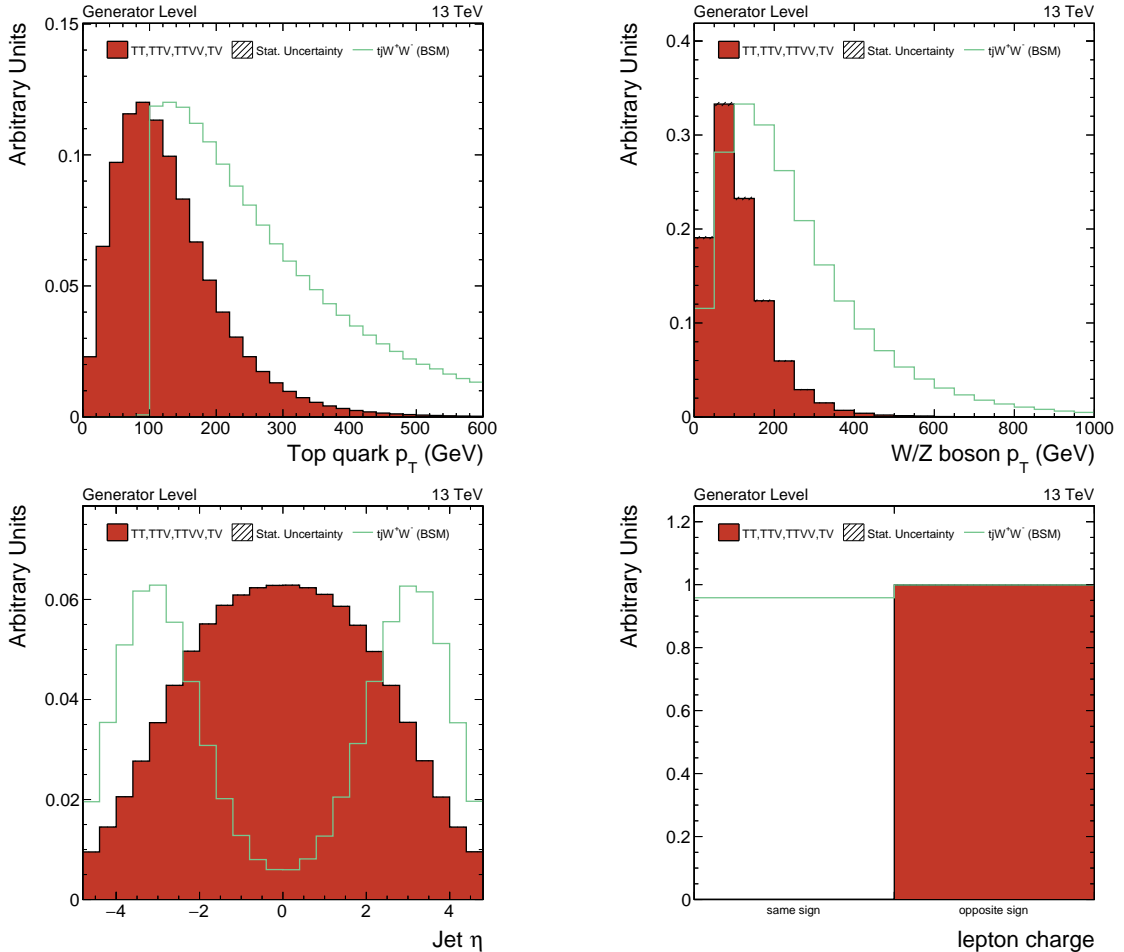

Figure 5.6: Top quark (top left) and W/Z boson transverse momentum (top right), jet pseudorapidity (bottom left), and lepton charges (bottom right) at generator level in $pp \to t\bar{t}$+jets, $t\bar{t}V$, $t\bar{t}VV$, and tV events, with the BSM contribution to the signal superimposed.

34

5.2.2 Vector bosons

Diboson events ($pp \to W^+W^-$, $W^\pm Z$, ZZ) can only contribute to the 1ℓ event category if a W or Z boson is misidentified as a hadronically decaying top quark and a jet fakes a lepton or is misidentified as a W boson. Therefore, the diboson background is mostly relevant in the 2ℓ event category, where no t-tagged AK8 jet is required. As discussed above, requiring both leptons to have the same electric charge greatly reduces the background contribution in the 2ℓ category.

The same is true for $pp \to WWW$, WWZ, WZZ, and ZZZ events. The $pp \to VVV$ cross sections are two orders of magnitude smaller than $pp \to VV$. Figure 5.7 shows the W and Z boson p_T and the jet pseudorapidity at generator level in $pp \to VV$ and $pp \to VVV$ events.
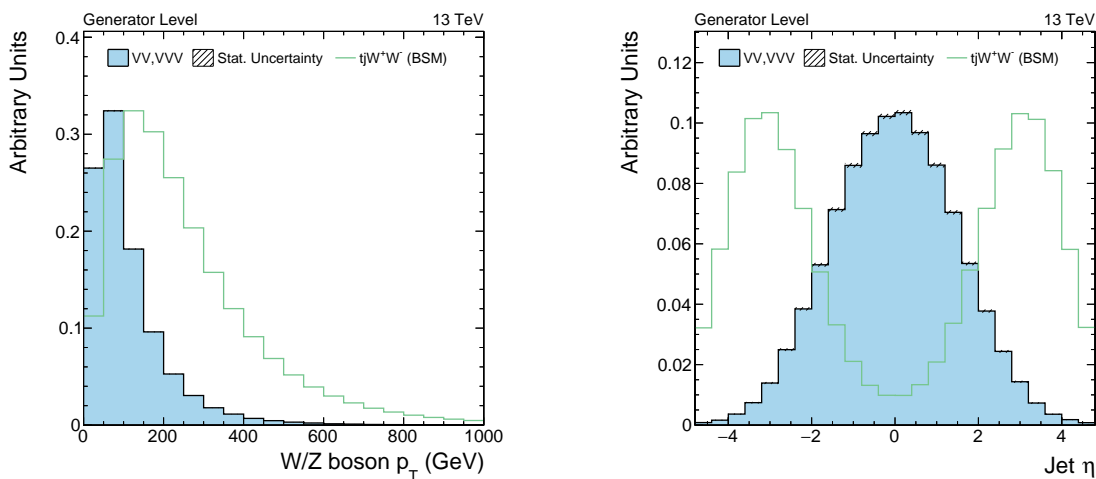

Figure 5.7: W/Z boson transverse momentum (left) and jet pseudorapidity (right) at generator level in $pp \to VV$ and $pp \to VVV$ events, with the BSM contribution to the signal superimposed.

5.2.3 QCD multijet production

The kinematic distributions of jets in QCD multijet events are shown in figure 5.8. QCD multijet events with highly energetic jets can contribute to the background, however, this requires two AK8 jets to be misidentified as a hadronic top quark and W boson, with an additional fake lepton; or one AK8 jet misidentified as a hadronically decaying W boson and two fake leptons. With the low misidentification rate of the DeepAK8 t- and W-classifiers and additional requirements on the presence of leptons and forward jets, the QCD multijet background is expected to be small.
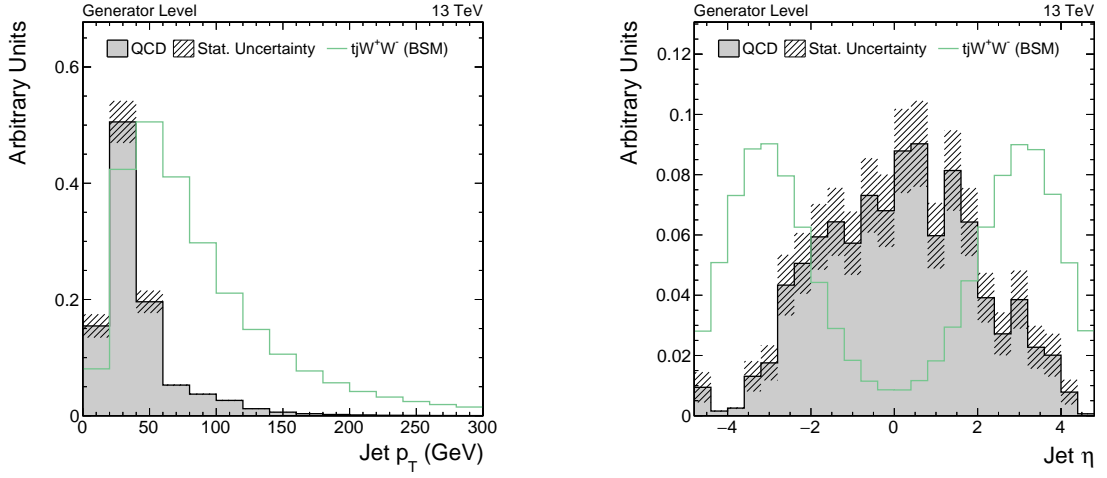
Figure 5.8: Jet transverse momentum (left) and pseudorapidity (right) at generator level in QCD multijet events, with the BSM contribution to the signal superimposed.

Table 5.2: Background MC samples with cross section times branching fraction given in pb.

Sample name	$\sigma \times \mathcal{B}$ (pb)
QCD_HT50to100_TuneCP5_PSWeights_13TeV-madgraphMLM-pythia8	185.4×10^6
QCD_HT100to200_TuneCP5_PSWeights_13TeV-madgraphMLM-pythia8	2366×10^3
QCD_HT200to300_TuneCP5_PSWeights_13TeV-madgraphMLM-pythia8	1551×10^3
QCD_HT300to500_TuneCP5_PSWeights_13TeV-madgraphMLM-pythia8	323×10^3
QCD_HT500to700_TuneCP5_PSWeights_13TeV-madgraphMLM-pythia8	29.96×10^3
QCD_HT700to1000_TuneCP5_PSWeights_13TeV-madgraphMLM-pythia8	6.353×10^3
QCD_HT1000to1500_TuneCP5_PSWeights_13TeV-madgraphMLM-pythia8	1.093×10^3
QCD_HT1500to2000_TuneCP5_PSWeights_13TeV-madgraphMLM-pythia8	99.35
QCD_HT2000toInf_TuneCP5_PSWeights_13TeV-madgraphMLM-pythia8	20.25
TTToSemiLeptonic_TuneCP5_13TeV-powheg-pythia8	365.34
TTToHadronic_TuneCP5_13TeV-powheg-pythia8	377.96
TTTo2L2Nu_TuneCP5_13TeV-powheg-pythia8	88.29
TTWJetsToLNu_TuneCP5_13TeV-amcatnloFXFX-madspin-pythia8	0.17693
TTWJetsToQQ_TuneCP5_13TeV-amcatnloFXFX-madspin-pythia8	0.382
TTZToLLNuNu_M-10_TuneCP5_13TeV-amcatnlo-pythia8	0.28817
TTZToQQ_TuneCP5_13TeV-amcatnlo-pythia8	0.64745
TTWW_TuneCP5_13TeV-madgraph-pythia8	0.0115
TTWZ_TuneCP5_13TeV-madgraph-pythia8	0.0038229
TTZZ_TuneCP5_13TeV-madgraph-pythia8	0.00198
ST_tW_top_5f_inclusiveDecays_TuneCP5_13TeV-powheg-pythia8	35.85
ST_tW_antitop_5f_inclusiveDecays_TuneCP5_13TeV-powheg-pythia8	35.85
tZq_ll_4f_ckm_NLO_TuneCP5_13TeV-amcatnlo-pythia8	0.07358
WW_TuneCP5_13TeV-pythia8	118.7
WZ_TuneCP5_13TeV-pythia8	45.6
ZZ_TuneCP5_13TeV-pythia8	16.9
WWW_4F_TuneCP5_13TeV-amcatnlo-pythia8	0.2086
WWZ_4F_TuneCP5_13TeV-amcatnlo-pythia8	0.1651
WZZ_TuneCP5_13TeV-amcatnlo-pythia8	0.05565
ZZZ_TuneCP5_13TeV-amcatnlo-pythia8	0.01398

6 Event Selection

Events are selected using either the `HLT_IsoMu24` or `HLT_Ele35_WPTight_Gsf` triggers, which require the presence of at least one muon with $p_T > 24$ GeV or electron with $p_T > 35$ GeV respectively.

6.1 Object selection

Leptons are required to have $|\eta| < 2.4$ and be isolated from other particles, $I_{\text{rel}} < 0.15$. The relative isolation of a muon (electron) is calculated in a cone of $\Delta R = 0.4$ (0.3) around the lepton. Muons are selected if they have $p_T > 24$ GeV and pass the medium muon ID criteria, a set of constraints on inner tracker hits, muon segment compatibility, and track fit quality that target a 99.5% identification efficiency for muons from simulated W and Z boson decays [36]. Electrons are selected if they have $p_T > 35$ GeV and pass the WP90 electron ID, a threshold on the multivariate classifier that targets a 90% electron identification efficiency [37].

AK8 jets are required to have $|\eta| < 2.4$ and $p_T > 200$ GeV and pass the tight jet identification criteria. The angular distance between the AK8 jet and any isolated lepton in the event must be $\Delta R_{J,\ell} > 0.8$. To be considered a hadronic top quark, the AK8 jet must have a DeepAK8 t-discriminant above the medium working point 0.802 (1% misstagging rate, above 25% signal efficiency for top quarks with $p_T \in (300, 500)$ GeV, 55% with $p_T \in (1000, 1500)$ GeV); to be considered a hadronic W boson, a DeepAK8 W-discriminant above the tight working point 0.961 (0.5% misstagging rate, above 45% signal efficiency for W bosons with $p_T \in (300, 500)$ GeV, 65% with $p_T \in (1000, 1500)$ GeV [39]) and t-discriminant below the loose working point 0.436.

AK4 jets must have $|\eta| < 4.7$ and $p_T > 15$ GeV and pass the tight jet identification criteria. The angular distance between the jet and any isolated lepton in the event must be $\Delta R_{j,\ell} > 0.4$, between the jet and the hadronic top quark $\Delta R_{j,t} > 0.8$, and between the jet and the hadronic W boson $\Delta R_{j,W} > 0.8$. A jet is considered a b-tagged jet if it has a DeepCSV b-classifier above the medium working point 0.277. Jets with $|\eta| > 2.4$ are referred to as forward jets in the following.

6.2 Event categories

Three event categories, 1μ, $1e$, and 2ℓss, are defined based on top quark decay mode and lepton flavour. Events are required to pass the preselection criteria of one of the three event categories, which are described in this section and summarized in table 6.1.

Table 6.1: Event categories. t, b, and ν always refers to $\bar{t}$, $\bar{b}$, and $\bar{\nu}$ as well, ℓ refers to either μ or e, j refers to a jet originating from any quark or antiquark, except t and $\bar{t}$.

Name	Preselection criteria	Selected signal
1μ	`HLT_IsoMu24`, one muon, one hadronic top quark, one hadronic W boson, at least one additional jet.	$t(\to bjj)\, j\, W^\pm(\to \mu^\pm\nu)$ $W^\mp(\to jj)$
$1e$	`HLT_Ele35_WPTight_Gsf`, one electron, one hadronic top quark, one hadronic W boson, at least one additional jet.	$t(\to bjj)\, j\, W^\pm(\to e^\pm\nu)$ $W^\mp(\to jj)$
$2\ell\mathrm{ss}$	`HLT_IsoMu24` or `HLT_Ele35_WPTight_Gsf`, two same-sign leptons, one hadronic W boson, at least one additional jet.	$t(\to b\ell^\pm\nu)\, j\, W^\pm(\to \ell^\pm\nu)$ $W^\mp(\to jj)$

The single lepton event categories, 1μ and $1e$, are designed to preselect events with hadronically decaying top quarks. Events are required to have exactly one muon or electron, one hadronic top quark, one hadronic W boson, and at least one additional jet that pass the object selection criteria. Events with additional leptons that pass looser selection criteria, $p_\mathrm{T} > 15$ GeV, $|\eta| < 2.4$, $I_\mathrm{rel} < 0.15$, medium muon ID or WP90 electron ID, are rejected.

The dilepton event category, $2\ell\mathrm{ss}$, is designed to preselect events with leptonically decaying top quarks. Events are required to have exactly two same-sign (same electric charge) leptons ($\mu^\pm\mu^\pm$, $e^\pm e^\pm$, $\mu^\pm e^\pm$), one hadronic W boson, and at least one additional jet that pass the object selection criteria. Requiring the same electric charge for the two leptons retains only half the signal in the leptonic top quark decay channel, however, as discussed in section 5.2, it greatly reduces the background from leptonic Z boson decays and from $t\bar{t}$, $tW^\pm$, and W^+W^- events with two leptonic decays. Events in this category are rejected if they have an AK8 jet with a DeepAK8 t-discriminant above the loose working point 0.436, or additional leptons that pass the looser selection criteria listed above.

Table 6.2: Expected number of background and SM signal events in 3000 fb^{-1} of data in the three event categories.

Process	1μ	$1e$	$2\ell\mathrm{ss}$
$t\bar{t}$	10431 ± 156	6948 ± 127	5332 ± 111
$t\bar{t}V$	1261 ± 44	873 ± 37	713 ± 13
$t\bar{t}VV$	91.0 ± 1.7	70.9 ± 1.5	62.1 ± 1.4
tV	2498 ± 186	1570 ± 148	615 ± 92
VVV	53.9 ± 1.8	39.5 ± 1.6	325 ± 5
VV	17 ± 17	108 ± 49	182 ± 58
QCD	0	401 ± 401	0
Total background	14352 ± 247	10010 ± 450	7229 ± 156
SM signal [1]	222 ± 4	163 ± 4	306 ± 5

[1] $c_\mathrm{uH} = 0$.

The expected number of events of the various backgrounds and the SM signal in the three event categories, in 3000 fb^{-1} of data, are listed in table 6.2.

6.3 Event selection

One of the main features of the signal signature is the forward jet. Some forward jets are also present in most background events, but in the signal process the forward jet is often the most energetic jet in the event. One way to make use of this, is to require the highest p_T jet of the event (leading jet) to pass the forward jet requirement, $|\eta| > 2.4$. Another option is to apply a slightly higher p_T cut on forward jets. Figure 6.1 shows the leading jet $|\eta|$ and forward jet p_T of the relevant backgrounds, with the BSM contribution to the signal superimposed.
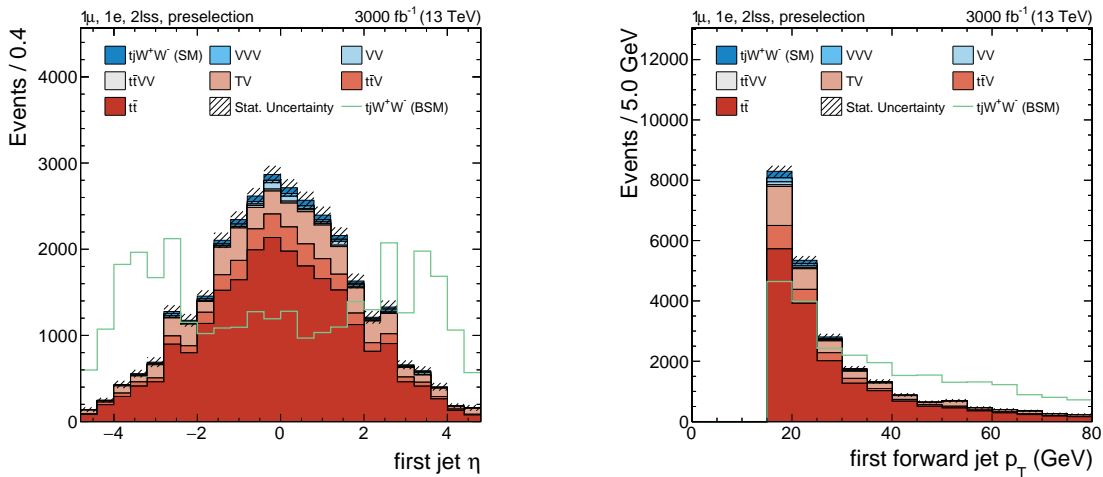
Figure 6.1: Leading jet pseudorapidity (left) and forward jet transverse momentum (right) in background events with the BSM contribution to the signal superimposed.

Another observable that is interesting to study, in the 1μ and $1e$ event categories in particular, is the transverse momentum of the lepton+missing energy system, $|\mathbf{p}_\mathrm{T}^\ell + \mathbf{E}_\mathrm{T}^\mathrm{miss}|$. If the lepton is the decay product of a W boson, it is produced in association with a neutrino and $|\mathbf{p}_\mathrm{T}^\ell + \mathbf{E}_\mathrm{T}^\mathrm{miss}|$ corresponds to the transverse momentum of the decayed W boson. The lepton+missing energy p_T helps to identify leptons that are not from W boson decays, in which case the lepton and missing energy do not originate from the same source and $|\mathbf{p}_\mathrm{T}^\ell + \mathbf{E}_\mathrm{T}^\mathrm{miss}|$ is expected to be small.

The $|\mathbf{p}_\mathrm{T}^\ell + \mathbf{E}_\mathrm{T}^\mathrm{miss}|$ and transverse momentum distributions of the leptons and the t- and W-tagged AK8 jets of the backgrounds, with the BSM contribution to the signal superimposed, are shown in figure 6.2.

After applying a cut on the pseudorapidity of the leading jet, $|\eta^{j1}| > 2.4$, only 76 simulated $pp \to tW$ events remain in the combined 1μ and $1e$ event categories, and ten in the 2ℓss category. This corresponds to an expected $pp \to tW$ yield in the full HL-LHC data of 1054 ± 121 ($1\mu + 1e$) and 139 ± 44 (2ℓss). With a tighter event selection, only a handful of simulated events remain, leading to large uncertainties. This is illustrated
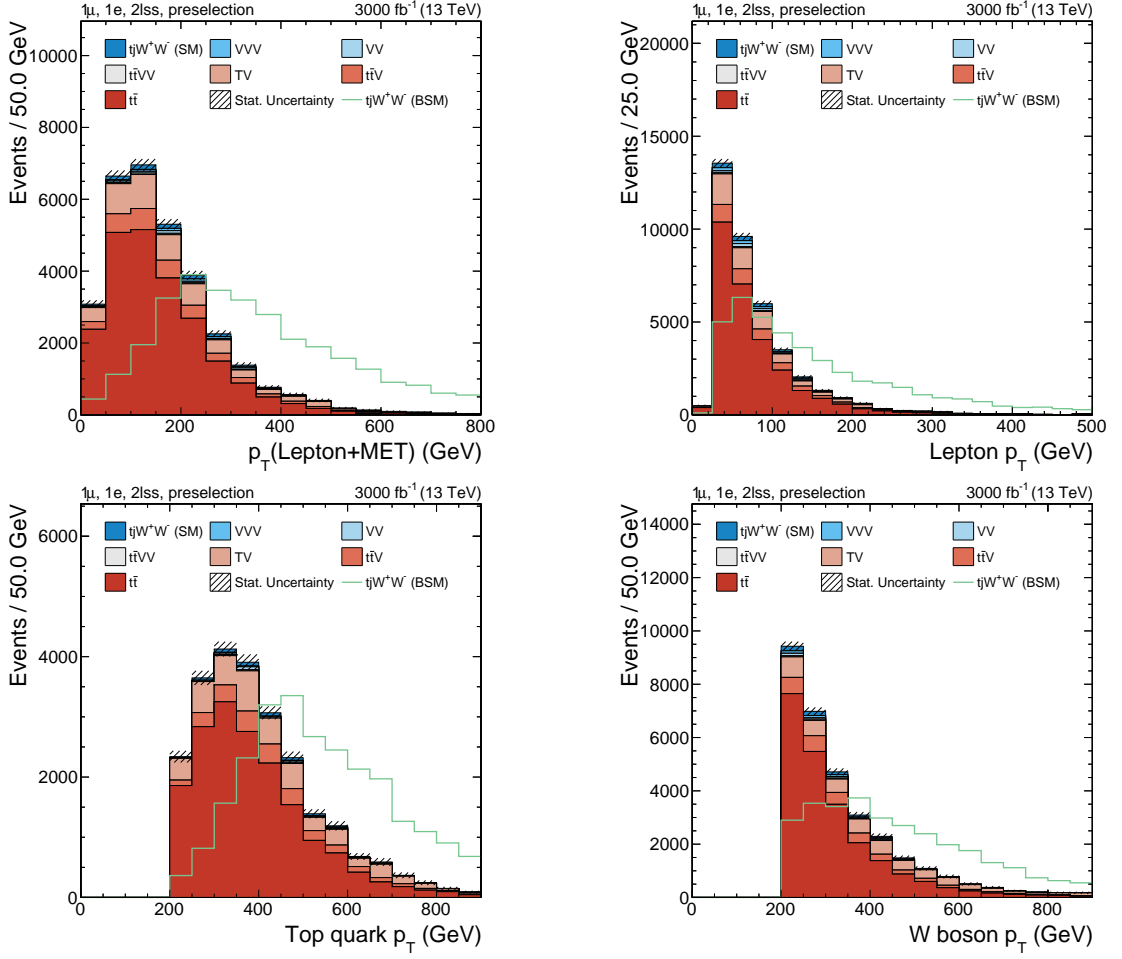
Figure 6.2: Transverse momentum of the lepton+missing transverse energy system (top left), lepton (top right), hadronic top quark (bottom left), and W boson (bottom right) in background events with the BSM contribution to the signal superimposed.

in figure 6.3, where an additional cut is applied on the transverse momentum of the hadronic top quark, $p_T^t > 350$ GeV. The small number of MC events leads to large fluctuations from bin to bin in the p_T^W and $|\mathbf{p}_T^\ell + \mathbf{E}_T^{\mathrm{miss}}|$ distributions, making an accurate estimation of the tW background impossible. The tZ background can safely assumed to be negligible, as its cross section is two orders of magnitude smaller than $pp \to tW$.

The same issue exists in the $pp \to VV$ case. In the $1\mu + 1e$ (2ℓss) event categories, only six (eleven) simulated events pass the preselection, corresponding to an expected 125 ± 52 (182 ± 58) events in the HL-LHC data. Requiring the leading jet to pass the forward jet requirement reduces this number to two and one simulated event respectively.

Based on these considerations, the tW, tZ, WW, WZ, ZZ, and QCD multijet backgrounds (where only one simulated event passes the preselection in the $1e$ category, and none in the other two) are not considered in the following.

Two different approaches are used to distinguish signal from background in each event category: Cut-and-count (section 6.3.1) and multivariate analysis (section 6.3.2).
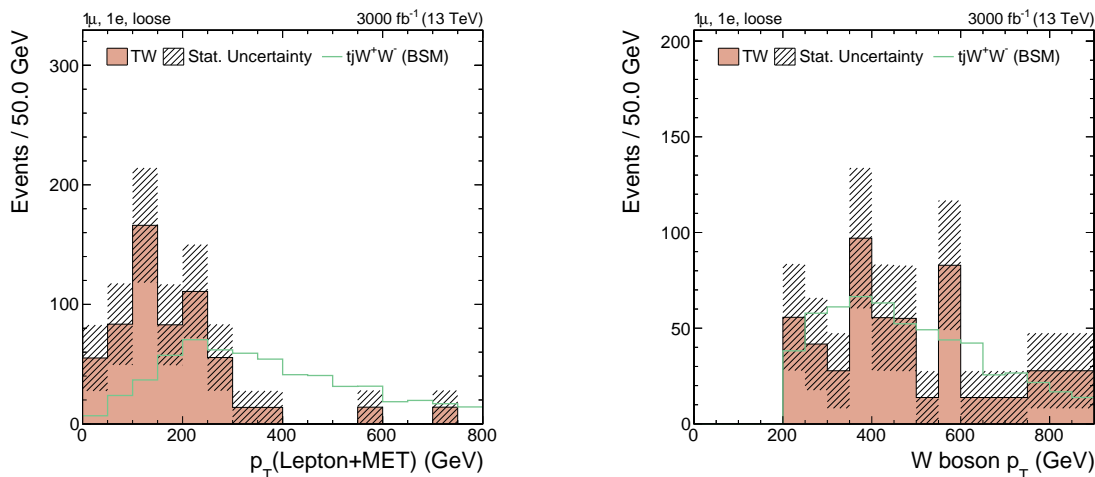
Figure 6.3: Transverse momentum of the lepton+missing transverse energy system (left) and the hadronic W boson (right) in $pp \to tW$ events with a slightly tighter event selection.

6.3.1 Cut-and-count analysis

In a cut-and-count analysis, a series of constraints is applied to parameters that have a strong separating power between signal and background. Then, the number of events that pass these constraints is counted and compared to the expected number of background events, in order to extract the signal.

Cuts need to be chosen carefully, in such a way that most events from background processes are rejected, while as many signal events as possible are accepted. A useful measure for cut optimization is the Asimov Median Significance (AMS) [47]

$$
\begin{aligned}
Z_A &= \sqrt{2\left[(s+b)\log\left(\frac{(s+b)(b+\sigma_b^2)}{b^2+(s+b)\sigma_b^2}\right) - \frac{b^2}{\sigma_b^2}\log\left(1+\frac{\sigma_b^2 s}{b(b+\sigma_b^2)}\right)\right]} \\
&= \frac{s}{\sqrt{b+\sigma_b^2}}\left(1+\mathcal{O}(s/b)+\mathcal{O}(\sigma_b^2/b)\right),
\end{aligned}
\tag{6.1}
$$

an approximate expression for the expected discovery significance of a Poisson counting experiment. Here, s and b are the expected number of signal and background events and σ_b is the uncertainty on b. For the purpose of cut optimization, the SM contribution to the tjW^+W^- final state is considered to be part of the background, and only the BSM contribution is considered as signal. The expected signal yield depends on the value of c_{uH}, however, when comparing the signal sensitivity of different sets of cuts, it is enough to evaluate the AMS for some arbitrary non-zero value of the Wilson coefficient, chosen here to be $c_{\text{uH}} = 40$.

In the 1μ and $1e$ categories, cuts are applied on the pseudorapidity of the highest-p_T jet of the event, $|\eta^{j_1}|$; the transverse momenta of the hadronic top quark and W boson, p_T^t, p_T^W; and on the p_T of the lepton+missing transverse energy system, $|\mathbf{p}_T^\ell + \mathbf{E}_T^{\text{miss}}|$. The

signal and background distributions of these observables in both the 1μ and $1e$ categories are shown in figures 6.4 and 6.5. The following cuts are applied:

$$|\eta^{j_1}| > 2.4, \quad p_T^t > 350\,\text{GeV}, \quad p_T^W > 300\,\text{GeV}, \quad |\mathbf{p}_T^\ell + \mathbf{E}_T^{\text{miss}}| > 350\,\text{GeV}. \qquad (6.2)$$
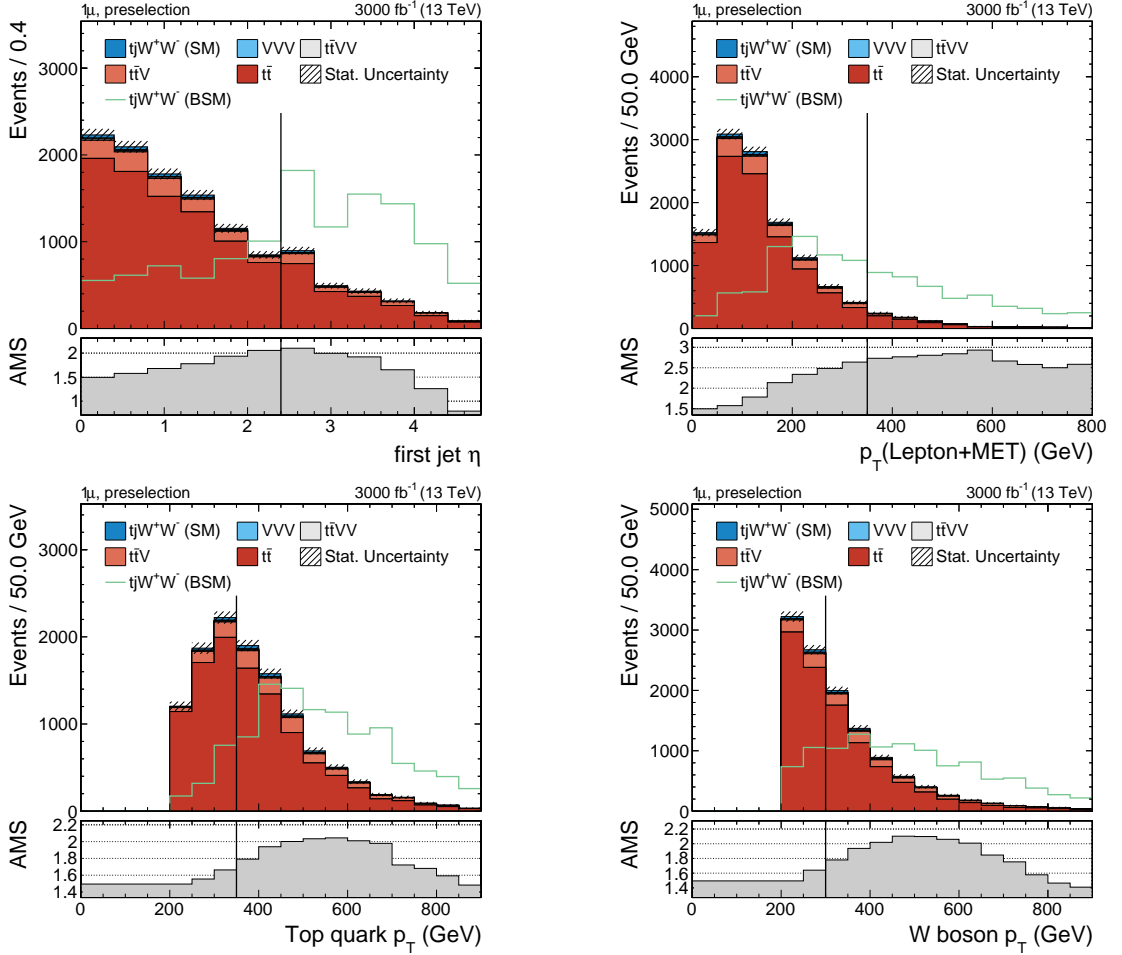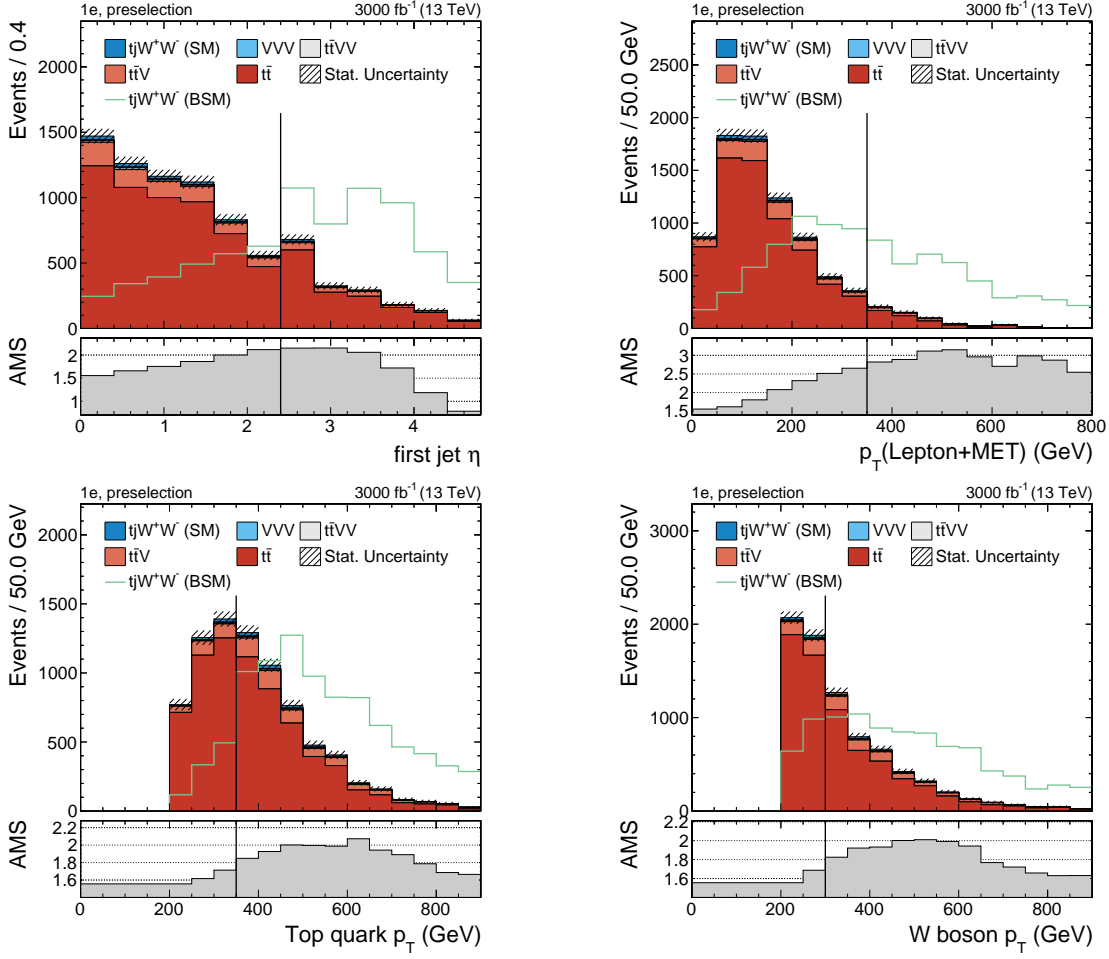

Figure 6.4: Signal and background distributions of $|\eta^{j_1}|$, $|\mathbf{p}_T^\ell + \mathbf{E}_T^{\text{miss}}|$, p_T^t, p_T^W (left to right and top to bottom) in the 1μ category. Bottom panel shows the Asimov Median Significance, assuming $c_{\text{uH}} = 40$, for a cut in the respective bin. The vertical line indicates the position of the cuts that are applied to these observables.

Figure 6.5: Signal and background distributions of $|\eta^{j_1}|$, $|\mathbf{p}_T^\ell + \mathbf{E}_T^{miss}|$, p_T^t, p_T^W (left to right and top to bottom) in the $1e$ category. Bottom panel shows the Asimov Median Significance, assuming $c_{uH} = 40$, for a cut in the respective bin. The vertical line indicates the position of the cuts that are applied to these observables.

In the 2ℓss category, cuts are applied on the number of forward jets (jets with $|\eta| > 2.4$), N_f; the transverse momenta of the leading forward jet, the hadronic W boson, and the two leptons, $p_T^{f_1}$, p_T^W, $p_T^{\ell_1}$, $p_T^{\ell_2}$; the missing transverse energy, E_T^{miss}; the angular distance of the two leptons, $\Delta R_{\ell_1,\ell_2}$; and on their relative isolation, $I_{rel}^{\ell_1}$, $I_{rel}^{\ell_2}$. Figures 6.6 and 6.7 show the signal and background distributions of these observables in the 2ℓss category. The chosen cuts are

$$
\begin{aligned}
N_f \geq 1, \quad & p_T^{f_1} > 30\,\text{GeV}, \quad p_T^W > 300\,\text{GeV}, \quad p_T^{\ell_1} > 100\,\text{GeV}, \quad p_T^{\ell_2} > 50\,\text{GeV}, \\
& E_T^{miss} > 50\,\text{GeV}, \quad \Delta R_{\ell_1,\ell_2} > 0.8, \quad I_{rel}^{\ell_1} < 0.075, \quad I_{rel}^{\ell_2} < 0.075\,.
\end{aligned}
\tag{6.3}
$$

Table 6.3 shows the expected background yields and the expected signal yields for two values of the Wilson coefficient, $c_{uH} = 0, 40$, in each of the three event categories, scaled to an integrated luminosity of 3000 fb^{-1}.
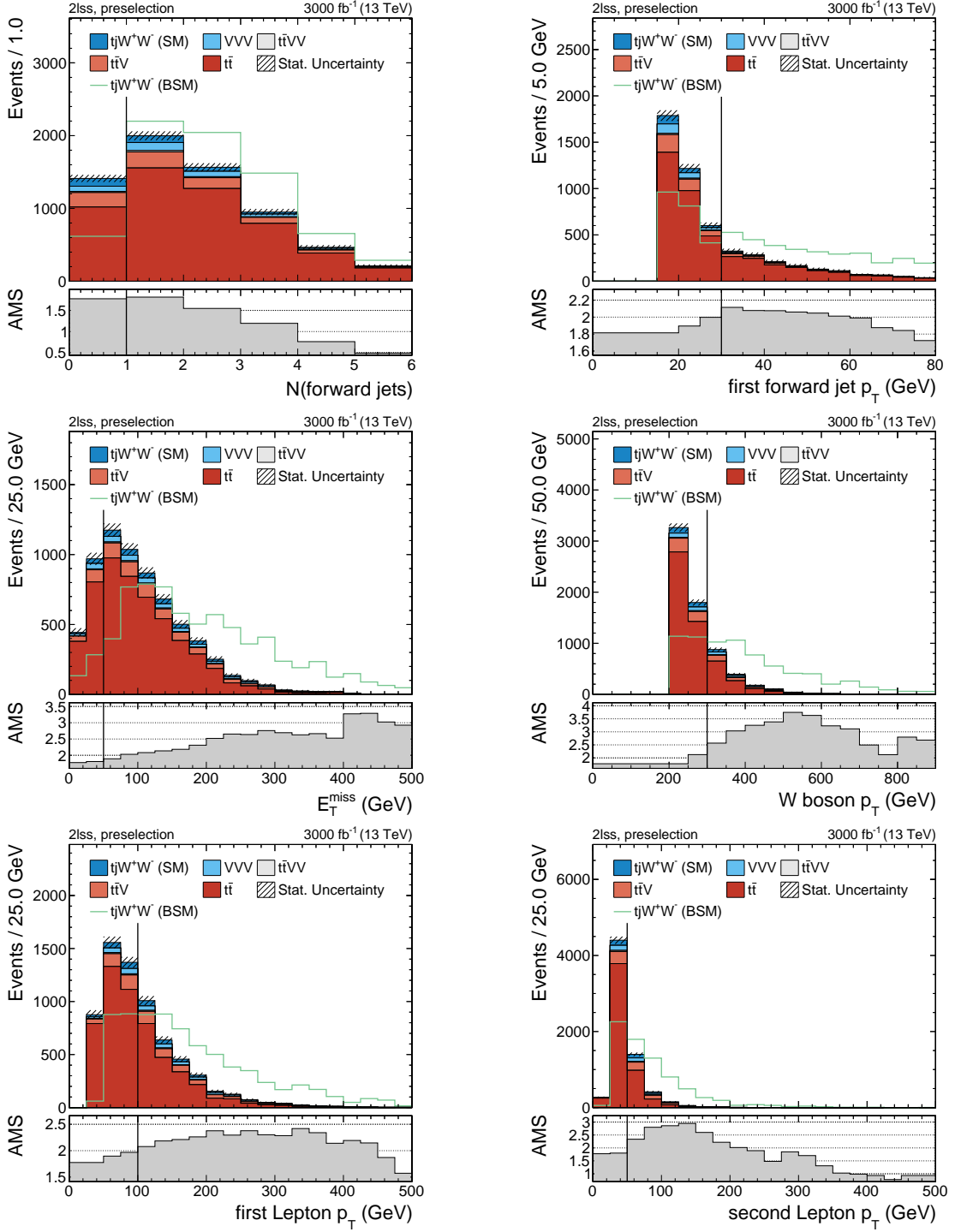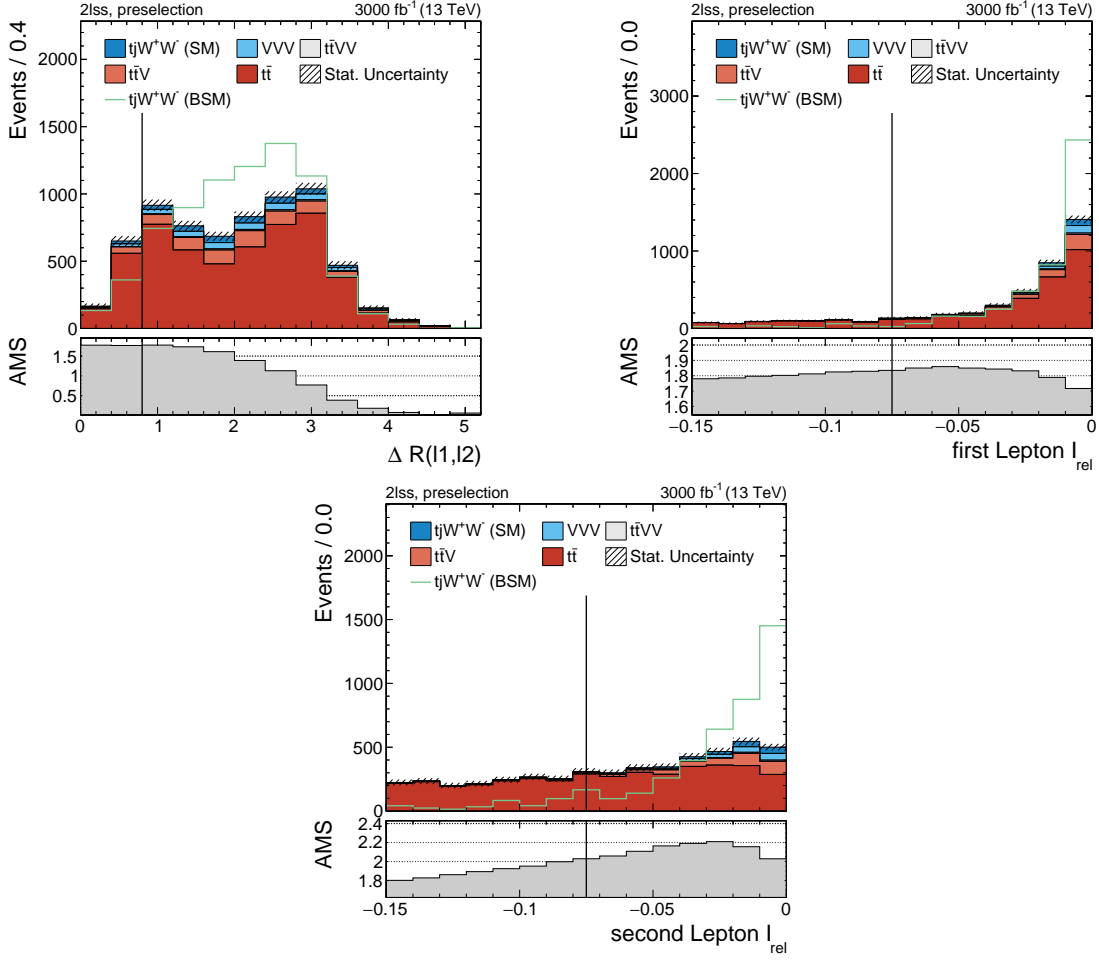
Figure 6.6: Signal and background distributions of N_f, $p_T^{f_1}$, E_T^{miss}, p_T^W, $p_T^{\ell_1}$, $p_T^{\ell_2}$ (left to right and top to bottom) in the 2ℓss category. Bottom panel shows the Asimov Median Significance, assuming $c_{uH} = 40$, for a cut in the respective bin. The vertical line indicates the position of the cuts that are applied to these observables.

Figure 6.7: Signal and background distributions of $\Delta R_{\ell_1,\ell_2}$, $I_{\text{rel}}^{\ell_1}$, $I_{\text{rel}}^{\ell_2}$ (left to right and top to bottom) in the 2ℓss category. Bottom panel shows the Asimov Median Significance, assuming $c_{\text{uH}} = 40$, for a cut in the respective bin. The vertical line indicates the position of the cuts that are applied to these observables.

Table 6.3: Expected background and signal yields from cut-and-count analysis.

Process	1μ	$1e$	2ℓss
$t\bar{t}$	20.4 ± 6.8	17.7 ± 7.0	11.4 ± 5.1
$t\bar{t}V$	12.3 ± 4.6	12.5 ± 4.1	14.1 ± 1.6
$t\bar{t}VV$	1.7 ± 0.2	1.0 ± 0.2	2.7 ± 0.3
VVV	1.3 ± 0.3	1.3 ± 0.3	12.9 ± 1.0
Total background	35.8 ± 8.3	32.5 ± 8.1	41.0 ± 5.4
SM signal [1]	4.6 ± 0.6	3.0 ± 0.5	5.8 ± 0.7
BSM signal [2]	67.7 ± 2.6	63.8 ± 2.5	61.3 ± 2.6

[1] $c_{\text{uH}} = 0$.

[2] The BSM signal yield depends quadratically on the Wilson coefficient. The yield reported here is for $c_{\text{uH}} = 40$, which is chosen arbitrarily. The SM contribution is subtracted.

6.3.2 Multivariate analysis

In a multivariate analysis (MVA), many observables that have a small separating power between signal and background are combined to obtain a more powerful discriminating variable. A boosted decision tree (BDT) classifier with gradient boosting (*XGBoost* [48]) is used as the MVA discriminant. Simulated signal and background events that pass the preselection criteria in one of the three event categories are split into training and control sets and in each event category a BDT model is trained. The training sets contain 20% of the simulated events.

The XGBoost library provides a built-in tool to evaluate the separating power (or feature importance) of each observable used as input to the BDT. This simply refers to the number of times a given observable is used in all the trees. The BDT training is done in several iterations, each time removing the least used variables.

The BDT classifiers in the 1μ and $1e$ event categories each use 16 input variables, which are listed in table 6.4. The feature importance of these observables is shown in figure 6.8. The observables that are found to provide the best discrimination between signal and background include those used in the cut-and-count analysis — the pseudorapidity of the leading jet, $|\eta_{j_1}|$, the transverse momentum of the hadronic top quark and the hadronic W boson, p_T^t, p_T^W, and the reconstructed transverse momentum of the leptonic W boson, $|\mathbf{p}_T^\ell + \mathbf{E}_T^{\mathrm{miss}}|$ — but also new observables like the DeepAK8 W-classifier of the hadronic W boson, the transverse momentum of the lepton, p_T^ℓ, and the angular distances between the lepton and the hadronic W boson, $\Delta R_{\ell,W}$, the lepton and the leading jet, $\Delta R_{\ell,j_1}$, and between the lepton and the leading b-tagged jet, $\Delta R_{\ell,b_1}$. Two of these observables, the W-classifier and $\Delta R_{\ell,j_1}$, are shown in figure 6.9.
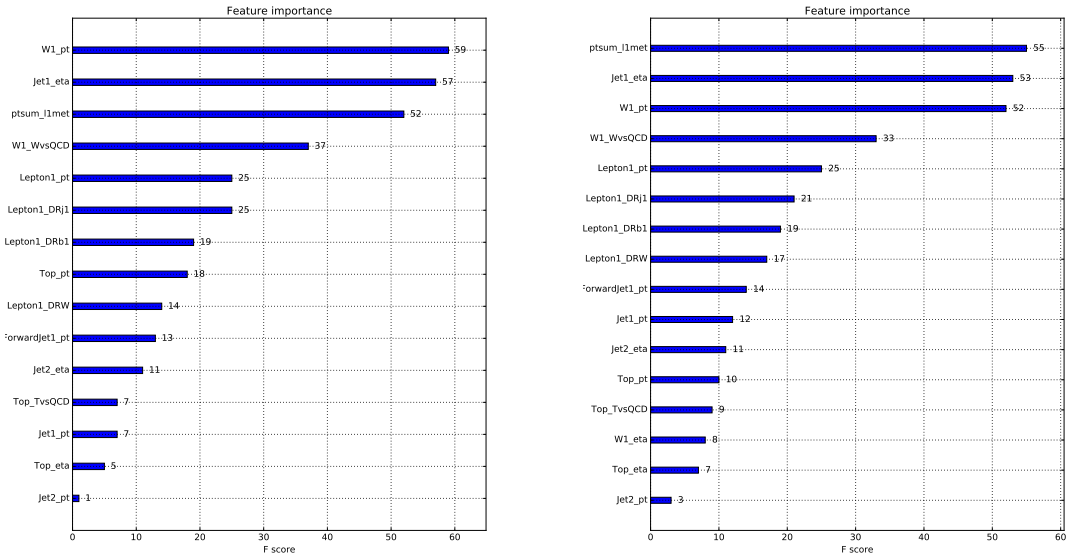

Figure 6.8: Feature importance for the BDT classifier in the 1μ (left) and $1e$ (right) event categories.

Table 6.4: Input variables for the BDT classifier in the 1μ and $1e$ event categories.

| Name	Description
Top_pt	p_{T}^t, transverse momentum of the top quark
Top_eta	$|\eta_t|$, pseudorapidity of the top quark
Top_TvsQCD	DeepAK8 t-classifier of the top quark
W1_pt	p_{T}^W, transverse momentum of the W boson
W1_eta	$|\eta_W|$, pseudorapidity of the W boson
W1_WvsQCD	DeepAK8 W-classifier of the W boson
Jet1_pt	$p_{\mathrm{T}}^{j_1}$, transverse momentum of the leading jet
Jet1_eta	$|\eta_{j_1}|$, pseudorapidity of the leading jet
Jet2_pt	$p_{\mathrm{T}}^{j_2}$, transverse momentum of the subleading jet
Jet2_eta	$|\eta_{j_2}|$, pseudorapidity of the subleading jet
ForwardJet1_pt	$p_{\mathrm{T}}^{f_1}$, transverse momentum of the leading forward jet
Lepton1_pt	p_{T}^ℓ, transverse momentum of the lepton
Lepton1_DRb1	$\Delta R_{\ell,b_1}$, angular distance between lepton and leading b-tagged jet
Lepton1_DRj1	$\Delta R_{\ell,j_1}$, angular distance between lepton and leading jet
Lepton1_DRW	$\Delta R_{\ell,W}$, angular distance between lepton and W boson
ptsum_l1met	$|\mathbf{p}_{\mathrm{T}}^\ell + \mathbf{E}_{\mathrm{T}}^{\mathrm{miss}}|$, transverse momentum of the lepton+missing energy system
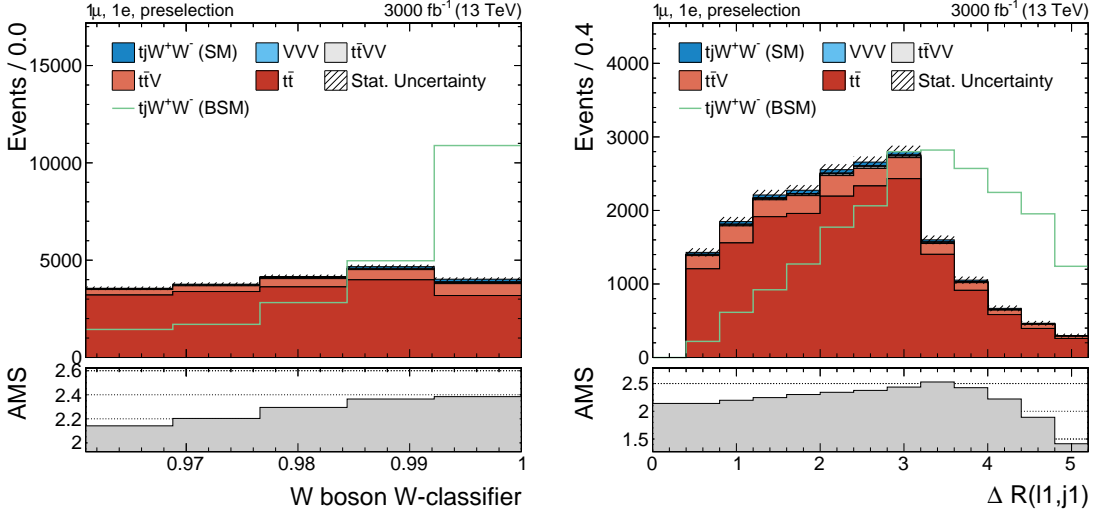
Figure 6.9: Signal and background distributions of the W-classifier of the hadronic W boson (left) and the angular distance between the lepton and the leading jet (right) in the 1μ and $1e$ event categories. Bottom panel shows the Asimov Median Significance, assuming $c_{\mathrm{uH}} = 40$, for a cut in the respective bin.
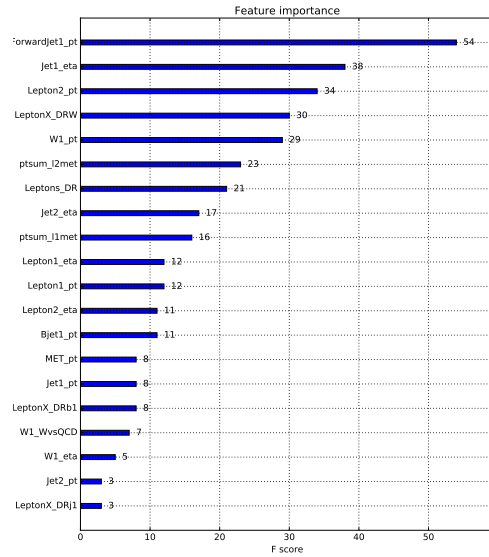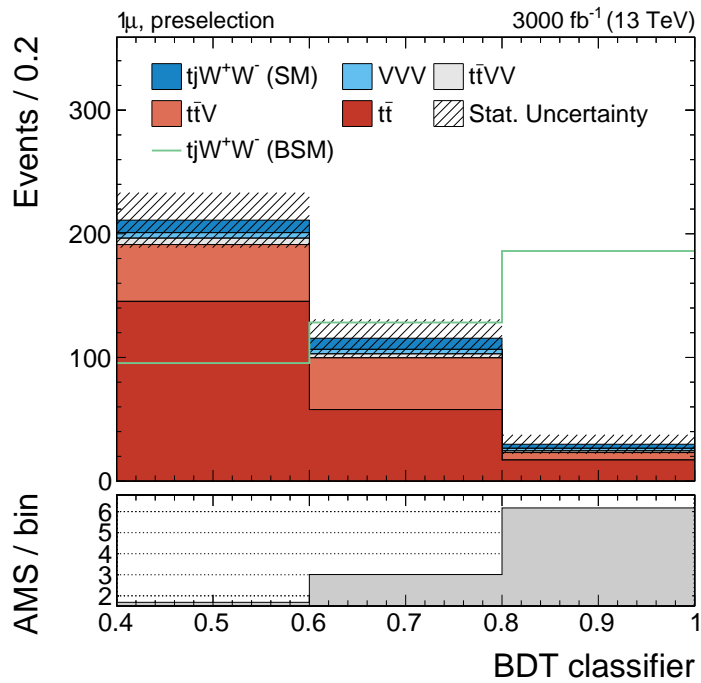
In the 2ℓss category, the BDT classifier uses 20 input variables, listed in table 6.5. Figure 6.10 shows the feature importance of these observables. Interestingly, the relative isolation of the leptons, $I_{\mathrm{rel}}^{\ell_1}$, $I_{\mathrm{rel}}^{\ell_2}$, which are used in the cut-based event selection in the 2ℓss category, are found to provide very little separating power and are therefore not used as inputs to the BDT classifier. This could indicate that $I_{\mathrm{rel}}^{\ell_1}$ and $I_{\mathrm{rel}}^{\ell_2}$ are strongly

correlated with other observables with more separating power, for example $|\mathbf{p}_T^{\ell_1} + \mathbf{E}_T^{\mathrm{miss}}|$ and $|\mathbf{p}_T^{\ell_2} + \mathbf{E}_T^{\mathrm{miss}}|$, but this has not been investigated further.

Table 6.5: Input variables for the BDT classifier in the 2ℓss event category.

Name	Description
W1_pt	p_T^W, transverse momentum of the W boson
W1_eta	$|\eta_W|$, pseudorapidity of the W boson
W1_WvsQCD	DeepAK8 W-classifier of the W boson
Jet1_pt	$p_T^{j_1}$, transverse momentum of the leading jet
Jet1_eta	$|\eta_{j_1}|$, pseudorapidity of the leading jet
Jet2_pt	$p_T^{j_2}$, transverse momentum of the subleading jet
Jet2_eta	$|\eta_{j_2}|$, pseudorapidity of the subleading jet
ForwardJet1_pt	$p_T^{f_1}$, transverse momentum of the leading forward jet
Bjet1_pt	$p_T^{b_1}$, transverse momentum of the leading b-tagged jet
Lepton1_pt	$p_T^{\ell_1}$, transverse momentum of the leading lepton
Lepton1_eta	$|\eta_{\ell_1}|$, pseudorapidity of the leading lepton
ptsum_l1met	$|\mathbf{p}_T^{\ell_1} + \mathbf{E}_T^{\mathrm{miss}}|$, transverse momentum of the leading lepton+missing energy system
Lepton2_pt	$p_T^{\ell_2}$, transverse momentum of the subleading lepton
Lepton2_eta	$|\eta_{\ell_2}|$, pseudorapidity of the subleading lepton
ptsum_l2met	$|\mathbf{p}_T^{\ell_2} + \mathbf{E}_T^{\mathrm{miss}}|$, transverse momentum of the subleading lepton+missing energy system
MET_pt	E_T^{miss}, missing transverse energy
Leptons_DR	$\Delta R_{\ell_1,\ell_2}$, angular distance between the leptons
LeptonX_DRb1	$\min(\Delta R_{\ell_1,b_1}, \Delta R_{\ell_2,b_1})$, angular distance between leading b-tagged jet and the closest lepton
LeptonX_DRj1	$\min(\Delta R_{\ell_1,j_1}, \Delta R_{\ell_2,j_1})$, angular distance between leading jet and the closest lepton
LeptonX_DRW	$\min(\Delta R_{\ell_1,W}, \Delta R_{\ell_2,W})$, angular distance between W boson and the closest lepton

The outputs of the BDT classifier B in the 1μ, $1e$, and 2ℓss event categories are displayed in figures 6.11, 6.12, and 6.13. In each category, the expected background and signal yields are evaluated in three bins of B: (0.4, 0.6), (0.6, 0.8), and (0.8, 1.0). The expected background and signal yields in each bin are listed in table 6.6.

Figure 6.10: Feature importance for the BDT classifier in the 2ℓss event category.

Figure 6.11: Output of the BDT classifier in the 1μ event category.
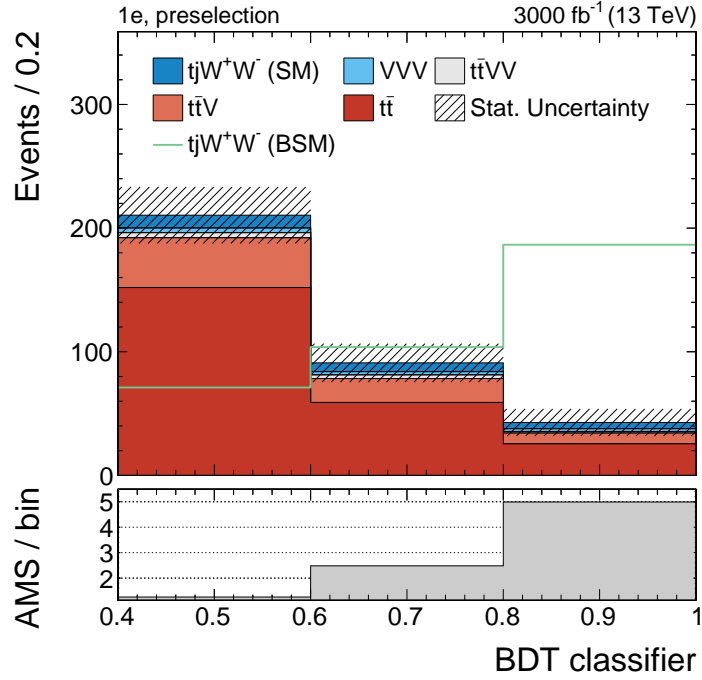
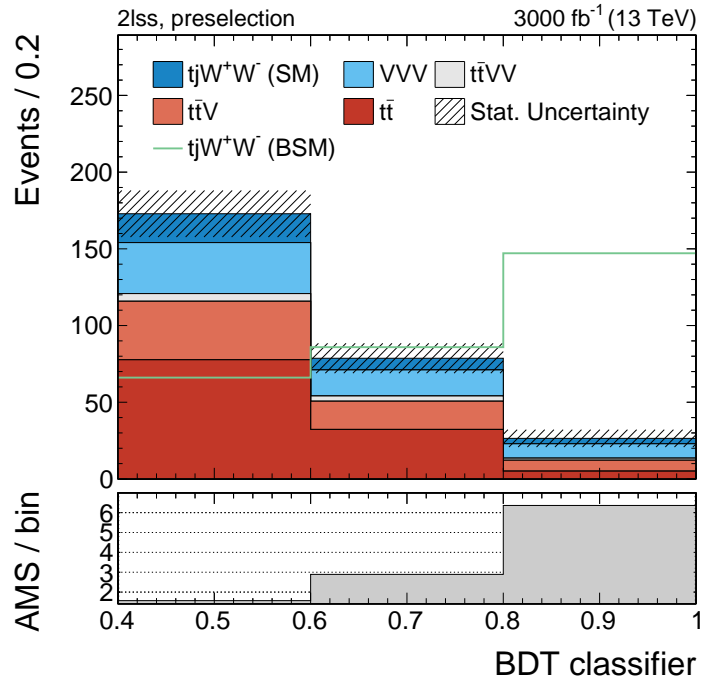Figure 6.12: Output of the BDT classifier in the 1*e* event category.

Figure 6.13: Output of the BDT classifier in the 2ℓss event category.

Table 6.6: Expected background and signal yields from MVA.

	Bin	Background	SM signal [1]	BSM signal [2]
	$0.4 < B < 0.6$	201 ± 22	10.2 ± 1.1	47.7 ± 2.8
1μ	$0.6 < B < 0.8$	107 ± 15	9.0 ± 1.0	64.1 ± 3.1
	$0.8 < B < 1$	26.5 ± 7.7	3.3 ± 0.6	93.0 ± 3.4
	$0.4 < B < 0.6$	200 ± 23	10.4 ± 1.1	35.6 ± 2.5
$1e$	$0.6 < B < 0.8$	83.9 ± 15.5	7.1 ± 0.9	51.9 ± 2.7
	$0.8 < B < 1$	37.7 ± 10.9	5.1 ± 0.8	93.3 ± 3.4
	$0.4 < B < 0.6$	154 ± 15	18.8 ± 1.5	33.0 ± 2.9
2ℓss	$0.6 < B < 0.8$	71.1 ± 9.7	7.6 ± 0.9	43.0 ± 2.6
	$0.8 < B < 1$	22.9 ± 5.6	3.5 ± 0.6	73.6 ± 3.1

[1] $c_{\mathrm{uH}} = 0$

[2] The expected BSM signal yield depends quadratically on the Wilson coefficient. The yield reported here is for $c_{\mathrm{uH}} = 40$, which is chosen arbitrarily. The SM contribution is subtracted.

7 Systematic Uncertainties

7.1 Statistical uncertainties on Monte Carlo samples

Due to the limited number of simulated events in the phase space studied in this analysis, there are large statistical uncertainties on the background predictions. This is by far the biggest source of systematic uncertainty, however, it is an uncertainty that can easily be reduced by obtaining MC samples with more events.

The relative MC statistical uncertainties on the total expected background yields obtained by the cut-and-count analysis are 23%, 25%, and 13% in the 1μ, $1e$, and 2ℓss event categories. In the MVA analysis, the relative uncertainties on the background yields in the $B \in (0.4, 0.6)$, $(0.6, 0.8)$, and $(0.8, 1.0)$ bins are 11%, 14%, 29% in the 1μ category; 12%, 18%, 29% in $1e$; and 9.7%, 14%, 24% in 2ℓss.

As discussed in section 6.3, the $pp \rightarrow tV$ and $pp \rightarrow VV$ samples are too small to allow any meaningful estimate of these backgrounds. Based on the event kinematics, it can be assumed that the applied event selection reduces the tV and VV contributions by at least the same amount as in the $t\bar{t}$ case. In the 1μ, $1e$, and 2ℓss categories, the cut-and-count analysis reduces the $t\bar{t}$ background to $0.20\% \pm 0.07\%$, $0.25\% \pm 0.10\%$, and $0.21\% \pm 0.10\%$ with respect to the preselection. A conservative estimate therefore sets an upper limit on the tV yields at 4.9 ± 1.7 (1μ), 4.0 ± 1.6 $(1e)$, and 1.3 ± 0.6 $(2\ell$ss$)$, which is well within the statistical uncertainty on the $t\bar{t}$ background alone. In the VV case, the upper limits are below one event in each event category.

7.2 Other systematic uncertainties

The $t\bar{t}$ cross section at $\sqrt{s} = 13$ TeV is $\sigma_{t\bar{t}} = 831.8 \, ^{+19.8}_{-29.2}(\text{scale}) \pm 35.1(\text{PDF}+\alpha_s)$ pb as calculated to next-to-next-to-leading order (NNLO) with the *Top++2.0* program [49]. The first uncertainty comes from the independent variation of the factorisation and renormalisation scales, the second one from variations in the parton density functions and the strong coupling α_s. Adding them in quadrature, the relative uncertainty on the $t\bar{t}$ cross section is $+4.8\%$, -5.5%.

For the $t\bar{t}V$, $t\bar{t}VV$, and VVV cross sections, theory uncertainties are not centrally provided within the CMS experiment. The $t\bar{t}V$ and $t\bar{t}VV$ uncertainties are estimated using the $pp \rightarrow tW^-$ cross section, $\sigma_{tW} = 41.8 \, ^{+1.8}_{-2.6}$ pb, which is calculated at NNLO for $\sqrt{s} = 14$ TeV in reference [50]. The VVV uncertainty is estimated from the $pp \rightarrow W^+W^-$ cross section, $\sigma_{WW} = 118.7 \, ^{+2.5\%}_{-2.2\%}$ pb, calculated at NNLO for $\sqrt{s} = 13$ TeV in reference [51]. Following these results, the relative uncertainties on the cross sections are estimated to be $+4.3\%$, -6.2% for $t\bar{t}V$ and $t\bar{t}VV$, and $+2.5\%$, -2.2% for VVV.

The t- and W-tagging uncertainties are taken as the uncertainties on the scale factors. For the medium t-tagging working point with 1% mistagging rate, the uncertainty is assumed to be -4.8%, $+4.3\%$. For the tight W-tagging working point with 0.5% mistagging rate, the uncertainty is -5.3%, $+5.7\%$. For leptons, the uncertainty is 2% per muon and 2% per electron. The uncertainty on the integrated luminosity is estimated to be 2.5%.

7.3 Summary

A summary of the systematic uncertainties on the background and signal yields that have been reported in this chapter is given in two tables: Table 7.1 lists the statistical uncertainties on the MC samples and table 7.2 the remaining systematic uncertainties.

Table 7.1: Systematic uncertainties on the background and signal yields due to statistical uncertainties on the MC samples.

		$t\bar{t}$	$t\bar{t}V$	$t\bar{t}VV$	VVV	Signal
1μ	cut-and-count	±33%	±37%	±12%	±23%	±13%
	$0.4 < B < 0.6$	±14%	±20%	±8.7%	±13%	±10%
	$0.6 < B < 0.8$	±22%	±20%	±11%	±14%	±11%
	$0.8 < B < 1$	±41%	±53%	±17%	±19%	±18%
$1e$	cut-and-count	±40%	±33%	±20%	±23%	±17%
	$0.4 < B < 0.6$	±14%	±25%	±9.8%	±15%	±10%
	$0.6 < B < 0.8$	±23%	±39%	±12%	±17%	±13%
	$0.8 < B < 1$	±33%	±78%	±17%	±19%	±15%
2ℓss	cut-and-count	±45%	±11%	±11%	±7.8%	±12%
	$0.4 < B < 0.6$	±19%	±7.5%	±9.0%	±5.2%	±7.8%
	$0.6 < B < 0.8$	±29%	±11%	±11%	±7.6%	±12%
	$0.8 < B < 1$	±100%	±18%	±17%	±9.6%	±18%

Table 7.2: Other systematic uncertainties on the background and signal yields.

		$t\bar{t}$	$t\bar{t}V$	$t\bar{t}VV$	VVV	Signal
Cross Section	1μ, $1e$	$+4.8\%$ -5.5%	$+4.3\%$ -6.2%	$+4.3\%$ -6.2%	$+2.5\%$ -2.2%	-
	2ℓss	$+4.8\%$ -5.5%	$+4.3\%$ -6.2%	$+4.3\%$ -6.2%	$+2.5\%$ -2.2%	-
t-tagging	1μ, $1e$	$+4.3\%$ -4.8%	$+4.3\%$ -4.8%	$+4.3\%$ -4.8%	$+4.3\%$ -4.8%	$+4.3\%$ -4.8%
	2ℓss	-	-	-	-	-
W-tagging	1μ, $1e$	$+5.7\%$ -5.3%	$+5.7\%$ -5.3%	$+5.7\%$ -5.3%	$+5.7\%$ -5.3%	$+5.7\%$ -5.3%
	2ℓss	$+5.7\%$ -5.3%	$+5.7\%$ -5.3%	$+5.7\%$ -5.3%	$+5.7\%$ -5.3%	$+5.7\%$ -5.3%
Lepton ID	1μ, $1e$	±2%	±2%	±2%	±2%	±2%
	2ℓss	±4%	±4%	±4%	±4%	±4%
Luminosity	1μ, $1e$	±2.5%	±2.5%	±2.5%	±2.5%	±2.5%
	2ℓss	±2.5%	±2.5%	±2.5%	±2.5%	±2.5%

8 Results

The results of the analysis presented in this thesis are extracted by performing a binned maximum-likelihood fit to pseudo-datasets. The quadratic dependence of the $pp \rightarrow tjW^+W^-$ cross section on the Wilson coefficient c_{uH} has been described in chapter 5 (see equation 5.6). Dividing the cross section σ by the SM expectation σ_{SM} gives a scaling function

$$\mu_i(c_{\mathrm{uH}}) = 1 + A_i\, c_{\mathrm{uH}} + B_i\, c_{\mathrm{uH}}^2 \,, \tag{8.1}$$

which parametrizes deviations from the SM expectation in a bin i in terms of c_{uH}. After determining the expected signal yield in bin i, $s_i(c_{\mathrm{uH}})$, for three different values of the Wilson coefficient, $c_{\mathrm{uH}} = 0, \alpha, \beta$, using simulated $pp \rightarrow tjW^+W^-$ samples, the ratios

$$\mu_i(c_{\mathrm{uH}}) = \frac{s_i(c_{\mathrm{uH}})}{s_i^{\mathrm{SM}}} \,, \tag{8.2}$$

where $s_i^{\mathrm{SM}} \equiv s_i(c_{\mathrm{uH}} = 0)$, are used to determine the coefficients A_i and B_i:

$$
\begin{aligned}
A_i &= \frac{1}{\beta - \alpha} \left[\frac{\beta}{\alpha} \big(\mu_i(\alpha) - 1\big) - \frac{\alpha}{\beta} \big(\mu_i(\beta) - 1\big) \right] \\
B_i &= \frac{1}{\beta - \alpha} \left[\frac{1}{\beta} \big(\mu_i(\beta) - 1\big) - \frac{1}{\alpha} \big(\mu_i(\alpha) - 1\big) \right] .
\end{aligned}
\tag{8.3}
$$

The expected yield y_i in bin i is

$$y_i(c_{\mathrm{uH}}) = \mu_i(c_{\mathrm{uH}})\, s_i^{\mathrm{SM}} + b_i \,. \tag{8.4}$$

The signal yield scaling functions $\mu_i(c_{\mathrm{uH}})$ in the three event categories, obtained from the cut-and-count analysis of section 6.3.1 and the multivariate analysis of section 6.3.2, along with the expected background and SM signal yields, b_i and s_i^{SM}, scaled to an integrated luminosity of 3000 fb^{-1}, are listed in table 8.1.

The systematic uncertainties on the predicted yields y_i are handled by introducing a set of nuisance parameters $\boldsymbol{\theta} = (\theta_1, ..., \theta_M)$, so signal and background expectations become functions of the nuisance parameters, $s_i^{\mathrm{SM}}(\boldsymbol{\theta})$, $b_i(\boldsymbol{\theta})$. Given an observation $\boldsymbol{n} = (n_1, ..., n_N)$, the likelihood function [52]

$$L(\boldsymbol{n}\,|\,c_{\mathrm{uH}}, \boldsymbol{\theta}) = \left(\prod_i \frac{y_i^{n_i}\, e^{-y_i}}{n_i!} \right) \cdot p(\tilde{\boldsymbol{\theta}}\,|\,\boldsymbol{\theta}) \tag{8.5}$$

is a product of Poisson probabilities in the bins $i = 1, ..., N$, times the probability density functions (pdfs), $p(\tilde{\boldsymbol{\theta}}\,|\,\boldsymbol{\theta})$, of the uncertainties on the nominal values of the nuisance parameters, $\tilde{\boldsymbol{\theta}}$. The pdfs are Gaussian distributions in case of the MC statistical uncertainties, and log-normal otherwise.

Table 8.1: Expected SM background and signal yields and BSM signal yield scaling functions, $\mu_i(c_{\mathrm{uH}}) = 1 + A_i\, c_{\mathrm{uH}} + B_i\, c_{\mathrm{uH}}^2$, for cut-and-count and multivariate analysis.

	Bin	Background	SM signal	BSM signal scaling function
	cut-and-count	35.8 ± 8.3	4.6 ± 0.6	$1 + 0.068\, c_{\mathrm{uH}} + 0.0076\, c_{\mathrm{uH}}^2$
1μ	$0.4 < B < 0.6$	201 ± 22	10.2 ± 1.1	$1 + 0.034\, c_{\mathrm{uH}} + 0.0021\, c_{\mathrm{uH}}^2$
	$0.6 < B < 0.8$	107 ± 15	9.0 ± 1.0	$1 + 0.049\, c_{\mathrm{uH}} + 0.0032\, c_{\mathrm{uH}}^2$
	$0.8 < B < 1$	26.5 ± 7.7	3.3 ± 0.6	$1 + 0.16\, c_{\mathrm{uH}} + 0.014\, c_{\mathrm{uH}}^2$
	cut-and-count	32.5 ± 8.1	3.0 ± 0.5	$1 + 0.17\, c_{\mathrm{uH}} + 0.0091\, c_{\mathrm{uH}}^2$
$1e$	$0.4 < B < 0.6$	200 ± 23	10.4 ± 1.1	$1 + 0.022\, c_{\mathrm{uH}} + 0.0016\, c_{\mathrm{uH}}^2$
	$0.6 < B < 0.8$	83.9 ± 15.5	7.1 ± 0.9	$1 + 0.060\, c_{\mathrm{uH}} + 0.0030\, c_{\mathrm{uH}}^2$
	$0.8 < B < 1$	37.7 ± 10.9	5.1 ± 0.8	$1 + 0.12\, c_{\mathrm{uH}} + 0.0083\, c_{\mathrm{uH}}^2$
	cut-and-count	41.0 ± 5.4	5.8 ± 0.7	$1 + 0.068\, c_{\mathrm{uH}} + 0.0049\, c_{\mathrm{uH}}^2$
$2\ell\mathrm{ss}$	$0.4 < B < 0.6$	154 ± 15	18.8 ± 1.5	$1 + 0.0045\, c_{\mathrm{uH}} + 0.00099\, c_{\mathrm{uH}}^2$
	$0.6 < B < 0.8$	71.1 ± 9.7	7.6 ± 0.9	$1 + 0.048\, c_{\mathrm{uH}} + 0.0023\, c_{\mathrm{uH}}^2$
	$0.8 < B < 1$	22.9 ± 5.6	3.5 ± 0.6	$1 + 0.092\, c_{\mathrm{uH}} + 0.011\, c_{\mathrm{uH}}^2$

The test statistic is the profile likelihood ratio [52]

$$q_{c_{\mathrm{uH}}} = -2\,\ln\left(\frac{L(\boldsymbol{n}\,|\,c_{\mathrm{uH}}, \hat{\boldsymbol{\theta}}_{c_{\mathrm{uH}}})}{L(\boldsymbol{n}\,|\,\hat{c}_{\mathrm{uH}}, \hat{\boldsymbol{\theta}})} \right), \tag{8.6}$$

where $\hat{c}_{\mathrm{uH}}$ and $\hat{\boldsymbol{\theta}}$ are the values of the parameters obtained by maximizing L, and $\hat{\boldsymbol{\theta}}_{c_{\mathrm{uH}}}$ refers to the values of the nuisance parameters that maximize L for a given c_{uH}. According to Wilk's theorem [53], for large enough sample size, the profile likelihood ratio follows a chi-squared distribution: $q_{c_{\mathrm{uH}}} \sim \chi^2$. The 2σ (95.4%) upper limit on the Wilson coefficient is then simply the value $\tilde{c}_{\mathrm{uH}}$ for which $\sqrt{q_{\tilde{c}_{\mathrm{uH}}}} = 2$.

The expected 2σ upper limit is used to quantify the sensitivity of the analysis. It is obtained by evaluating the test statistic $q_{c_{\mathrm{uH}}}$ on a toy dataset generated with the Wilson coefficient set to the SM expectation, $c_{\mathrm{uH}} = 0$. The expected 2σ upper limit for the cut-and-count analysis of section 6.3.1, in 3000 fb^{-1} of data, is

$$c_{\mathrm{uH}} < 15.4 = \sqrt{10.6^2(\mathrm{stat}) + 7.1^2(\mathrm{syst}) + 8.6^2(\mathrm{MC})}\,, \tag{8.7}$$

where stat, MC, syst refer to the contributions from statistical fluctuations of the data, systematic uncertainties due to statistical uncertainties on the MC samples, and the remaining systematic uncertainties. Expressed in terms of δy_t, where $y_t = y_t^{\mathrm{SM}}(1 + \delta y_t)$, this is [44]

$$\delta y_t = \frac{v^2}{\Lambda^2}\, c_{\mathrm{uH}} \approx 0.0605\, c_{\mathrm{uH}} < 0.93 = \sqrt{0.64^2(\mathrm{stat}) + 0.43^2(\mathrm{syst}) + 0.52^2(\mathrm{MC})}\,. \tag{8.8}$$

For the MVA analysis of section 6.3.2, it is

$$
\begin{aligned}
c_{\mathrm{uH}} &< 12.4 = \sqrt{7.7^2(\mathrm{stat}) + 4.8^2(\mathrm{syst}) + 8.4^2(\mathrm{MC})}\,, \\
\delta y_t &< 0.75 = \sqrt{0.47^2(\mathrm{stat}) + 0.29^2(\mathrm{syst}) + 0.51^2(\mathrm{MC})}\,.
\end{aligned}
\tag{8.9}
$$

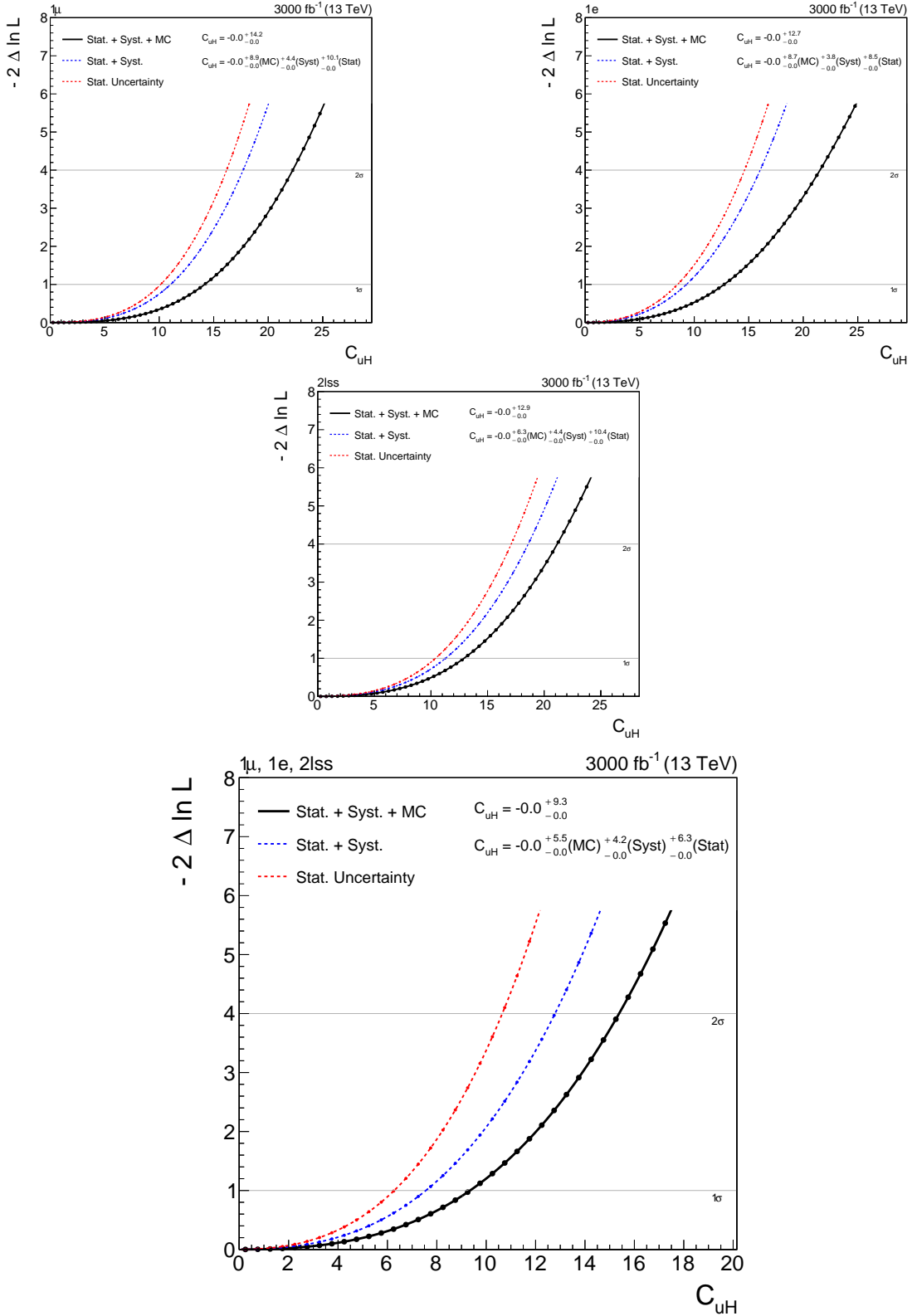The profile likelihood scans are shown in figures 8.1 and 8.2.

Figure 8.1: Profile likelihood scans on c_{uH} from cut-and-count analysis in the 1μ (top left), $1e$ (top right), and 2ℓss (center) event categories, and the three categories combined (bottom).
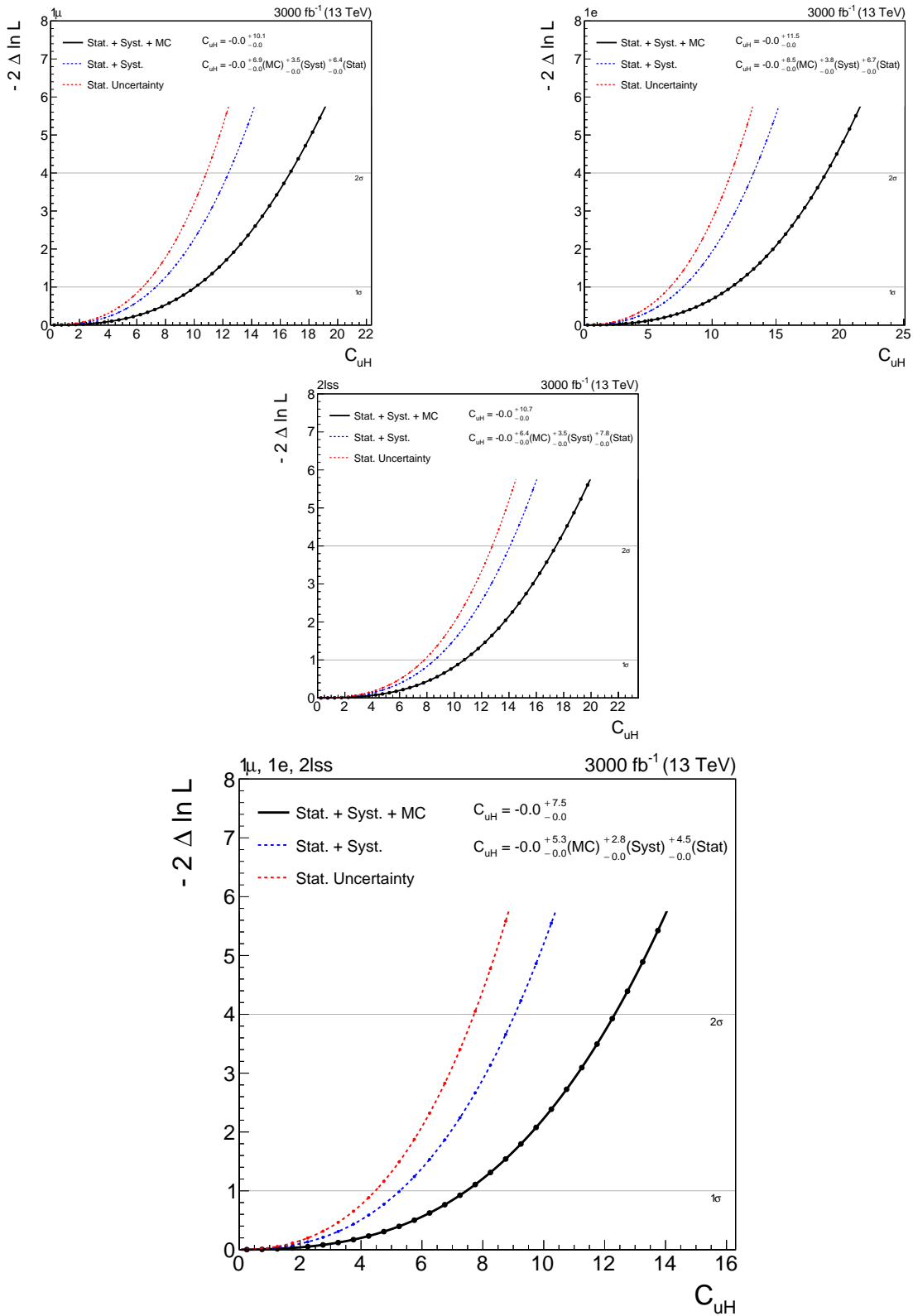
Figure 8.2: Profile likelihood scans on c_{uH} from multivariate analysis in the 1μ (top left), $1e$ (top right), and 2ℓss (center) event categories, and the three categories combined (bottom).

57

9 Summary and Outlook

The expected 1σ and 2σ upper limits on the Wilson coefficient c_{uH} for the multivariate analysis presented in this thesis, when using the full data to be collected by the end of the HL-LHC programme (3000 fb^{-1}), $c_{\text{uH}} < 7.5$ and $c_{\text{uH}} < 12.4$, correspond to an expected ratio of the top quark Yukawa coupling to its Standard Model value of

$$\frac{y_t}{y_t^{\text{SM}}} = 1 + \delta y_t = 1 \pm 0.45\,(\text{tot}) = 1 \pm 0.27\,(\text{stat}) \pm 0.17\,(\text{syst}) \pm 0.32\,(\text{MC})\,, \qquad (9.1)$$

with a 2σ upper limit of $y_t/y_t^{\text{SM}} < 1.75$. The main source of uncertainty is the background modelling, which uses Monte Carlo samples with limited statistics in the relevant phase space. For further studies, the effect of these uncertainties can be reduced by a data-driven background estimation, or by simply generating much larger MC samples. Assuming the MC statistical uncertainty to be negligible, the expected ratio becomes

$$\frac{y_t}{y_t^{\text{SM}}} = 1 \pm 0.32\,(\text{tot}) \qquad (9.2)$$

and the 2σ upper limit reduces to $y_t/y_t^{\text{SM}} < 1.55$.

An indirect measurement in $pp \to t\bar{t}$ events, performed by the CMS collaboration on the full Run 2 dataset, has obtained a result of $y_t/y_t^{\text{SM}} = 1.16\,^{+0.07}_{-0.08}\,(\text{stat})\,^{+0.23}_{-0.34}\,(\text{syst})$ and an approximate upper limit at the 95% confidence level of $y_t/y_t^{\text{SM}} < 1.54$. The SM expected 95% upper limit of that analysis is $y_t/y_t^{\text{SM}} < 1.47$ [54]. The measurement in the $pp \to tjW^+W^-$ channel presented in this thesis therefore reaches a sensitivity in HL-LHC data comparable to the sensitivity of current CMS analyses on Run 2 data only.

The sensitivity of a direct measurement of the coupling modifier κ_t (corresponding to y_t/y_t^{SM}), in $pp \to t\bar{t}h$ with the CMS detector, is projected to 3000 fb^{-1} of data by the LHC Higgs Combination Group in reference [55]. Assuming the MC statistical uncertainties to be negligible, and the remaining systematic uncertainties to be the same as in Run 2, they expect a $\pm 1\sigma$ uncertainty on κ_t of 5.5%. A direct measurement of the top quark Yukawa coupling in the $pp \to tth$ channel is therefore expected to be almost six times more sensitive than the indirect measurement in the $pp \to tjW^+W^-$ channel.

Several aspects of the analysis presented in this thesis leave room for improvement. The small number of simulated background events in the selected phase space has been discussed previously, however, even when the Monte Carlo statistical uncertainties are not taken into account explicitly, they limit the sensitivity of the measurement significantly. In the cut-and-count analysis, constraints on the event kinematics have been chosen rather conservatively, always keeping in mind not only the expected signal significance, but also the number of simulated events passing the constraints. Once a few cuts are applied, the limited size of the simulated samples leads to sizable fluctuations from bin

to bin, making it difficult to determine the ideal thresholds for consecutive constraints. In the multivariate analysis, the training of the BDT classifier suffers from the limited statistics as well. To make sure the test sets are not too small, the training sets contain only 20% of the simulated background events that pass the preselection in the three event categories. It is likely that the background rejecting power of the MVA could be improved if trained on more simulated data. Furthermore, the binning on the BDT classifier has been chosen in such a way that the number of simulated events from each background sample is not too small in any bin, in order to keep the MC uncertainties manageable. It is therefore reasonable to assume that an improved background estimation would allow for a significant improvement of the event selection, both in cut-and-count and multivariate analysis, leading to reduced uncertainties and better sensitivity.

This analysis takes into account only the $pp \to tjW^+W^-$ channel, where one W boson decays hadronically, the other leptonically. When taking into account the other signal channels, $pp \to tjW^{\pm}W^{\pm}$, $tjZW^{\pm}$, and $tjZZ$, the cross sections of which are listed in table 9.1, the signal yields increase. The SM $pp \to tjW^{\pm}W^{\pm}$ cross section is very similar to that of $pp \to tjW^+W^-$, and the event kinematics of the two channels are alike as well. In the single lepton event categories, $tjW^{\pm}W^{\pm}$ final states are reconstructed with the same efficiency as tjW^+W^-. In the dilepton category, due to the same-sign requirement on the leptons, tjW^+W^+ and $\bar{t}jW^-W^-$ events with semileptonic W boson decays do not contribute. However, it might be possible to get a signal from events where both W bosons decay leptonically and the top quark hadronically. The Z boson channels, $pp \to tjZW^{\pm}$ and $pp \to tjZZ$, need further investigation. Despite its SM cross section being considerably larger than the $pp \to tjWW$ cross sections, $pp \to tjZW^{\pm}$ seems to be the least promising channel, due to its weak c_{uH} dependence. The $pp \to tjZZ$ cross section is two orders of magnitude smaller, but it is much more sensitive to modifications of the top quark Yukawa coupling than the other channels. Whether taking this channel into consideration can improve the sensitivity of the analysis depends on the hadronic Z boson tagging performance and on how well leptonic Z boson decays can be incorporated into the event selection.

Taking into account the other decay modes of the W boson pair will further increase the signal yields. The semileptonic decay mode, the one studied in this analysis, has a branching fraction of around 44%, the fully hadronic mode 45%, and the fully leptonic mode 11%. The fully hadronic decay of the W boson pair, in combination with a hadronically decaying top quark, seems to be the most challenging, as there is no lepton to trigger on and a total of three AK8 jets that have to be t- or W-tagged, leading to a reduced reconstruction efficiency. In combination with a leptonic top quark decay, the signal reconstruction looks easier than in the semileptonic diboson decay channel, however, with no hadronic top quark present in the event, reducing the backgrounds might be more difficult. Fully leptonic decays of the W^+W^- boson pair do not pass the current event selection, due to the requirement of same electric charge for the lepton pair, but this is partially compensated by the contribution from the fully leptonic $pp \to tjW^{\pm}W^{\pm}$ decay modes. Furthermore, when taking into account all signal channels discussed in the last two paragraphs, the dilepton event category, 2ℓss, could be split into separate categories based on lepton flavour, $\mu^{\pm}\mu^{\pm}$, $e^{\pm}e^{\pm}$, $\mu^{\pm}e^{\pm}$, and complemented by an opposite-flavour/opposite-charge category, $\mu^{\pm}e^{\mp}$. The latter would allow to select some of the signal from the fully leptonic tjW^+W^- and the semileptonic $tjW^{\pm}W^{\pm}$ de-

cay modes, while still rejecting backgrounds from leptonic Z boson decays, where both leptons have the same flavour.

Given these considerations, the potential of a top quark Yukawa coupling measurement in the $pp \to tjVV$ channel at the HL-LHC should not be written off. While the sensitivity of the analysis, as it has been presented here, is not yet competitive with other measurements, there are numerous opportunities for refinement that warrant further studies.

Table 9.1: Cross section of each signal channel for the three sets of cuts listed in equation (5.8).

signal channel	cut	σ (pb)
	cut 1	$2.48 \times 10^{-1} \left(1 - 0.000101\, c_{\mathrm{uH}} + 0.0000184\, c_{\mathrm{uH}}^2\right)$
tjW^+W^-	cut 2	$2.79 \times 10^{-2} \left(1 + 0.000306\, c_{\mathrm{uH}} + 0.0000407\, c_{\mathrm{uH}}^2\right)$
	cut 3	$8.00 \times 10^{-4} \left(1 + 0.00438\, c_{\mathrm{uH}} + 0.00123\, c_{\mathrm{uH}}^2\right)$
	cut 1	$2.50 \times 10^{-1} \left(1 - 0.0000434\, c_{\mathrm{uH}} + 0.00000622\, c_{\mathrm{uH}}^2\right)$
$tjW^{\pm}W^{\pm}$	cut 2	$2.78 \times 10^{-2} \left(1 + 0.0000430\, c_{\mathrm{uH}} + 0.0000170\, c_{\mathrm{uH}}^2\right)$
	cut 3	$8.60 \times 10^{-4} \left(1 + 0.0000698\, c_{\mathrm{uH}} + 0.000494\, c_{\mathrm{uH}}^2\right)$
	cut 1	$7.50 \times 10^{-1} \left(1 + 0.0000328\, c_{\mathrm{uH}} + 0.00000168\, c_{\mathrm{uH}}^2\right)$
$tjZW^{\pm}$	cut 2	$7.49 \times 10^{-2} \left(1 - 0.000272\, c_{\mathrm{uH}} + 0.0000122\, c_{\mathrm{uH}}^2\right)$
	cut 3	$4.05 \times 10^{-3} \left(1 + 0.00105\, c_{\mathrm{uH}} + 0.0000110\, c_{\mathrm{uH}}^2\right)$
	cut 1	$2.59 \times 10^{-3} \left(1 - 0.00432\, c_{\mathrm{uH}} + 0.000309\, c_{\mathrm{uH}}^2\right)$
$tjZZ$	cut 2	$2.70 \times 10^{-4} \left(1 - 0.00289\, c_{\mathrm{uH}} + 0.000812\, c_{\mathrm{uH}}^2\right)$
	cut 3	$8.60 \times 10^{-5} \left(1 - 0.00381\, c_{\mathrm{uH}} + 0.00205\, c_{\mathrm{uH}}^2\right)$

Bibliography

[1] B. Henning et al. *Measuring Higgs Couplings without Higgs Bosons*. In: *Phys. Rev. Lett.* 123, 181801 (2019). DOI: 10.1103/PhysRevLett.123.181801. arXiv: 1812.09299 [hep-ph].

[2] F. Halzen and A. Martin. *Quarks and Leptons*. John Wiley and Sons, 1984. ISBN: 978-0-471-88741-6.

[3] M. Schwartz. *Quantum Field Theory and the Standard Model*. Cambridge University Press, 2014. DOI: 10.1017/9781139540940.

[4] G. Isidori. *Flavour physics and CP violation*. 2012. arXiv: 1302.0661 [hep-ph].

[5] P.A. Zyla et al. (Particle Data Group). *Review of Particle Physics*. In: *Prog. Theor. Exp. Phys.* 083C01 (2020). DOI: 10.1093/ptep/ptaa104.

[6] UA1 Collaboration. *Experimental observation of isolated large transverse energy electrons with associated missing energy at $\sqrt{s} = 540$ GeV*. In: *Phys. Lett. B* 122 (1983), pp. 103–116. DOI: 10.1016/0370-2693(83)91177-2.

[7] UA1 Collaboration. *Experimental observation of lepton pairs of invariant mass around 95 GeV/c^2 at the CERN SPS collider*. In: *Phys. Lett. B* 126 (1983), pp. 398–410. DOI: 10.1016/0370-2693(83)90188-0.

[8] CMS Collaboration. *Observation of a New Boson at a Mass of 125 GeV with the CMS Experiment at the LHC*. In: *Phys. Lett. B* 716 (2012), pp. 30–61. DOI: 10.1016/j.physletb.2012.08.021. arXiv: 1207.7235 [hep-ex].

[9] ATLAS Collaboration. *Observation of a new particle in the search for the Standard Model Higgs boson with the ATLAS detector at the LHC*. In: *Phys. Lett. B* 716 (2012), pp. 1–29. DOI: 10.1016/j.physletb.2012.08.020. arXiv: 1207.7214 [hep-ex].

[10] ATLAS and CMS Collaborations. *Measurements of the Higgs boson production and decay rates and constraints on its couplings from a combined ATLAS and CMS analysis of the LHC pp collision data at $\sqrt{s} = 7$ and 8 TeV*. In: *Journal of High Energy Physics* 08 (2016). DOI: 10.1007/JHEP08(2016)045. arXiv: 1606.02266 [hep-ex].

[11] ATLAS Collaboration. *Cross-section measurements of the Higgs boson decaying into a pair of τ-leptons in proton-proton collisions at $\sqrt{s} = 13$ TeV with the ATLAS detector*. In: *Phys. Rev. D* 99, 072001 (2019). DOI: 10.1103/PhysRevD.99.072001. arXiv: 1811.08856 [hep-ex].

[12] CMS Collaboration. *Observation of the Higgs boson decay to a pair of τ leptons with the CMS detector*. In: *Phys. Lett. B* 779 (2018), pp. 283–316. DOI: 10.1016/j.physletb.2018.02.004. arXiv: 1708.00373 [hep-ex].

[13] ATLAS Collaboration. *Observation of $H \rightarrow b\bar{b}$ decays and VH production with the ATLAS detector*. In: *Phys. Lett. B* 786 (2018), pp. 59–86. DOI: 10.1016/j. physletb.2018.09.013. arXiv: 1808.08238 [hep-ex].

[14] CMS Collaboration. *Observation of Higgs boson decay to bottom quarks*. In: *Phys. Rev. Lett.* 121, 121801 (2018). DOI: 10.1103/PhysRevLett.121.121801. arXiv: 1808.08242 [hep-ex].

[15] ATLAS Collaboration. *Observation of Higgs boson production in association with a top quark pair at the LHC with the ATLAS detector*. In: *Phys. Lett. B* 784 (2018), pp. 173–191. DOI: 10.1016/j.physletb.2018.07.035. arXiv: 1806.00425 [hep-ex].

[16] CMS Collaboration. *Observation of* $t\bar{t}H$ *production*. In: *Phys. Rev. Lett.* 120, 231801 (2018). DOI: 10.1103/PhysRevLett.120.231801. arXiv: 1804.02610 [hep-ex].

[17] CMS Collaboration. *Evidence for Higgs boson decay to a pair of muons*. In: *Journal of High Energy Physics* 01, 148 (2021). DOI: 10.1007/JHEP01(2021)148. arXiv: 2009.04363 [hep-ex].

[18] ATLAS Collaboration. *A search for the dimuon decay of the Standard Model Higgs boson with the ATLAS detector*. In: *Phys. Lett. B* 812, 135980 (2021). DOI: 10. 1016/j.physletb.2020.135980. arXiv: 2007.07830 [hep-ex].

[19] ATLAS Collaboration. *Direct constraint on the Higgs-charm coupling from a search for Higgs boson decays into charm quarks with the ATLAS detector*. 2022. arXiv: 2201.11428 [hep-ex].

[20] CMS Collaboration. *A measurement of the Higgs boson mass in the diphoton decay channel*. In: *Phys. Lett. B* 805, 135425 (2020). DOI: 10.1016/j.physletb.2020. 135425. arXiv: 2002.06398 [hep-ex].

[21] Y. Fukuda et al. *Evidence for oscillation of atmospheric neutrinos*. In: *Phys. Rev. Lett.* 81 (1998), pp. 1562–1567. DOI: 10.1103/PhysRevLett.81.1562. arXiv: hep-ex/9807003.

[22] C. Pérez de los Heros. *Status of direct and indirect dark matter searches*. 2020. arXiv: 2001.06193 [astro-ph.HE].

[23] P. de Simone. *Experimental Review on Lepton Universality and Lepton Flavour Violation tests in B decays*. In: *EPJ Web Conf.* 234, 01004 (2020). DOI: 10.1051/ epjconf/202023401004.

[24] B. Grzadkowski et al. *Dimension-Six Terms in the Standard Model Lagrangian*. In: *Journal of High Energy Physics* 10, 058 (2010). DOI: 10.1007/JHEP10(2010)085. arXiv: 1008.4884 [hep-ph].

[25] R. Alonso et al. *Renormalization Group Evolution of the Standard Model Dimension Six Operators III: Gauge Coupling Dependence and Phenomenology*. In: *Journal of High Energy Physics* 04, 159 (2013). DOI: 10.1007/JHEP04(2014)159. arXiv: 1312.2014 [hep-ph].

[26] ALICE Collaboration. *The ALICE experiment at the CERN LHC*. In: *Journal of Instrumentation* 3, S08002 (2008). DOI: 10.1088/1748-0221/3/08/S08002.

[27] ATLAS Collaboration. *The ATLAS Experiment at the CERN Large Hadron Collider*. In: *Journal of Instrumentation* 3, S08003 (2008). DOI: 10.1088/1748-0221/3/08/S08003.

[28] CMS Collaboration. *The CMS experiment at the CERN LHC*. In: *Journal of Instrumentation* 3, S08004 (2008). DOI: 10.1088/1748-0221/3/08/s08004.

[29] LHCb Collaboration. *The LHCb Detector at the LHC*. In: *Journal of Instrumentation* 3, S08005 (2008). DOI: 10.1088/1748-0221/3/08/S08005.

[30] *High-Luminosity Large Hadron Collider (HL-LHC): Technical Design Report V. 0.1*. In: *CERN Yellow Reports: Monographs* (2017). Ed. by G. Apollinari et al. DOI: 10.23731/CYRM-2017-004.

[31] CMS Tracker Group. *The CMS Phase-1 Pixel Detector Upgrade*. In: *Journal of Instrumentation* 16, P02027 (2021). DOI: 10.1088/1748-0221/16/02/P02027. arXiv: 2012.14304 [physics.ins-det].

[32] CMS Collaboration. *Description and performance of track and primary-vertex reconstruction with the CMS tracker*. In: *Journal of Instrumentation* 9, P10009 (2014). DOI: 10.1088/1748-0221/9/10/p10009. arXiv: 1405.6569 [physics.ins-det].

[33] CMS Collaboration. *The CMS trigger system*. In: *Journal of Instrumentation* 12, P01020 (2017). DOI: 10.1088/1748-0221/12/01/p01020. arXiv: 1609.02366 [physics.ins-det].

[34] S. Paoletti. *The CMS Tracker Upgrade for the High Luminosity LHC*. In: *PoS* EPS-HEP2019 (2020). DOI: 10.22323/1.364.0138.

[35] CMS Collaboration. *Particle-flow reconstruction and global event description with the CMS detector*. In: *Journal of Instrumentation* 12, P10003 (2017). DOI: 10.1088/1748-0221/12/10/p10003. arXiv: 1706.04965 [physics.ins-det].

[36] CMS Collaboration. *Performance of the CMS muon detector and muon reconstruction with proton-proton collisions at $\sqrt{s} = 13$ TeV*. In: *Journal of Instrumentation* 13, P06015 (2018). DOI: 10.1088/1748-0221/13/06/p06015. arXiv: 1804.04528 [physics.ins-det].

[37] CMS Collaboration. *Electron and photon reconstruction and identification with the CMS experiment at the CERN LHC*. In: *Journal of Instrumentation* 16, P05014 (2021). DOI: 10.1088/1748-0221/16/05/P05014. arXiv: 2012.06888 [hep-ex].

[38] M. Cacciari, G.P. Salam, and G. Soyez. *The anti-k_T jet clustering algorithm*. In: *Journal of High Energy Physics* 04, 063 (2008). DOI: 10.1088/1126-6708/2008/04/063. arXiv: 0802.1189 [hep-ph].

[39] CMS Collaboration. *Identification of heavy, energetic, hadronically decaying particles using machine-learning techniques*. In: *Journal of Instrumentation* 15, P06005 (2020). DOI: 10.1088/1748-0221/15/06/P06005. arXiv: 2004.08262 [hep-ex].

[40] CMS Collaboration. *Identification of heavy-flavour jets with the CMS detector in pp collisions at 13 TeV*. In: *Journal of Instrumentation* 13, P05011 (2017). DOI: 10.1088/1748-0221/13/05/P05011. arXiv: 1712.07158 [physics.ins-det].

[41] CMS Collaboration. *Reconstruction and identification of τ lepton decays to hadrons and ν_τ at CMS*. In: *Journal of Instrumentation* 11, P01019 (2016). DOI: 10.1088/1748-0221/11/01/p01019. arXiv: 1510.07488 [physics.ins-det].

[42] J. Alwall et al. *MadGraph 5: going beyond.* In: *Journal of High Energy Physics* 6, 128 (2011). DOI: 10.1007/JHEP06(2011)128. arXiv: 1106.0522 [hep-ph].

[43] I. Brivio, Y. Jiang, and M. Trott. *The SMEFTsim package, theory and tools.* In: *Journal of High Energy Physics* 12, 70 (2017). DOI: 10.1007/JHEP12(2017)070. arXiv: 1709.06492 [hep-ph].

[44] I. Brivio. *SMEFTsim 3.0 — a practical guide.* In: *Journal of High Energy Physics* 4, 73 (2021). DOI: 10.1007/JHEP04(2021)073. arXiv: 2012.11343 [hep-ph].

[45] T. Sjöstrand et al. *An introduction to PYTHIA 8.2.* In: *Comp. Phys. Commun.* 191 (2015), pp. 159–177. DOI: 10.1016/j.cpc.2015.01.024. arXiv: 1410.3012 [hep-ph].

[46] P. Artoisenet et al. *Automatic spin-entangled decays of heavy resonances in Monte Carlo simulations.* In: *Journal of High Energy Physics* 3, 15 (2013). DOI: 10.1007/JHEP03(2013)015. arXiv: 1212.3460 [hep-ph].

[47] G. Cowan. *Discovery sensitivity for a counting experiment with background uncertainty.* 2012. URL: http://www.pp.rhul.ac.uk/~cowan/stat/medsig/medsigNote.pdf.

[48] T. Chen and C. Guestrin. "XGBoost: A Scalable Tree Boosting System". In: *KDD '16: Proceedings of the 22nd ACM SIGKDD International Conference on Knowledge Discovery and Data Mining.* 2016, pp. 785–794. DOI: 10.1145/2939672.2939785. arXiv: 1603.02754 [cs.LG].

[49] M. Czakon and A. Mitov. *Top++: A Program for the Calculation of the Top-Pair Cross-Section at Hadron Colliders.* In: *Comput. Phys. Commun.* 185 (2014), pp. 2930–2938. DOI: 10.1016/j.cpc.2014.06.021. arXiv: 1112.5675 [hep-ph].

[50] N. Kidonakis. *Top Quark Production.* 2013. DOI: 10.48550/arXiv.1311.0283. arXiv: 1311.0283 [hep-ph].

[51] T. Gehrmann et al. W^+W^- *Production at Hadron Colliders in Next to Next to Leading Order QCD.* In: *Phys. Rev. Lett.* 113, 212001 (2014). DOI: 10.1103/PhysRevLett.113.212001. arXiv: 1408.5243 [hep-ph].

[52] ATLAS and CMS Collaborations, and LHC Higgs Combination Group. *Procedure for the LHC Higgs boson search combination in Summer 2011.* URL: https://cds.cern.ch/record/1379837.

[53] S.S. Wilks. *The Large-Sample Distribution of the Likelihood Ratio for Testing Composite Hypotheses.* In: *Annals Math. Statist.* 9 (1938), pp. 60–62. DOI: 10.1214/aoms/1177732360.

[54] CMS Collaboration. *Measurement of the top quark Yukawa coupling from $t\bar{t}$ kinematic distributions in the dilepton final state in proton-proton collisions at $\sqrt{s} = 13$ TeV.* In: *Phys. Rev. D* 102, 092013 (2020). DOI: 10.1103/PhysRevD.102.092013. arXiv: 2009.07123 [hep-ex].

[55] LHC Higgs Combination Group. *Higgs Physics at the HL-LHC and HE-LHC.* 2019. DOI: 10.48550/arXiv.1902.00134. arXiv: 1902.00134 [hep-ph].